UC Berkeley
UC Berkeley Electronic Theses and Dissertations

Title
New Advances in Spectroscopy: Applications to Aqueous Interfaces and Liquid Carbon

Permalink
https://escholarship.org/uc/item/3pq2f84z

Author
Mizuno, Hikaru

Publication Date
2021

Peer reviewed|Thesis/dissertation

eScholarship.org Powered by the California Digital Library
University of California

New Advances in Spectroscopy: Applications to Aqueous Interfaces and Liquid Carbon

By

Hikaru Mizuno

A dissertation submitted in partial satisfaction of the

requirements for the degree of

Doctor of Philosophy

in

Chemistry

in the

Graduate Division

of the

University of California, Berkeley

Committee in charge:

Professor Richard J. Saykally, Chair
Professor Daniel M. Neumark
Professor Kranthi K. Mandadapu

Spring 2021

New Advances in Spectroscopy: Applications to Aqueous Interfaces and Liquid Carbon

© Copyright 2021
by
Hikaru Mizuno

Abstract

New Advances in Spectroscopy: Applications to Aqueous Interfaces and Liquid Carbon

by

Hikaru Mizuno

Doctor of Philosophy in Chemistry

University of California, Berkeley

Professor Richard J. Saykally, Chair

This dissertation comprises two major projects. The first is the study of ions and molecules at the air/water interface using second-order nonlinear spectroscopy to measure interfacial electronic $|\chi^{(2)}|^2$-spectra. The second is the investigation of the liquid state of carbon using time-resolved soft X-ray free electron laser spectroscopy.

The nature of ions and molecules at and near aqueous interfaces is central in many chemical systems including atmospheric chemistry, electrochemistry, and biochemistry, but remains incompletely understood. Contrary to widely held earlier views, recent studies have unambiguously shown that some ions adsorb strongly to the air/water interface, with compelling evidence for enhanced surface concentrations of larger, more polarizable, weakly solvated anions. While the mechanism of selective ion adsorption has been shown to correlate strongly with ionic radii and hydration properties, considerable debate remains.

In this dissertation, I describe the development and application of femtosecond broadband deep ultraviolet electronic sum frequency generation (DUV-ESFG) spectroscopy which allows quantitative analysis of peak positions, linewidths, and relative intensities that can be directly compared with theoretical calculations to yield new insights into the nature of ions and molecules at aqueous interfaces. Under the electric dipole approximation, the second-order nonlinear susceptibility vanishes in centrosymmetric media, and SFG spectroscopy is a surface-sensitive probe with a probe depth of ca. 1 nm, corresponding to a few outermost monolayers.

In Chapter 2, I present the interfacial charge-transfer-to-solvent spectrum of thiocyanate (SCN^-), a prototypical chaotropic anion, and discuss selection rules and salient differences between interfacial and bulk solvation that contribute to the observed spectral differences.

In Chapter 3, we investigate the lowest energy charge-transfer-to-solvent bands of aqueous iodide using broadband DUV-ESFG and two-photon absorption spectroscopy and assign the observed transitions using atomic selection rules within a Rydberg transition model based on the *jj*-coupling limit. We find that DUV-ESFG signal at the air/water interface arises from symmetry breaking and solute-solvent vibronic coupling effects that relax the selection rules.

In Chapter 4, we revisit the $\pi \rightarrow \pi^*$ transition of the nitrite ion at the air/water interface and, together with MD simulations and electronic structure calculations, find no evidence of a previously reported contact ion pair induced redshift and strongly favorable bimolecular

adsorption mechanism. However, the presence of a distribution of local solvation environments at the interface, including solvent separated ion pairs, solvent shared ion pairs, contact ion pairs, and small ion clusters is not ruled out.

In Chapter 5, I present the $|\chi^{(2)}|^2$-spectra of phenol at the air/water interface in the deep UV (5.4-6.3 eV) and find an apparent redshift of the electronic transitions relative to the bulk aqueous spectrum. MD simulations and electronic structure calculations suggest stabilization of the excited states due to the highly specific hydration structure effected at the interface. Additional work is ongoing to elucidate the role of selection rules and solvent environment on the observed spectral differences.

In Chapter 6, I discuss my efforts to attempt heterodyne-detected DUV-ESFG spectroscopy and future directions, including incorporating a flat-jet that would enable measurements at low concentrations and liquid/liquid interfaces.

The liquid state of carbon is of fundamental chemical significance and has potential practical applications, but it remains very poorly characterized. For example, studies suggest that carbon nanotubes and Q-carbon are formed through liquid intermediates. Moreover, novel carbon materials and routes for synthesizing them are of great interest, as some proposed carbon allotropes may have exciting new properties for technological applications, and better understanding of the liquid properties may suggest new routes for synthesizing them. In this dissertation, I present our recent efforts to characterize liquid carbon using pump-probe soft X-ray free electron laser spectroscopy at the carbon *K*-edge.

In Chapter 7, I detail time-resolved resonant inelastic X-ray scattering (tr-RIXS) and X-ray emission spectra (tr-XES) of non-thermally melted carbon films measured at the Pohang Accelerator Laboratory X-ray Free Electron Laser in South Korea. An initial decrease in tr-RIXS signal intensity at short delay times was observed, corresponding to a decrease in the absorption cross-section of sp^2-hybridized carbon atoms as structural reorganization occurs to form liquid carbon. Additional theoretical work is ongoing to further elucidate the dynamics of the melting and ablation processes.

In Chapter 8, I present and discuss our recent attempts to demonstrate optical & soft X-ray sum frequency generation spectroscopy at the carbon *K*-edge, building upon soft X-ray second harmonic generation spectroscopy demonstrated by our group at FERMI in Italy.

To my friends and family.

Table of Contents

List of Figures

List of Tables

Acknowledgements

I would like to thank my advisor Rich for his amazing mentorship and support—his passion and enthusiasm for science are inspiring. To current and former members of the Saykally Group, thank you for making the Ph.D. journey fun and enjoyable. I am grateful for my collaborators at UC Berkeley, LBNL, USC, FERMI, PAL-XFEL, LLNL, and Stockholm University; without them, none of this work would have been possible.

Thank you to my family and friends for their love, encouragement, and support.

This work was supported by the Director, Office of Basic Energy Sciences, Office of Science, U.S. Department of Energy (DOE) under Contract No. DE-AC02-05CH11231 through the Chemical Sciences Division of the Lawrence Berkeley National Laboratory (LBNL), and U.S. Army Research Laboratory and the U.S. Army Research Office under grant No. W911NF-13-1-0483 and No. W911NF-17-1-0163.

Chapter 1 Femtosecond Broadband Deep Ultraviolet Electronic Sum Frequency Generation Spectroscopy

The behavior of ions at and near aqueous interfaces is of central importance in many chemical systems, including atmospheric chemistry,[1,2] electrochemistry,[3–5] and biochemistry,[6] but remains incompletely understood. Contrary to widely held earlier views, recent experimental and theoretical studies have unambiguously shown that some ions adsorb to the air/water interface, with compelling evidence for enhanced surface concentrations of larger, more polarizable, weakly solvated anions.[7–10]

Recent advances have also revealed mechanistic details of the adsorption of the prototypical anion thiocyanate to air/water,[7,8] dodecanol/water,[11] and graphene/water[12] interfaces, focused on thermodynamic properties, viz. adsorption free energy, enthalpy, and entropy. While the mechanism of selective ion adsorption to the air/water interface has been shown to correlate strongly with ionic radii and hydration properties, considerable debate remains, with conflicting interpretations of theoretical models which can be significantly affected by the choices of parameters, initial conditions, thermodynamic constraints, and simulation sizes.[8,13–19]

To further our understanding of the behavior of ions at aqueous interfaces, directly measuring and interpreting detailed spectra of interfacial ions is of much interest. While several "surface sensitive" spectroscopic techniques are widely used in this context, their probe depths vary, ranging from the outermost few layers (*e.g.*, second-order nonlinear spectroscopy[7,20,21]) to greater than ca. 5 nm (*e.g.*, mass spectrometry,[22] photoelectron spectroscopy[23]) depending on experimental conditions.

Second-order nonlinear spectroscopy is a powerful tool in surface and interfacial spectroscopy.[24] Under the electric dipole approximation, the second-order nonlinear susceptibility ($\chi^{(2)}$) vanishes in centrosymmetric media, and second harmonic generation (SHG) and sum frequency generation (SFG) spectroscopies are surface-sensitive probes of the air/water interface with a probe depth of ca. 1 nm, corresponding to a few outermost monolayers.[24–26]

Our group has recently developed femtosecond broadband deep ultraviolet electronic sum frequency generation (DUV-ESFG) spectroscopy[27] which produces a broad, continuous, interfacial electronic $|\chi^{(2)}|^2$-spectrum in a single ultrafast measurement. Compared to time-consuming, error-prone pointwise measurements with resonant deep ultraviolet electronic second harmonic generation (DUV-ESHG) spectroscopy[7,28] developed by our group in the 2000s, broadband DUV-ESFG spectroscopy allows a more quantitative analysis of peak positions, linewidths, and relative intensities that can be directly compared with theoretical calculations to yield additional insights into the nature of ions at aqueous interfaces. When one or both of the input frequencies (ω_1, ω_2) and/or sum frequency ($\omega_{SF} = \omega_1 + \omega_2$) are resonant with an allowed transition(s), the detected SF signal can be strongly enhanced.[24]

The experimental design of broadband DUV-ESFG spectroscopy is based on the homodyne ESFG experiment of Yamaguchi & Tahara.[29] The experimental design is shown in Figure 1. A commercial Ti:Sapphire regenerative amplifier (Spitfire Ace, Spectra Physics) seeded by a Ti:Sapphire oscillator (Mai Tai, Spectra Physics) and pumped by an Nd:YLF laser (Empower,

Spectra Physics) is used to produce 800 nm, 100 fs pulses (1 kHz, 4 mJ/pulse). The output of the amplifier is split into two beam paths to generate the ω_1 and ω_2 pulses.

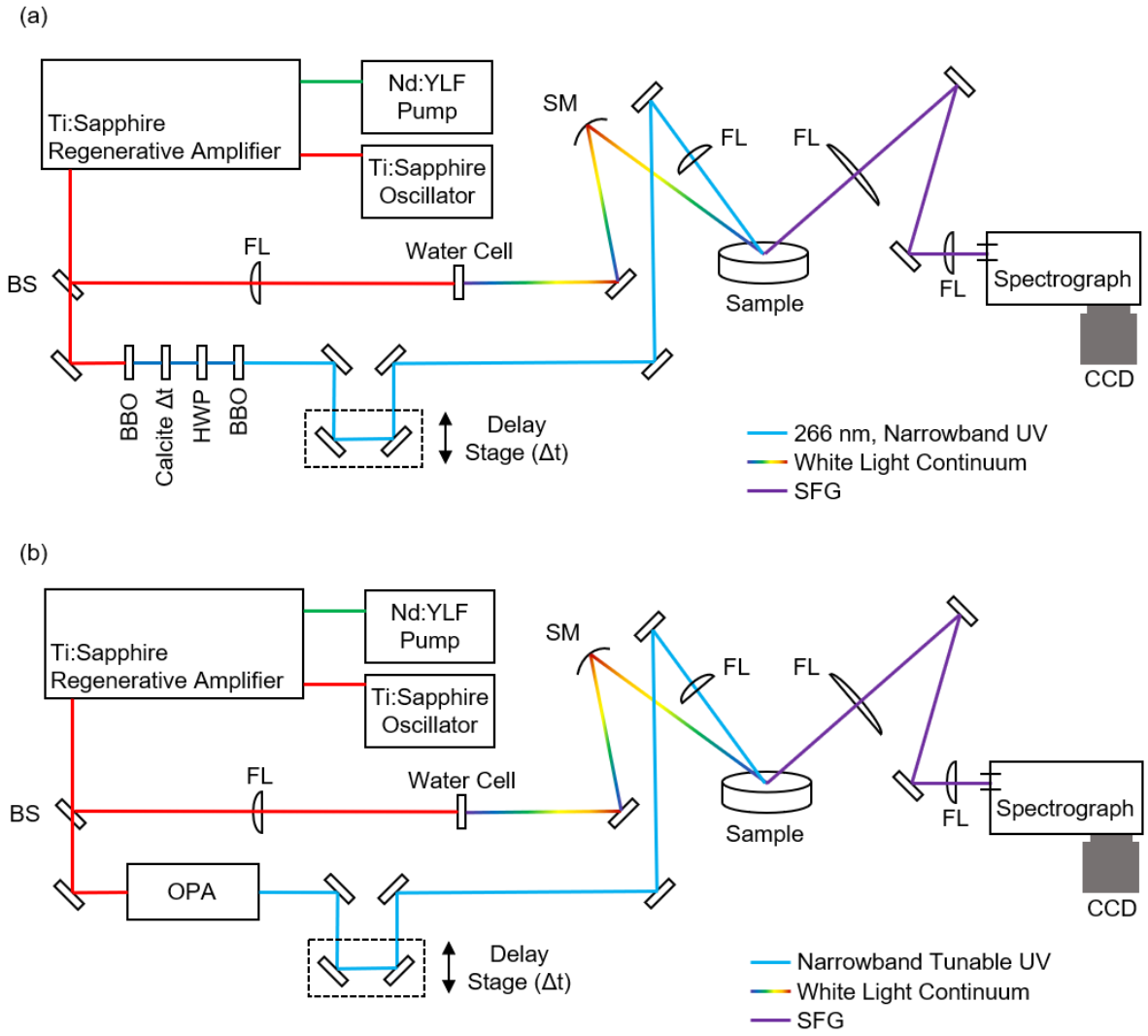

Figure 1. Experimental design for femtosecond broadband DUV-ESFG spectroscopy. The narrowband UV pulse (ω_1) can be generated by (a) a series of nonlinear crystals to obtain the frequency tripled fundamental at 267 nm or (b) a commercial optical parametric amplifier. (BS: beam splitter, BBO: β-barium borate crystal, Calcite Δt: calcite delay plate, HWP: 800-nm half-wave plate, OPA: optical parametric amplifier, SM: spherical mirror, FL: focusing lens, CCD: charge-coupled device camera)

A series of nonlinear crystals (Figure 1a) or an optical parametric amplifier (Figure 1b) is used to generate the narrowband UV pulse (ω_1). The frequency-tripled fundamental at 267 nm is generated by directing the 800 nm output of the amplifier through a β-barium borate (BBO) crystal, a calcite delay plate, an 800-nm half-wave plate, and a second BBO crystal. To generate a narrowband UV pulse at other frequencies, a commercial optical parametric amplifier (TOPAS Prime, Spectra Physics) is used. The ω_1 pulse is then directed through a bandpass filter and a time delay stage before being focused onto the solution surface using a lens at an angle of ca. 57° with respect to the surface normal.

To generate the broadband pulse (ω_2), the 800 nm output of the amplifier is attenuated and then directed through an 800-nm half-wave plate before being focused into a 5-mm quartz cell containing a continuous water flow to generate a white light continuum,[30] which is then directed through a 600-nm longpass filter (BLP01-594R-25, Semrock). The ω_2 pulse is then collimated and focused onto the sample surface using a spherical mirror to avoid chromatic aberration effects, at an angle of ca. 50° with respect to the surface normal.

When the ω_1 and ω_2 pulses are spatially and temporally overlapped at the solution surface, a coherent sum frequency (SF, ω_{SF}) signal is generated at the interface at the phase-matched angle. The reflected SF signal and fundamental beams are collimated by a UV fused silica plano-convex lens (LA4907, Thorlabs) and spatially filtered with an iris. The SF signal is then focused using a calcium fluoride plano-convex lens (PLCX-25.4-70.6-CFUV, CVI Laser Optics), passed through a bandpass filter, directed onto the entrance slit of a spectrograph (SP-300i, Princeton Instruments) with 500 grooves/mm and 240 nm blaze wavelength grating (53-069R, Richardson Gratings), and detected by a thermoelectrically cooled charge-coupled device camera (PIXIS 2KBUV, Princeton Instruments).

For all spectra presented herein, the background (*i.e.*, scattered light, CCD readout, and dark charge noise) is subtracted and baseline correction is performed. The background spectra are measured with a delay time of ca. 2 ps between the two incident pulses because there is no SFG without temporal overlap. The raw ESFG spectra are normalized by the non-resonant SFG spectrum of gallium arsenide (GaAs) or z-cut quartz (ZCQ), to correct for distortion in the raw ESFG spectra due to the spectral intensity and positive temporal chirp of the white light continuum (ω_2) pulse and the spectral sensitivities of the optics and CCD detector. The non-resonant SFG spectra and raw ESFG spectra are acquired under the same experimental conditions.

Under the two-photon on-resonance, one-photon off-resonance condition of broadband DUV-ESFG spectroscopy employed herein, the normalized intensity (I_{ESFG}) can be expressed as

$$I_{\mathrm{ESFG}} \propto \left|\chi^{(2)}\right|^2 \propto \sum_n \frac{\left|\mu_{0n}(\alpha_{0n})_{\mathrm{TPA}}\right|^2}{(\omega_n - \omega_{\mathrm{SFG}})^2 + \Gamma_n^2}$$

where $\chi^{(2)}$ is the second-order nonlinear susceptibility, μ_{0n} is the transition dipole matrix element and $(\alpha_{0n})_{TPA}$ is the two-photon absorption polarizability tensor element connecting the ground state and excited state n, Γ_n is the linewidth of the transition, ω_n is the transition energy between the ground and excited state n, and ω_{SFG} is the sum frequency of the incident photons.[31] By plotting $|\chi^{(2)}|^2$ vs. ω_{SFG}, the interfacial electronic $|\chi^{(2)}|^2$-power spectrum is obtained. The non-resonant background signal from the solvent is assumed to be negligibly weak because no SFG signal is observed from neat water.

Chapter 2 Interfacial Charge-Transfer-to-Solvent Spectrum of Aqueous Thiocyanate

Adapted with permission from Mizuno, H.; Rizzuto, A. M.; Saykally, R. J. "Charge-Transfer-to-Solvent Spectrum of Thiocyanate at the Air/Water Interface Measured by Broadband Deep Ultraviolet Electronic Sum Frequency Generation Spectroscopy." *J. Phys. Chem. Lett.,* **2018**, *9* (16), 4753–57. Copyright (2018) American Chemical Society.[32]

Introduction

In investigating the behavior of halides, pseudohalides, and biologically relevant anions in aqueous systems, many studies have focused on charge-transfer-to-solvent (CTTS) transitions—the precursors of solvated electrons.[33–39] CTTS states are short-lived excited states that comprise a neutral parent atom and an excited electron in a dipole bound state supported by the surrounding solvent network. Because the initial and final states are defined by the parent ion and its corresponding neutral species, as well as the surrounding solvent molecules, CTTS spectra are highly sensitive to the local environment, *e.g.*, solvation, temperature, pressure, and electrolytes.[33,37,40,41] CTTS spectra of anions typically comprises broad, intense, and typically featureless bands in the deep UV (< 250 nm).[33] The high sensitivity to the local chemical environment and large extinction coefficients of CTTS transitions make them excellent probes of anion solvation dynamics in complex systems. Here, we report the interfacial CTTS spectrum of aqueous thiocyanate at the air/water interface.

Thiocyanate (SCN^-) is a highly surface-active anion and one of the most chaotropic in the anion Hofmeister series.[6,42]

$$CO_3^{2-} > SO_4^{2-} > S_2O_3^{2-} > H_2PO_4^- > F^- > Cl^- > Br^- \sim NO_3^- > I^- > ClO_4^- > SCN^-$$

The asymmetric solvation shell of thiocyanate, a linear triatomic ion (Figure 2), differs from those of often studied halides and other ions (*e.g.*, I^-, NO_3^-, CO_3^{2-}) that possess symmetric structures and charge distributions.

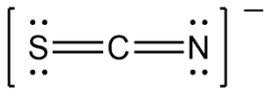

Figure 2. Lewis structure of thiocyanate ion.

The bulk aqueous CTTS spectrum of 100 μM sodium thiocyanate (NaSCN) is shown in Figure 4a. Fox et al. measured the bulk absorption spectrum of aqueous tetramethylammonium thiocyanate ($N(CH_3)_4SCN$) and assigned two bands in the deep UV, viz. a higher energy band centered near 187 nm and a lower energy band centered at 216 nm, with no observed cation dependence at low concentrations.[43] Solvent and temperature dependence properties were used to assign the lower energy band as a CTTS transition.[44] The higher energy band resembles similar higher energy bands observed in CTTS spectra of halides.[45] Thus, the higher energy band is proposed to originate from higher energy solvated electron states or higher states of the corresponding thiocyanate radical.[43] Upon irradiation with UV wavelengths, two competing photochemical pathways, depending on the incident wavelengths, are proposed:

$$SCN^-(aq) \xrightarrow{\lambda<240\ nm} [SCN^-(aq)]^* \rightarrow SCN(aq) + e^-(aq)$$

$$SCN^-(aq) \xrightarrow{\lambda>240\ nm} CN^-(aq) + \cdot S(aq)$$

wherein first is an external CTTS transition and the latter is an intramolecular transition.[46]

Materials and Methods

Sodium thiocyanate was obtained from J.T. Baker (≥98.0%, ACS Reagent, Baker Analyzed).

For bulk measurements, the salt was used as is and dissolved in ultrapure water (18.2 MΩ.cm at 25 °C, TOC < 5 ppb, Milli-Q, EMD Millipore). The bulk UV-Vis absorption spectrum of sodium thiocyanate was measured using a UV-Vis spectrophotometer (UV-2600, SHIMADZU) in a 10-mm pathlength quartz cuvette at a bulk concentration of 100 μM.

For interfacial measurements, solutions were prepared in glassware soaked in NOCHROMIX (Godax Laboratories, Inc.) and concentrated sulfuric acid solution overnight and rinsed with copious amounts of ultrapure water. Sodium thiocyanate was baked in an oven overnight prior to being dissolved in ultrapure water and allowed to equilibrate to room temperature (293 K) before spectroscopic measurements. The sample solutions were contained in a Teflon Petri dish during the measurement. Each sample was limited to 120 seconds of laser exposure time to reduce effects of photodegradation, photoproduct formation, and surface contamination by airborne particulates. The broadband DUV-ESFG spectra was measured with *ppp*-polarization scheme (*p*-polarized SFG, *p*-polarized 266 nm, and *p*-polarized white light continuum) using the experimental setup described in Chapter 1.

Results and Discussion

Figure 3 shows the unnormalized broadband DUV-ESFG spectra of interfacial thiocyanate at the air/water interface and the non-resonant SFG spectra of gallium arsenide (GaAs). To obtain the $|\chi^{(2)}|^2$-spectra, the thiocyanate spectra are normalized by the GaAs spectra measured under identical conditions. Due to the positive chirp in the white light continuum generation process of the ω_2 pulse,[30] spectral overlap with shorter and longer wavelength components of the white light continuum were obtained by adjusting the time delay (±60 fs) between the two input pulses.

Figure 4 compares the bulk linear absorption spectrum and the interfacial $|\chi^{(2)}|^2$-spectra obtained by broadband DUV-ESFG spectroscopy and previously measured pointwise resonant DUV-ESHG spectra.[7] Compared to the pointwise ESHG spectra obtained at five different input frequencies at molar concentrations (1-3 M) by Petersen et al.,[7] the broadband DUV-ESFG spectrum ($[NaSCN]_{bulk}$ = 3 M) is consistent and of much higher quality. The most striking difference is that the lower energy CTTS band observed in the bulk spectrum is not observed at the air/water interface. This can be attributed to differences in the local solvation environment and/or selection rules which will be further discussed below.

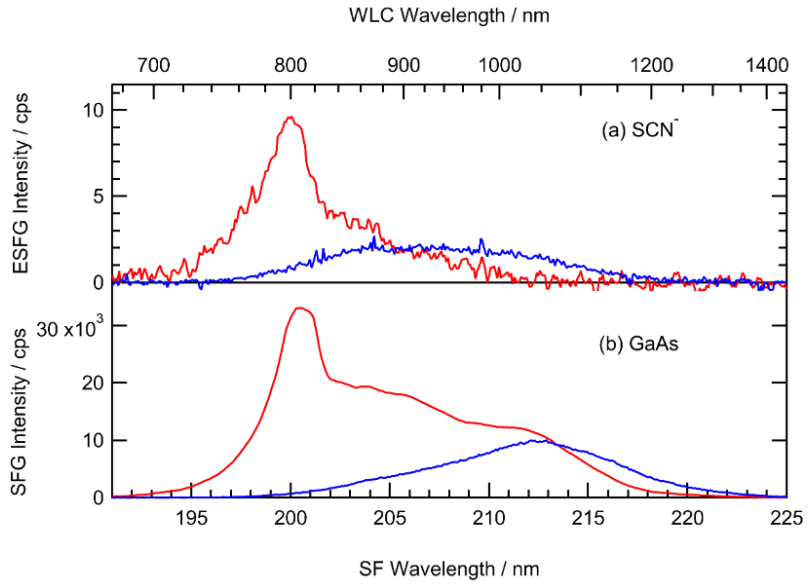

Figure 3. (a) Unnormalized broadband DUV-ESFG spectra of 3 M aqueous sodium thiocyanate measured at 293 K. (b) Non-resonant SFG spectrum of gallium arsenide. Red (λ_{WLC} = 700-1200 nm) and blue (λ_{WLC} = 800-1400 nm) lines indicate spectra measured with different time delay between the two incident pulses corresponding to different spectral overlap due to the positive chirp of the white light continuum pulse. The top axis corresponds to the wavelength of the white light continuum pulse mixing with the narrowband 266 nm pulse (ω_1) to generate the sum frequency at the wavelength on the bottom axis.

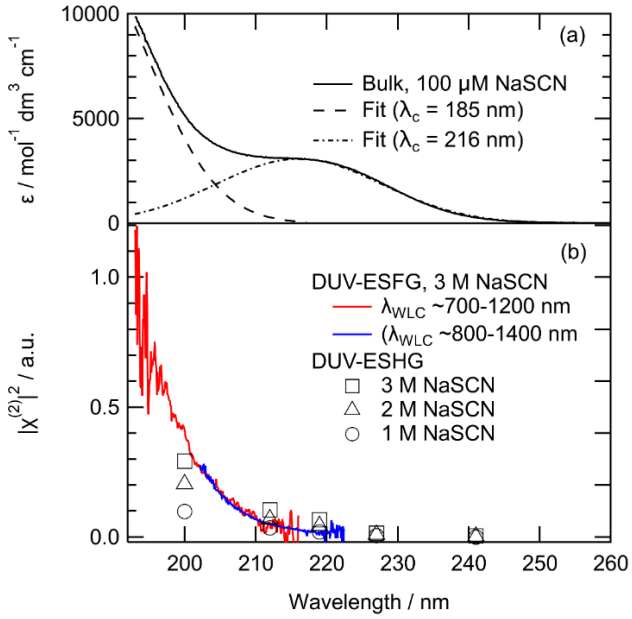

Figure 4. (a) Bulk charge-transfer-to-solvent (CTTS) spectrum of 100 µM aqueous sodium thiocyanate measured at 293 K. Dotted black lines indicate Gaussian fits centered at 185 nm and 216 nm. (b) Interfacial $|\chi^{(2)}|^2$-spectra of aqueous thiocyanate CTTS measured by resonant DUV-ESHG (200, 212, 219, 227, and 241 nm; 1-3 M, black markers)[7] and broadband DUV-ESFG (3 M, red and blue solid lines) spectroscopy. The red and blue lines indicate spectra measured with different time delay of the two input pulses corresponding to different spectral overlap due to the positive chirp of the white light continuum pulse.

The interfacial solvation environment of thiocyanate is distinctly different from that of the bulk. In bulk solution, neutron diffraction experiments predict an eggshell-like solvation shell with 2-3 water molecules hydrogen bonded to N and weakly correlated to S at 1-3 M concentrations with no significant concentration dependence.[47] *Ab initio* calculations with DFT-based interaction potentials predict the local solvation around the S-terminus to resemble that of iodide and around the N-terminus to be similar to fluoride.[48]

As thiocyanate repartitions from the bulk to the interface region, it will shed water molecules from its solvation shell. Additionally, thiocyanate is also predicted to alter its charge distribution as the ion moves to the interface.[48] Furthermore, thiocyanate also possesses an asymmetry and a significant dipole moment that drives the ion to favorable orientations at aqueous interfaces. Previous experiments that probed the thiocyanate C−N stretch by homodyne-detected vibrational SFG spectroscopy predict an average tilt angle of 45° with respect to the surface normal at the air/water interface, although the absolute orientation was unable to be determined.[49,50] A recent MD study predicts that the S-terminus has a greater affinity for the interface than does the N-terminus, yielding an average tilt angle of 45° in the outermost surface layer, but more perpendicularly oriented with respect to the surface in the subsurface region (0.1-0.5 nm).[51] The different solvation environments experienced by the thiocyanate ion at the air/water interface likely contributes to the observed spectral differences.

Another key difference between the bulk and interfacial spectra presented here are the ion concentrations. At the bulk concentration (3 M) in DUV-ESFG measurements, the ratio of all ions to water molecules is ca. 1:10; thus, ion-ion effects are expected to be present. These ion-ion interactions can influence the electronic states involved in the CTTS transitions and the water hydrogen bonding structure in the interfacial region. At the interface, the dielectric constant is lower than that of the bulk;[52] thus, there is a stronger propensity for ions to form contact ion pairs, solvent separated ion pairs, and ion clusters. Simulations have predicted unexpected water-bridged configurations at high ion concentrations at and near the interface, wherein a few hydration water molecules are shared by *like-charged ions*.[53] In the bulk, ultrafast 2D infrared pump-probe experiments have shown evidence of ion cluster formation at concentrations greater than ca. 10^{-3} M in aqueous thiocyanate solutions.[54] For a 2 M potassium thiocyanate solution, ca. 35% of thiocyanate anions in bulk were reported to be present in some cluster form, with dilute solutions having fewer, smaller, and tighter ion clusters.[54] Gas phase cluster experiments also support the existence of ion clusters in concentrated aqueous sodium thiocyanate solutions.[55] Vibrational SFG spectroscopy measurements that probed the water O−H stretch suggest the presence of thiocyanate strongly perturbs the interfacial hydrogen bonding network.[49,50] Moreover, the induced ordering of water molecules due to the formation of an electric double layer at the air/water interface[56,57] may also contribute to the differences in bulk and interfacial CTTS spectra.

Broadband DUV-ESFG spectra of 3 M aqueous potassium thiocyanate (KSCN) showed nearly identical interfacial CTTS spectra to that of the sodium salt (NaSCN). Thus, *cation* effects on interfacial CTTS spectra appear to be minimal between sodium and potassium; this is consistent with molecular dynamics simulations by Tesei et al. at high concentrations (ca. 5 M) that predicted cations (Na^+, K^+) to have negligible influence on the interfacial properties of thiocyanate at the air/water interface.[51] However, lithium or cesium may show stronger cation effects due to the larger differences in ionic radii and charge densities. Recent homodyne-detected vibrational SFG measurements by Hao et al. probing the C−N stretch of thiocyanate suggest cation effects manifest

in the tilt angle of thiocyanate at higher concentrations.[58] However, this result could be due to variations in probe depths at higher concentrations as the interfacial thickness is expected to increase at higher salt concentration which can complicate the interpretation of vibrational SFG spectra. As previously predicted by a theoretical study, there may be depth dependence in the orientation of thiocyanate near the interface.[51] Further experimental and theoretical studies are necessary to elucidate the cation effects on the interfacial spectrum of thiocyanate and its implications for selective ion adsorption at aqueous interfaces.

The upper limit of concentrations used for broadband DUV-ESFG measurements is limited by formation of photoproducts leading to turbidity in the solution and concomitant signal interference. Upon UV irradiation of solutions with bulk concentrations greater than 3 M, formation of sulfur oligomers and elemental sulfur has been observed,[46,59] consistent with the second reaction in the photochemical scheme presented above. On the other hand, the lower limit of usable concentration is established by the ESFG signal intensity and acquisition time. Because SFG is a second-order process, the signal is inherently weak and reducing the bulk concentration below 3 M would lower the signal count, leading to decreased signal-to-noise ratio of the spectra. Longer acquisition times would increase the possibility of introducing contaminants from the lab environment (*e.g.*, oils, dust particles) that would affect the ESFG signal from the solution interface. The use of a flat jet system[60] (Chapter 6) is a promising direction as it would allow for a continuously refreshing surface and longer acquisition times at lower concentrations.

From a selection rule standpoint, in the two-photon resonant, one-photon non-resonant case for broadband DUV-ESFG spectroscopy as used here, the normalized ESFG intensity is proportional to the square modulus of the product of the transition moment (μ_{0n}) and the two-photon absorption polarizability tensor ((α_{0n})$_{\mathrm{TPA}}$):[31]

$$I_{\mathrm{ESFG}} \propto \left|\chi^{(2)}\right|^2 \propto \sum_n \frac{\left|\mu_{0n}(\alpha_{0n})_{\mathrm{TPA}}\right|^2}{(\omega_{\mathrm{CTTS}} - \omega_{\mathrm{SFG}})^2 + \Gamma_{\mathrm{CTTS}}^2}$$

For thiocyanate at the air/water interface, the ground and/or excited states corresponding to the CTTS transitions may be shifted due to the different local solvation environments and/or the charge distribution within the ion as discussed above. This could lead to significant changes in the numerator of the above expression and would be consistent with the observed differences between the bulk and interfacial spectra. The increased inhomogeneity of solvation environments[61] and orientational constraints in the interfacial region[49–51,58] may also affect the population distribution of the ground and excited states of the thiocyanate ion.

Conclusions

In light of the results presented here, previously reported results for the thermodynamics associated with thiocyanate adsorption to aqueous interfaces obtained via pointwise ESHG spectroscopy measurements as a function of concentration and fit to a Langmuir adsorption model[7,8,11,12] should be re-examined to determine if the spectral changes observed herein may have affected the interpretation of those data. In resonant ESHG spectroscopy, as developed in our group, the CTTS transition is two-photon resonant with the second harmonic of the input fundamental frequency.[28] The Langmuir adsorption model assumes that the orientation of surface species and the magnitude of the microscopic nonlinear polarizability remain constant over the

entire concentration range and that multiple adsorbing species do not interact with each other, which may not be valid at molar concentrations.[7,28]

Furthermore, as discussed above, thiocyanate clusters are reported to form in bulk solution at moderate to high concentrations ($> 10^{-3}$ M).[54] Formation of contact ion pairs, solvent separated pairs, and clusters in the interfacial region could result in non-negligible ion-ion effects and concentration dependence in the measured free energy, enthalpy, and entropy of adsorption. In other words, thiocyanate in very dilute solution may have different thermodynamic driving forces for interfacial adsorption compared to a higher concentration solution wherein significant ion-ion interactions and perturbations to the water structure are present.

Though the exact physical origins of the observed differences in the interfacial and bulk CTTS spectra of thiocyanate are not yet certain, it is clear that concentration dependent parameters to account for ion-ion interactions are necessary in elucidating the complex thermodynamics associated with ion adsorption at aqueous interfaces. Further experiments and associated theoretical studies are necessary to extract the interesting chemical details responsible for these salient observations.

Chapter 3 New Insights into the Charge-Transfer-to-Solvent Spectrum of Aqueous Iodide: Surface vs. Bulk

Adapted with permission from Bhattacharyya, D.[#]; Mizuno, H.[#]; Rizzuto, A. M.; Zhang, Y.; Saykally, R. J.; Bradforth, S. E. "New Insights into the Charge-Transfer-to-Solvent Spectrum of Aqueous Iodide: Surface vs. Bulk." *J. Phys. Chem. Lett.*, **2020**, *11* (5), 1656-1661. Copyright (2020) American Chemical Society.[62]

[#]These authors contributed equally. Two-photon absorption spectra were measured by the Bradforth Group at University of Southern California.

Introduction

In investigating the behavior of halides, pseudohalides, and biologically relevant anions in aqueous systems, many studies have focused on charge-transfer-to-solvent (CTTS) transitions—the precursors of solvated electrons.[33–39] CTTS states are short-lived excited states that comprise a neutral parent atom and an excited electron in a dipole bound state supported by the surrounding solvent network. Because the initial and final states are defined by the parent ion and the surrounding solvent, CTTS spectra are highly sensitive to the environment.[33,37,40,41] Excitation to a CTTS state can lead to the formation of solvated electrons with high quantum yield;[63,64] the high sensitivity to the local environment and large extinction coefficients of CTTS transitions make them excellent probes of anion solvation dynamics in complex systems.

Iodide (I^-) has served as a prototypical anion in probing local solvation structure due to its favorable spectroscopic properties. The lowest energy CTTS transitions of iodide in the deep UV wavelengths (~190-260 nm) are relatively easily accessible experimentally, as compared to those of lighter halides that exhibit CTTS bands at higher energies. Furthermore, iodide is a spherical, monoatomic anion with only electronic degrees of freedom, thus making theoretical calculations and modeling more straightforward than for polyatomic ions, which become further complicated by the presence of overlapping intramolecular valence excitations and orientational effects.

At room temperature, the bulk one-photon absorption (1PA) spectrum of the aqueous iodide CTTS band exhibits well-resolved doublet components at 226 nm (5.5 eV) and 193 nm (6.4 eV) with similar intensities (Figure 5).[65] Because the doublet splitting roughly matches the energy difference (0.9 eV) between the ground state ($^2P_{3/2}$) and spin-orbit excited state ($^2P_{1/2}$) of the neutral iodine atom (I), they are commonly referred to as "J=3/2" and "J=1/2" bands, respectively. Previously, the 1PA spectrum has been fit with sets of overlapping log-normal bands derived from spectra in various solvents and conditions, suggesting that the iodide CTTS spectrum consists of several additional overlapping transitions at higher energies (Figure 5).[45,66,67] The higher energy bands have not yet been assigned definitively, but are speculated to arise from higher-lying CTTS excited states.[45,66] Here, we focus on elucidating the nature of the transitions that make up these CTTS bands.

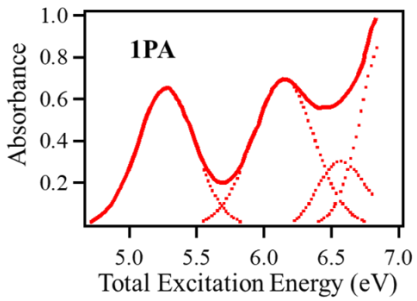

Figure 5. Bulk one-photon absorption spectrum of the charge-transfer-to-solvent bands of aqueous tetramethylammonium iodide at 318 K (solid red curve).[45] Dotted lines are log-normal bands used to deconvolute the overall absorption spectrum into individual CTTS bands. The lowest energy bands are commonly referred to as "J=3/2" and "J=1/2" bands.

Resonant one-photon excitation into the lower energy CTTS band (J=3/2) detaches an electron on a 200-fs time scale, which in turn, relaxes in ~800 fs,[68,69] consistent with theoretical results from Sheu & Rossky.[70,71] Upon resonant one-photon excitation into the higher-lying CTTS state (J=1/2), an additional autodetachment channel for hydrated electron formation is proposed,[72] characterized by a different electron ejection length compared to the lower energy J=3/2 band.[73,74]

Phase-sensitive transient ESHG spectroscopy measurements by Verlet and co-workers reveal that the lower CTTS state of iodide at the air/water interface is asymmetrically solvated in the plane of the surface and that the electron solvation dynamics at the interface are very similar to those observed in the bulk, although slightly faster.[75,76] The asymmetry of the lowest CTTS wavefunction arising from the thermal fluctuation of the local solvation environment is also predicted by Bradforth & Jungwirth.[73] Their calculations suggest that the lowest CTTS states comprise a mixture of valence *s* (~30%), diffuse *s* (~50%), and *p* (~17%) type orbitals. This result contrasts with the calculations by Sheu & Rossky that predicted ~45-80% *d* orbital character in the lowest CTTS states.[77] This discrepancy most likely arises from the one-electron model used by Sheu & Rossky which did not account for all valence shell electrons of iodide,[77] resulting in artificial lowering of the virtual *d* orbitals. The Configuration Interaction Singles (CIS) calculation by Bradforth & Jungwirth[73] in fact predicted promotions involving orbitals with considerable *d* orbital character are situated much higher in energy compared to the lowest CTTS states.

Although the lowest energy CTTS transition of aqueous iodide has been studied extensively using linear absorption spectroscopy (*i.e.*, 1PA spectroscopy), very little is known about the character of the higher lying CTTS states because of their overlapping nature and the onset of the lowest-lying water electronic absorption (ca. 6.4 eV). The latter increasingly interferes with the shorter wavelength region of 1PA spectra.[41] Herein, we present aqueous iodide CTTS spectra measured with interface-sensitive femtosecond broadband DUV-ESFG spectroscopy and bulk-sensitive two-photon absorption (2PA) spectroscopy, and discuss the salient selection rules and symmetry arguments within a Rydberg transition model to provide insight into the aqueous iodide CTTS spectrum, specifically in the region of overlapping transitions. Moreover, the interference from water electronic absorption is avoided by virtue of using nonlinear processes to access the halide electronic absorption. None of the input photon energies overlaps with the onset of water electronic absorption and the 2PA threshold for bulk water absorption lies even higher in energy (ca. 7.8 eV) as shown previously,[78] indicating that water is two-photon transparent in the energy region explored in this work.

Materials and Methods

Sodium iodide (ACS Reagent ≥ 99.5%) was obtained from Sigma-Aldrich.

The detailed experimental design for broadband DUV-ESFG spectroscopy is presented in Chapter 1. Briefly, a narrowband 100-fs tunable UV pulse (ω_1) is spatially and temporally overlapped with a white light continuum pulse (ω_2) at the solution surface, generating coherent sum frequency ($\omega_{SFG} = \omega_1 + \omega_2$) photons at the phase-matched angle in reflection geometry. The white light continuum pulse enables the acquisition of a broadband spectrum in a single measurement without having to tune the input frequencies. The broadband DUV-ESFG spectra were measured with *ppp*-polarization scheme (*p*-polarized SFG, *p*-polarized UV, and *p*-polarized white light continuum) using the experimental setup described in Chapter 1. Spectra were measured with ω_1 = 267 nm and 295 nm, $\omega_2 \approx$ 600-1400 nm.

For interfacial spectra measurements, solutions were prepared in glassware soaked in NOCHROMIX (Godax Laboratories, Inc.) and concentrated sulfuric acid solution overnight and rinsed with copious amounts of ultrapure water (18.2 MΩ.cm at 25 °C, TOC < 5 ppb, Milli-Q, EMD Millipore). Sodium iodide was baked in an oven overnight prior to being dissolved in ultrapure water and allowed to equilibrate to room temperature (293 K) before spectroscopic measurements. The sample solutions were contained in a Teflon Petri dish during the measurement. Each sample was limited to 120 seconds of laser exposure time to reduce effects of photodegradation, photoproduct formation, and contamination of the solution surface by airborne particulates.

For bulk 2PA spectra measurements performed by the Bradforth Group, two different pump wavelengths (266 and 400 nm) were mixed with the visible portion of the white light continuum (~310-700 nm) to cover the spectral range of the iodide CTTS doublet. Both pump and probe beams were overlapped spatially and temporally on a wire-guided gravity jet.[79] Differential absorbance (ΔA) of the broadband continuum probe was recorded with and without the pump pulse using a 256-channel silicon photodiode array. The detailed experimental design is described elsewhere.[78,80]

Results and Discussion

Pointwise interfacial $|\chi^{(2)}|^2$-spectra of iodide were measured with resonant DUV-ESHG spectroscopy developed in the Saykally Group in 2006.[81] By fitting to a Langmuir adsorption model, Petersen & Saykally obtained the Gibbs free energies of adsorption (ΔG_{ads}) for iodide at the air/water interface to be −6.1 ± 0.2 and −6.3 ± 0.2 kcal/mol for sodium iodide and potassium iodide, respectively.[82] However, noisy, time-consuming, and error-prone pointwise ESHG spectra present a challenge for quantitative analysis of spectral shapes and shifts. Our group also previously published CTTS spectrum of iodide ($[NaI]_{bulk}$ = 5 M) at the air/water interface measured by broadband DUV-ESFG spectroscopy with ω_1 = 266 nm and $\omega_2 \approx$ 600-1400 nm. The interfacial $|\chi^{(2)}|^2$-spectrum (Figure 6b, red) revealed a small redshift of the CTTS doublet, a slight narrowing of the linewidths, and a large relative intensity difference between the upper (J=1/2) and lower (J=3/2) CTTS bands compared to the bulk 1PA spectrum (Figure 6a).[27] In the present work, we supplement this $|\chi^{(2)}|^2$-spectra with broadband DUV-ESFG spectra measured with ω_1 = 295 nm.

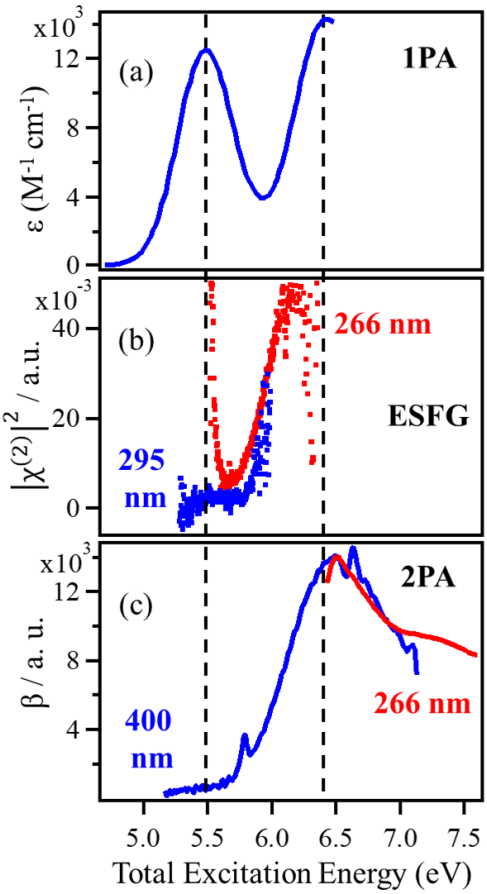

Figure 6. Charge-transfer-to-solvent spectra of aqueous iodide. (a) 1PA spectrum of potassium iodide in water at 298 K. The literature deconvolution of the overall absorption spectrum into individual CTTS bands is shown in Figure 5. The vertical dashed lines correspond to the 1PA peak positions for the two lowest CTTS transitions at 298 K and 1 atm for aqueous iodide. (b) Normalized DUV-ESFG spectra of aqueous sodium iodide for two different pump wavelengths (ω_1 = 266 nm and ω_1 = 295 nm, $\omega_2 \approx$ 600-1400 nm; $[NaI]_{bulk}$ = 5 M) measured at 293 K. For ω_1 = 266 nm pump, the ESFG data is truncated in the lower energy region. (c) 2PA spectra of aqueous sodium iodide for two different pump wavelengths (ω_1 = 266 nm and ω_1 = 400 nm, $\omega_2 \approx$ 310-700 nm; $[NaI]_{bulk}$ = 700 mM) measured at 293 K. The sharp features in the 400 nm pump 2PA spectrum are due to the instantaneous Raman signals from water.

The interfacial $|\chi^{(2)}|^2$-spectrum measured with ω_1 = 295 nm and $\omega_2 \approx$ 600-1400 nm exhibits no significant resonance enhancement for the lower (J=3/2) CTTS band under the strictly two-photon resonance condition (Figure 6b, blue) where the intensity of the normalized SFG intensity can be expressed as

$$I \propto \left|\chi^{(2)}\right|^2 \propto \sum_n \frac{|\mu_{0n}(\alpha_{0n})_{2PA}|^2}{(\omega_{CTTS} - \omega_1 - \omega_2)^2 + \Gamma_{CTTS}^2}$$

where $\chi^{(2)}$ is the 2nd-order nonlinear susceptibility, μ_{0n} is the 1PA transition dipole matrix element and $(\alpha_{0n})_{2PA}$ is the 2PA polarizability tensor element connecting the ground state to excited state n, Γ_{CTTS} is the linewidth of the CTTS transition, ω_{CTTS} is the transition energy between the ground state and CTTS excited state, and ω_1 and ω_2 are the frequencies of the input radiations. Under the

one-photon off-resonance two-photon on-resonance ESFG spectroscopy condition here, the selection rules require that the transition be simultaneously active for both 1PA and 2PA.[31,83] Hence, large relative intensity difference observed in the previously reported ESFG spectrum (ω_1 = 266 nm) is attributed to a double resonance effect, wherein the narrowband ω_1 pulse is also one-photon resonant with the tail of the J=3/2 CTTS band, leading to an additional resonance enhancement term in the denominator as shown in the equation below:[31,83]

$$I_{\mathrm{ESFG}} \propto \left|\chi^{(2)}\right|^2 \propto \sum_n \frac{\left|\mu_{0n}(\alpha_{0n})_{2\mathrm{PA}}\right|^2}{[(\omega_{\mathrm{CTTS}} - \omega_1 - \omega_2)^2 + \Gamma_{\mathrm{CTTS}}^2][(\omega_{\mathrm{CTTS}} - \omega_1)^2 + \Gamma_{\mathrm{CTTS}}^2]}$$

This is consistent with the fact that aqueous iodide has been used as a precursor of solvated electrons by employing a 266 nm laser to excite the lower energy CTTS band.[84,85]

The fact that the J=3/2 CTTS band of iodide has no ESFG intensity under the strictly two-photon resonant condition (ω_1 = 295 nm), suggests that the transition must be two-photon inactive. To verify this hypothesis, broadband 2PA spectra of 700 mM bulk aqueous sodium iodide solution were measured (Figure 6c). Interestingly, continuous 2PA spectra have not been reported before for any aqueous alkali halide salt. Although the 1PA spectrum shows similar intensities for the J=3/2 and J=1/2 bands, the former is absent in the 2PA spectra, consistent with the broadband ESFG interfacial spectra presented above. The nature of the orbital excitations resulting in the CTTS transitions in aqueous iodide and the reasons for the absence of the lowest CTTS band in 2PA are discussed below.

Several studies dating back to work by Franck & Scheibe[86] suggest that the promoted electron in the vertical excited state of aqueous iodide is spatially extended over the solvent shell but still centered on the parent iodine atom.[87,88] Hence, in the simple Rydberg transition model,[89] the excited electronic configuration is [Kr]4d^{10}5$s^2$5$p^5$6s^1 which gives rise to four excited states: $^3P_2$, $^3P_1$, $^3P_0$ and $^1P_1$, in the Russell-Saunders (R-S) coupling limit (Figure 7a). However, for a heavy atom like iodine, the significance of the R-S term symbols is obscured because the orbital angular momentum (L) and spin angular momentum (S) are no longer good quantum numbers. Instead, the *jj*-coupling language is more relevant and the total angular momentum (J = L + S) should be used to more accurately describe the atomic energy levels.[90]

In the *jj*-coupling limit, the selection rule for 1PA requires $\Delta J = 0, \pm 1$ with the restriction that the transition between J = 0 to J = 0 state is not allowed, and for 2PA, $\Delta J = 0, \pm 1, \pm 2$ holds. From the J = 0 ground state of iodide, 1PA transitions to both upper and lower spin-orbit split components are allowed (Figure 7b, red arrows).[90] The selection rules further dictate that both of these transitions would also be allowed in 2PA, which fails to explain our experimental findings. However, it is also important to consider the parity of the states involved in the electronic transitions. We resort to the spectroscopic database compiled by Moore,[91] wherein the excited state energies and their corresponding term symbol notations for xenon are tabulated (Table 1).

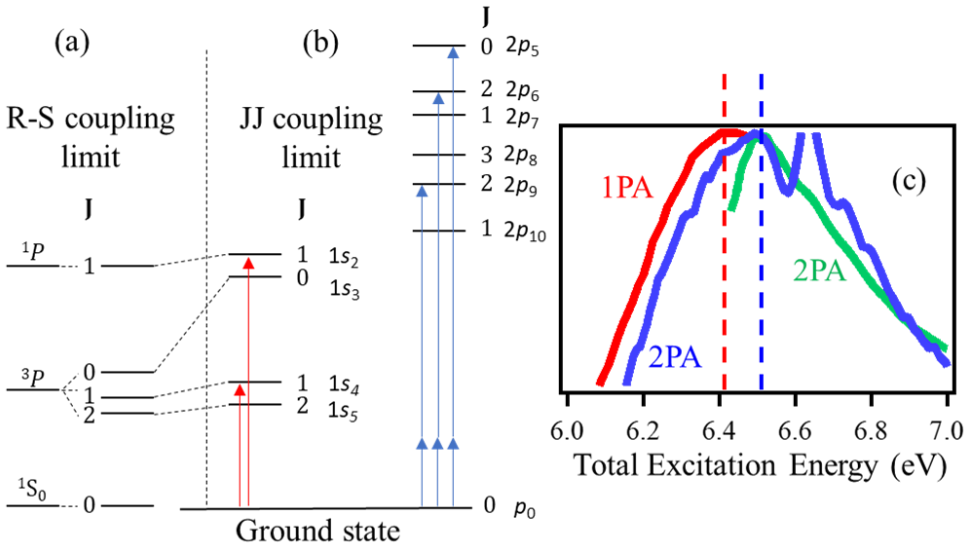

Figure 7. Energy levels of xenon (isoelectronic with iodide); transitions from ground to excited states are also shown (arrows).[92] Two different coupling schemes are shown: (a) R-S coupling and (b) J-J coupling. The Paschen notations, as shown in Table 1, are used to designate the energy levels. The red arrows and the blue arrows are used to show the 1PA and 2PA excitations, respectively. (c) The 1PA and 2PA spectra of aqueous iodide are zoomed-in to the region of the higher energy CTTS transition to clearly show the shift in the peak position. The 1PA spectrum is reproduced from Ref.[41] measured at 298 K and 250 bar.

Table 1. Electronic excited states of xenon as adapted from the database compiled by Moore.[91]

Paschen Notation	Configuration	Designation		J	Energy (eV)
p_0	$5p^6$	$5p^6$	^{1}S	0	0.00
$1s_5$	$5p^5(^2P^o_{1½})6s$	6*s*	[1½]^o	2	8.32
$1s_4$				1	8.44
$1s_3$	$5p^5(^2P^o_{0½})6s$	6s′	[0½]^o	0	9.45
$1s_2$				1	9.57
$2p_{10}$	$5p^5(^2P^o_{1½})6p$	6*p*	[0½]	1	9.58
$2p_9$	″	6*p*	[2½]	2	9.69
$2p_8$	″	6*p*		3	9.72
$2p_7$	″	6*p*	[1½]	1	9.79
$2p_6$	″	6*p*		2	9.82
$2p_5$	″	6*p*	[0½]	0	9.93
$2p_4$	$5p^5(^2P^o_{0½})6p$	6p′	[1½]	1	10.96
$2p_3$	″	6p′		2	11.05
$2p_2$	″	6p′	[0½]	1	11.07
$2p_1$	″	6p′		0	11.14

Since iodide (I^-) is isoelectronic with xenon (Xe), the energy ordering of the excited states and the corresponding term symbols are similar in both cases. The ground state of xenon is of even parity. The overall parities of the excited states corresponding to $5p^5(^2P_{3/2})6s$ ($6s[3/2]^o_{2,1}$) and $5p^5(^2P_{1/2})6s$ ($6s'[1/2]^o_{0,1}$) electronic configurations are odd, which dictates that both transitions should be 1PA allowed and 2PA inactive (the superscript (^{o}) indicates the overall odd parity of the excited state wavefunction, Table 1). The presence of $^1S_0 \rightarrow 5p^5(^2P_{3/2})6s$ transition in the three-photon excitation of xenon further supports this parity argument, as 1PA and 3PA excitations follow similar selection rules.[93] This means that transitions to the $5p^5(^2P_{3/2})6s$ ($6s[3/2]^o_{2,1}$) or $5p^5(^2P_{1/2})6s$ ($6s'[1/2]^o_{0,1}$) state is not responsible for the band centered at ~6.5 eV in the 2PA spectra of aqueous iodide. However, excited states corresponding to the $5p^5(^2P_{3/2})6p$ electronic configurations are of even parity and hence, transitions to these states (particularly the J = 2 and J = 0 subcomponents) from the ground state are 2PA parity allowed. Moore's compilation further suggests that $5p^5(^2P_{3/2})6p$ levels start ~100 cm^{-1} above the transition to $5p^5(^2P_{1/2})6s$ (Table 1[91] and Figure 7[92]). Based on the excited state energies of xenon, the lowest energy 2PA allowed transition ($^1S_0 \rightarrow 5p^5(^2P_{3/2})6p$) is expected to be centered ~0.12-0.25 eV above the upper CTTS transition in 1PA originating from the $^1S_0 \rightarrow 5p^5(^2P_{1/2})6s$ excitation. This is consistent with the measured 2PA spectra (Figure 7c), which peaks ~0.14 eV higher in energy, as compared to the upper component of the 1PA spectra.[41]

It is worth pointing out that the literature 1PA spectrum of aqueous potassium iodide used for this comparison is measured at high pressure (250 bar). Lowering the pressure from 250 bar to 1 bar has only a small effect on the iodide 1PA transition energies (~20 meV redshift),[94] and the peak positions for the CTTS transitions are the same for aqueous sodium and potassium iodide salts.[95] The 2PA bandwidth also appears to be different from that of the two 1PA transitions, implying different excited state character. Combined evidence thus suggests that the lowest energy band in the 2PA spectrum of aqueous iodide is due to the $^1S_0 \rightarrow 5p^5(^2P_{3/2})6p$ transition and is unrelated to either peak observed in the 1PA spectrum. Our assignments of the 1PA and 2PA transitions in aqueous iodide is consistent with the calculated cross-sections for multiphoton ionization of isoelectronic xenon atom in the *jl*-coupling limit.[96]

In broadband DUV-ESFG spectra, under the two-photon resonant one-photon off-resonant condition (Figure 6b, ω_1 = 295 nm, blue), the intensity is proportional to the product of the 1PA and 2PA absorption cross-sections at the sum frequency.[31,83] It has been established above that for bulk iodide, both $^1S_0 \rightarrow 5p^5(^2P_{1/2})6s$ and $^1S_0 \rightarrow 5p^5(^2P_{3/2})6s$ transitions are 1PA allowed and 2PA forbidden, and $^1S_0 \rightarrow 5p^5(^2P_{3/2})6p$ is only 2PA allowed, *i.e.*, no electronic transition is simultaneously 1PA and 2PA active. Thus, no ESFG intensity should be observed for iodide unless the symmetry is perturbed at the interface.

In bulk solution at room temperature, there is instantaneous asymmetry in the local solvation environment,[73] but upon moving to the interface, iodide is expected to lose ~1-2 water molecules from its first solvation shell and thus experiences far greater asymmetry.[8,75,97,98] In addition, at the high salt concentrations used in the ESFG spectroscopy experiments ($[NaI]_{bulk}$ = 5 M), solvent-shared and contact ion-pairs, solvent orientational effects, and electric double-layer formation are expected.[53,56,57] The external electric field experienced by the iodide ion at the interface strongly perturbs the symmetry and relaxes the 1PA and 2PA parity selection rules established for bulk aqueous iodide. When strictly resonant at only the sum frequency, ESFG intensity is observed at the interface only for the upper energy band (Figure 6b, blue). Here, the

external electric field effects at the air/water interface are predicted to be more strongly affecting the upper excited states with *p*-like symmetry than the lower *s*-like excited states, allowing sufficient mixing of the 1PA and 2PA allowed transitions in the higher energy band, and resulting in an ESFG-allowed transition. In addition, solute-solvent vibronic coupling may also enhance mixing between excited states that are energetically near-degenerate. A molecular dynamics simulation of the water molecules in the first solvation shell of the iodide ion predicts fast relaxation dynamics (~100 fs) corresponding to the intermolecular vibrations of the ion-water hydrogen bonds.[99] Such vibronic interactions occur within the timescale of our ultrafast laser pulse durations and potentially contribute to the perturbation of the symmetry of the excited states.

Conclusions

We, to the best of our knowledge, are the first to report the broadband 2PA spectra of aqueous iodide and to combine ESFG with 2PA spectroscopy, where the bulk-sensitive 2PA spectra provide crucial information that aids in the interpretation of the surface-sensitive ESFG spectra. By analyzing the subtle difference in band positions in the 1PA and 2PA spectra, and considering the selection rules for these two complementary spectroscopic techniques, we show that both the $^1S_0 \rightarrow 5p^5(^2P_{3/2})6s$ and $^1S_0 \rightarrow 5p^5(^2P_{1/2})6s$ transitions of bulk aqueous iodide which are allowed in 1PA, are 2PA inactive; the 2PA band is assigned to the $^1S_0 \rightarrow 5p^5(^2P_{3/2})6p$ transition. It is quite unprecedented that the electronic spectra measured in a highly condensed environment can be accurately explained using the atomic selection rule for an isolated molecule, signifying that the symmetry of the lower lying excited orbitals of *s* and *p* character are not perturbed to a great extent in the bulk liquid phase. The observed signal in the DUV-ESFG spectra must originate from symmetry breaking and solute-solvent vibronic coupling effects at the air/water interface. Further experiments and associated theoretical modeling will be necessary to extract additional details regarding these complex transitions observed in 1PA, 2PA, and ESFG spectra.

Chapter 4 Revisiting the π→π* Transition of the Nitrite Ion at the Air/Water Interface: A Combined Experimental and Theoretical Study

Adapted with permission from Mizuno, H.[#]; Oosterbaan, K. J.[#]; Menzl, G.[#]; Smith, J.; Rizzuto, A. M.; Geissler, P. L.; Head-Gordon, M.; and Saykally, R. J. "Revisiting the π→π* Transition of the Nitrite Ion at the Air/Water Interface: A Combined Experimental and Theoretical Study." *Chem. Phys. Lett.* **2020,** *751*, 137516.[100]

[#]These authors contributed equally. Molecular dynamics simulations were performed by the Geissler Group and electronic structure calculations were performed by the M. Head-Gordon Group at UC Berkeley.

Introduction

To further advance our fundamental understanding of the mechanism of selective ion adsorption at the air/water interface, measuring and interpreting detailed electronic spectra of interfacial ions presents a compelling prospect. Toward that end, our group has recently developed femtosecond broadband DUV-ESFG spectroscopy[27,32] that produces a broad, continuous, interfacial electronic $|\chi^{(2)}|^2$-spectrum in a single measurement. Compared to time-consuming, error-prone *pointwise* measurements made with resonant DUV-ESHG spectroscopy[7,8,28] that yield incomplete spectra, *broadband* DUV-ESFG spectroscopy allows a more quantitative analysis of interfacial electronic $|\chi^{(2)}|^2$-spectra. Herein, we employ broadband DUV-ESFG spectroscopy, MD simulations, and SOS-CIS(D_0) calculations to re-examine the $\pi\rightarrow\pi^*$ transition of the nitrite anion (NO_2^-) at the air/water interface and compare the results with those from our previous DUV-ESHG spectroscopy study.[101]

Since nitrite is a major component of marine and terrestrial nitrogen cycles, nitrite photochemistry both directly and indirectly affects the global carbon cycle, marine habitats, and atmosphere, thus making this system of central interest and importance. In the atmosphere, for example, photolysis of nitrite in seawater can form highly reactive hydroxyl (·OH) and nitric oxide (·NO) radicals, which can further react with volatile compounds.[102–104] Nitrite is a relatively kosmotropic anion in the Hofmeister series:[42]

$$F^- > Cl^- > NO_2^- > NO_3^- > Br^- > I^- > SCN^-$$

As a weak kosmotrope, nitrite is not expected to exhibit strong surface concentration enhancement at the air/water interface. In 2009, Brown et al. used X-ray photoemission spectroscopy on a liquid jet to measure the depth profile of nitrite and nitrate at the air/water interface and found both to be depleted relative to bulk concentrations; however, nitrite and nitrate were still *present* in the interfacial region (outermost ~2.5-3.0 nm, determined by photoelectron kinetic energy).[23]

The bulk UV-Vis spectrum of aqueous nitrite (Figure 8) exhibits an intense absorption band ($\varepsilon \approx 5800$ L mol^{-1} cm^{-1}) centered at 210 nm (5.90 eV) assigned to a $\pi\rightarrow\pi^*$ molecular transition.[105–107] Previous studies of the bulk spectrum have suggested that this band may engender transfer of an electron to the surrounding solvent, *i.e.*, is a charge-transfer-to-solvent (CTTS)

band.[108,109] However, the observation of this band in crystalline sodium nitrite and the absence of CTTS-like solvent dependence in other solvents provide evidence against this CTTS assignment.[105–107]

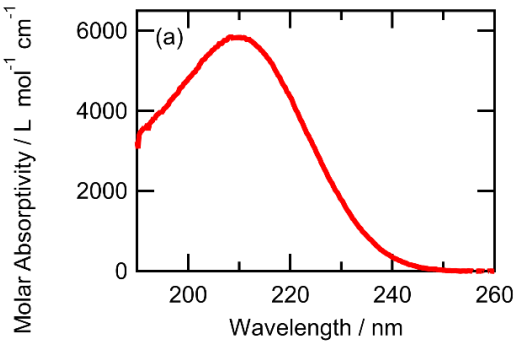

Figure 8. Bulk UV-Vis absorption spectrum of aqueous sodium nitrite ([$NaNO_2$] = 180 µM). The peak centered at 210 nm is assigned to an intramolecular $\pi \rightarrow \pi^*$ transition. Spectrum was measured at 293 K and 1 atm.

In 2012, Otten et al. reported pointwise DUV-ESHG spectra of sodium nitrite at the air/water interface and used a *bimolecular* Langmuir adsorption model to extract a surprisingly large and favorable Gibbs free energy of adsorption (ΔG_{ads} = −17.8 kJ mol^{-1}), suggesting adsorption as a Na^+-NO_2^- contact ion pair.[101] The ESHG spectra measured at three wavelengths (λ_{SHG} = 200 nm, 247 nm, and 255 nm) showed strong resonance enhancement only at 247 nm, which led Otten and co-workers to report a significant redshift (~0.75 eV) of the interfacial $\pi \rightarrow \pi^*$ transition relative to bulk that was attributed to contact ion pair formation and solvent effects.[101]

In the interest of re-examining the nitrite $\pi \rightarrow \pi^*$ transition at the air/water interface, the $|\chi^{(2)}|^2$-spectrum of nitrite was measured with broadband DUV-ESFG spectroscopy between ~230-260 nm, but no significant resonance enhancement was observed.[110] The vibrational SFG spectrum of the nitrite solution showed sharp features at 2870 cm^{-1} and 2933 cm^{-1}, corresponding to the $-CH_3$ symmetric stretch and its Fermi resonance, indicating the presence of hydrocarbons at the solution surface.[110] In solution, hydrocarbon impurities partition to the air/water interface and can contribute large non-resonant and/or resonant signals in SHG and SFG spectra.[111] The strong resonance enhancement observed exclusively at 247 nm in ESHG spectra by Otten et al.[101] may have resulted from aromatic structures and/or conjugated π-bond systems of hydrocarbon contaminants at the surface. Herein, we report broadband DUV-ESFG spectrum of interfacial nitrite in the ~200-220 nm region.

Materials and Methods

Ultrahigh purity sodium nitrite salt (99.999% trace metals basis, Aldrich), baked overnight, was used to reduce effects of hydrocarbon and other contamination.

All glassware was soaked in NOCHROMIX (Godax Laboratories, Inc.) and concentrated sulfuric acid solution overnight and washed with copious amounts of ultrapure water (18.2 MΩ.cm at 25 °C, TOC < 5 ppb, Milli-Q, EMD Millipore). Solutions were prepared with ultrapure water immediately before measurements.

The broadband DUV-ESFG spectroscopy setup has been described in detail in Chapter 1. Briefly, a 100-fs UV pulse (ω_1 = 266 nm) and a white light continuum pulse ($\omega_2 \approx$ 600-1400 nm) are temporally and spatially overlapped at the solution surface in reflection geometry, generating coherent sum frequency radiation ($\omega_{SF} = \omega_1 + \omega_2$) at the phase-matched angle.[27,32] The continuum pulse is generated by focusing the 800 nm output of a Ti-Sapphire amplifier into a quartz cuvette containing a continuous flow of water. This process gives rise to a positive temporal chirp of the broadband pulse.[30] Here, the longer wavelength portion ($\omega_2 \approx$ 800-1400 nm) of the broadband pulse is overlapped with the narrowband UV pulse (ω_1).

Computational Methods

To examine the effects of contact ion pairing on the $\pi \rightarrow \pi^*$ transition, MD simulations and electronic structure calculations were performed. Computing the $\pi \rightarrow \pi^*$ transition energy of nitrite in a contact ion pair configuration with a sodium cation from electronic structure calculations requires equilibrium configurations of the non-electronic degrees of freedom, *i.e.*, the atomic nuclei, as a starting point. Using empirical interaction potentials, such configurations from MD simulations of an ion pair in dilute bulk solution were harvested.

Ions were modeled as Lennard-Jones particles with a point charge at their center and the geometry of the nitrite ion was realized *via* harmonic potentials acting on the N−O distances and the O−N−O angle (ion parameters were taken from Refs.[112,113]). Simulations were performed using the rigid, non-polarizable SPC/E water model.[114] The effects of electronic polarization were taken into account in a mean-field approximation by applying an electronic continuum correction.[115] In practice, this entails rescaling the ionic (partial) charges by the square root of the high-frequency dielectric constant of water, $q_{eff} = q/\varepsilon_{el}^{1/2}$, where ε_{el} = 1.78. Consequently, the dielectric constant of the solvent is enhanced by a factor of ε_{el}, to about 130.[116,117] Taking the electronic polarizability into account in this manner provides consistency between the ions' charges and the parametrization of the employed water models.

To assess the influence of the employed water model on the obtained configurations, additional simulations with the rigid, non-polarizable TIP4P water model as the solvent were conducted.[118] Because the dielectric constant of TIP4P is significantly lower than that of SPC/E (about 90 for TIP4P after applying the electronic continuum correction), these calculations help illuminate its influence on the effective ion-ion interaction (Figure 9). Our results show that contact ion pairs are free-energetically more favorable in TIP4P than in SPC/E solvent, as expected from TIP4P's lower dielectric constant. This is also reflected in the respective dissociation equilibrium constants, which are K_{eq} = 0.62 mol L^{-1} for SPC/E and K_{eq} = 0.42 mol L^{-1} for TIP4P, where the location of the first maximum in $w(r)$ was chosen as the boundary of the associated state.[119] Nevertheless, the location and shape of the minimum in $w(r)$ is almost identical between the two models; in conjunction with the similar radial distribution functions between ions and water, this suggests that the local structures of contact pairs is not strongly affected by the choice of water model in our simulations.

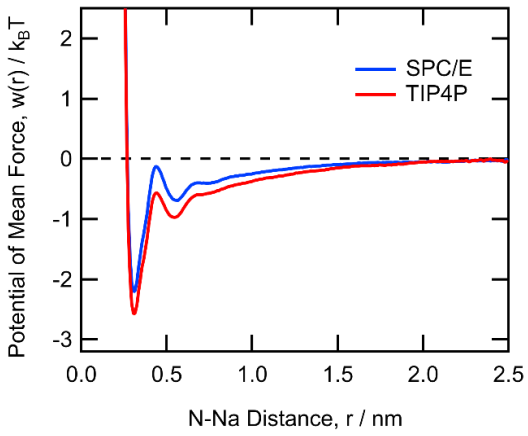

Figure 9. The potential of mean force, $w(r)$, as a function of N–Na distance for SPC/E and TIP4P, respectively. The increased likelihood of encountering ion pairs in TIP4P water due to its lower dielectric constant is reflected in the deeper minimum when compared to SPC/E. For distances beyond ca. 1 nm, the smooth decay of $w(r)$ is dominated by the dielectric constant of the respective water models.

Simulations were performed for a Na^+-NO_2^- ion pair solvated at the equilibrium density of SPC/E in a 5×5×5 nm^3 cubic box under periodic boundary conditions.[116] Configurations were propagated with a time step of 2 fs and water molecules were kept rigid using LINCS.[120] Constant temperature of 300 K was ensured by use of the stochastic v-rescaling thermostat,[121] and long-range interactions were treated using a particle mesh Ewald technique.[122] Simulations were performed using GROMACS 2019[123] and sufficient sampling of contact pair configurations was facilitated *via* umbrella sampling along the N–Na distance using PLUMED 2.5.[124]

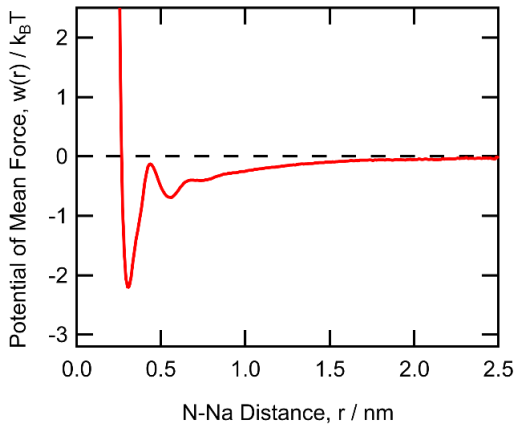

Figure 10. At low concentrations, the potential of mean force, $w(r)$, as a function of N–Na distance exhibits a minimum at ~0.3 nm that indicates the formation of contact ion pairs.

In order to identify contact ion pairs, the potential of mean force as a function of the N–Na distance r, $w(r) = -k_B T \ln[P(r)/(4\pi r^2)]$, where k_B is Boltzmann's constant and $P(r)$ is the equilibrium probability distribution of the distance r between ions was computed (Figure 10). The potential of mean force encodes the effective Na^+-NO_2^- interaction as a function of distance when the ions' relative orientations and the solvent degrees of freedom are canonically averaged over all

configurations.[119] The minimum in $w(r)$ at $r \approx 0.3$ nm corresponds to contact ion pair configurations; based on these data, configurations within $0.5k_BT$ of the minimum were selected as inputs for the electronic structure calculations. To limit the computational cost of those calculations, only the water molecules in the first solvation shell of the ions, determined from the respective radial distribution functions, were taken into account.

SOS-CIS(D_0) calculations[125,126] were performed for the Na^+-NO_2^- contact ion pair and the isolated NO_2^- ion in vacuum and surrounded by its first solvent shell. This is the most extreme example of the potential effect of solvation and any difference here should be greater than what would be observed experimentally. SOS-CIS(D_0) was chosen because it has N^4 scaling and it was well-validated for nitrite against EOM-CCSD,[127,128] which is accurate for single-electron valence excited states within 0.25 eV, while TDDFT[129–133] with various functionals was not. Calculations were performed in the Def2-SVPD basis set.[134,135]

Results and Discussion

The interfacial electronic $|\chi^{(2)}|^2$-spectrum (Figure 11c, red) measured with broadband DUV-ESFG spectroscopy appears strikingly similar to the bulk absorption spectrum (Figure 8). Thus, we confirm the presence of nitrite at the air/water interface (outermost ~1 nm); however, we do not observe the previously reported drastic redshift in the interfacial $\pi \rightarrow \pi^*$ transition, attributed to contact ion pairs and solvent effects.[101]

In XAS of aqueous sodium nitrite measured previously by our group, no appreciable ion pairing was observed in bulk solution.[136] However, the lower dielectric constant at the air/water interface[137,138] will increase the propensity for ion pair formation. Simulations by Venkateshwaran et al. have shown that ion pairing near the interface can be enthalpically and entropically favorable for oppositely charged ions, as it releases some hydrating waters to the bulk and reduces pinning of capillary waves.[53] At the concentrations used for the surface spectroscopy measurements discussed here, solvent separated, solvent shared, and contact ion pairs are likely to be present in the interfacial region. In addition, an electric double layer can form in the interfacial region at moderate-to-high salt concentrations,[56] which can induce ordering of water molecules and further alter the solvation environments at the interface. This induced ordering of water can increase the sampled "interfacial region" and thus may increase the probe depth of second order nonlinear spectroscopy techniques (*e.g.*, SHS, SFG) at higher electrolyte concentrations.[139]

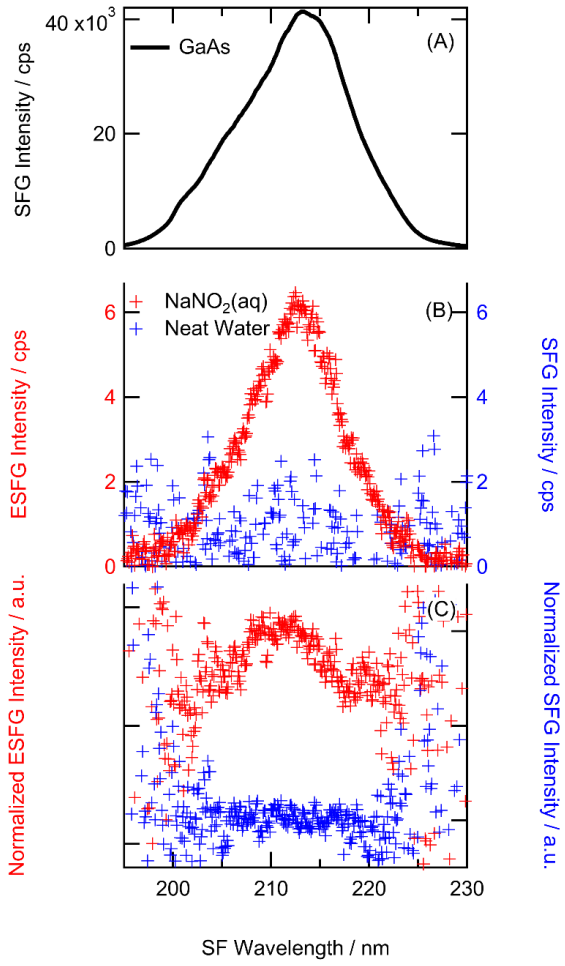

Figure 11. (a) Non-resonant SFG spectrum of gallium arsenide, (b) raw ESFG spectra of aqueous sodium nitrite and neat water, and (c) interfacial $|\chi^{(2)}|^2$-spectrum measured by broadband DUV-ESFG spectroscopy (red, $[NaNO_2]_{bulk}$ = 3.4 M) and neat water (blue). All spectra measured at 293 K.

Under the two-photon on-resonance, one-photon off-resonance condition employed here, the normalized ESFG intensity (I_{SFG}) can be expressed as

$$I_{SFG} \propto \left|\chi^{(2)}\right|^2 \propto \sum_n \frac{|\mu_{0n}(\alpha_{0n})_{2PA}|^2}{(\omega_n - \omega_{SFG})^2 + \Gamma_n^2}$$

where $\chi^{(2)}$ is the 2nd-order nonlinear susceptibility, μ_{0n} is the transition dipole matrix element and $(\alpha_{0n})_{2PA}$ is the two-photon absorption polarizability tensor element connecting the ground state to excited state n, Γ_n is the linewidth of the transition, ω_n is the transition energy between the ground state and excited state n, and ω_{SFG} is the sum frequency of the input photons.[31,62,83] By plotting I_{SFG} vs. ω_{SFG}, the interfacial electronic $|\chi^{(2)}|^2$-spectrum is obtained. We note that the obtained $|\chi^{(2)}|^2$-spectrum is a power spectrum and that a more rigorous approach would be required to measure $\mathrm{Im}(\chi^{(2)})$ by heterodyne-detected or phase-sensitive ESFG spectroscopy; here, the non-resonant

contribution from the solvent (water) is assumed to be negligibly weak because no SFG signal is observed from the neat water surface (Figure 11b,c).

Theoretical Results and Discussion

In vacuum, the $\pi \rightarrow \pi^*$ transition of isolated nitrite occurred at 5.71 eV. The $\pi \rightarrow \pi^*$ transition of Na^+-NO_2^- contact pair showed some character at 5.37 eV and 5.80 eV in vacuum. However, when just two water molecules were added to a plane parallel with the contact ion pair, the energy of the transition stabilized to 5.69 eV, which we believe is closer to an accurate representation of the interface.

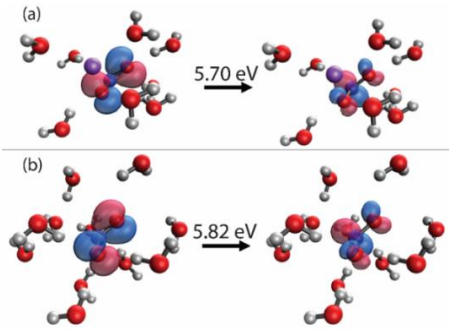

Figure 12. Representative snapshots and calculated $\pi \rightarrow \pi^*$ transition energies of (a) Na^+-NO_2^- contact ion pair in a solvent shell and (b) isolated NO_2^- ion in a solvent shell.

In order to get reproducible results, the geometry of NO_2^- in the solvent shell snapshots was slightly modified to be consistent with the vacuum geometry and five randomly selected snapshots for the Na^+-NO_2^- contact pair and six for NO_2^- were calculated. While all NO_2^- snapshots had one distinct transition energy at which the $\pi \rightarrow \pi^*$ transition was found, the contact pair sometimes contained multiple transition energies with $\pi \rightarrow \pi^*$ character. The average energy was determined by averaging all states for which $\pi \rightarrow \pi^*$ character was observed. The $\pi \rightarrow \pi^*$ transition for the solvated Na^+-NO_2^- contact pair was found to be on average 5.70 eV (Figure 12a), and the $\pi \rightarrow \pi^*$ transition for solvated NO_2^- to be at 5.82 eV (Figure 12b). The differences between these values (0.12 eV), as well as the contrast between in vacuum and in solvation shell, are substantially smaller than the value reported by Otten et al., which was ~0.75 eV.[101]

Conclusions

We have employed broadband DUV-ESFG spectroscopy, MD simulations, and SOS-CIS(D_0) electronic structure calculations to re-examine the $\pi \rightarrow \pi^*$ transition of nitrite at the air/water interface. Our results, which reveal no significant shift in the $\pi \rightarrow \pi^*$ transition for the contact ion pair, revise our previously reported conclusions from pointwise DUV-ESHG spectra[101] that suggested a large redshift at the surface and a bimolecular adsorption mechanism *via* contact ion pair formation. Although no evidence of a contact ion pair induced redshift and strongly favorable bimolecular adsorption mechanism were found herein, our results do not rule out the presence of a distribution of local solvation environments at the interface, including solvent separated, solvent shared, contact ion pairs, and small ion clusters, under the experimental conditions discussed here.

Chapter 5 Electronic Spectra of Aqueous Phenol

Unpublished material in this chapter is included with permission from Shivalee Dey, Katherine J. Oosterbaan, Nathan Odendahl, Shane W. Devlin, Dirk R. Rehn, Andreas Dreuw, Phillip L. Geissler, Martin Head-Gordon, Stephen E. Bradforth, and Richard J. Saykally.

Two-photon absorption spectra were measured by the Bradforth Group at University of Southern California, molecular dynamics simulations were performed by the Geissler Group at UC Berkeley, and electronic structure calculations were performed by the M. Head-Gordon Group at UC Berkeley and the Dreuw Group at Heidelberg University.

Introduction

Understanding the behavior of ions and molecules at aqueous interfaces is key to central processes in electrochemistry, atmospheric chemistry, and biochemistry, and is assuming an increased level of attention.[1,3,6] Recent experimental advances have facilitated the measurement of broadband electronic spectra of ions at the air/water interface by broadband deep ultraviolet electronic sum frequency generation (DUV-ESFG) spectroscopy.[27,32,62,100] Here, we apply this new technique for the study of a prototypical organic molecule, phenol (C_6H_5OH), at the air/water interface.

Phenol is an amphiphilic organic molecule with a hydrophilic hydroxyl group and a hydrophobic phenyl ring. The phenol motif is present in many biochemical systems, most prominently in the amino acid tyrosine, which plays a central role in the water-splitting reaction in photosynthesis.[140] In the environment, phenol is a commonly occurring pollutant in industrial wastewater.[141] Phenol contributes to secondary organic aerosol formation *via* oxidation by triplet organic compounds in the atmosphere[142] and can affect reactions occurring on ocean surfaces.[143] "On-water" catalysis studies have reported orders of magnitude increases in reaction rates of certain organic reactions in droplets and thin films that have been attributed to partial solvation of reagents at the interface.[144] Recent work by Tahara et al. showed that photoionization of phenol occurs ca. 10^4 times faster at the air/water interface than in bulk, reflecting the different solvation environment at the interface.[145] Hence, studying the behavior of organic molecules at aqueous interfaces is of central current interest.

The bulk UV-Vis absorption spectrum of aqueous phenol exhibits two main bands near 4.6 eV (270 nm) and 5.9 eV (210 nm) that correspond to transitions from the electronic ground state to the lowest two $^1\pi\pi^*$ excited states. Additionally, there is a $^1\pi\sigma^*$ state that lies between the two $^1\pi\pi^*$ states. The $S_2(1^1\pi\sigma^*)$ potential energy surface (PES) of phenol is dissociative with respect to the O−H bond stretching coordinate and crosses the bound PESs of the electronic ground state (S_0) and first excited state $S_1(1^1\pi\pi^*)$ to produce two conical intersections (CIs).[146,147] Previous pump-probe studies in the gas phase[148,149] and in cyclohexane[150,151] have reported phenoxy radical and hydrogen atom products on a femtosecond timescale upon directly populating the dissociative $S_2(1^1\pi\sigma^*)$ state by photoexcitation above the $1^1\pi\pi^*/1^1\pi\sigma^*$ CI. In aqueous solution, Oliver et al.[152] reported phenoxy radical and solvated electron formation, but with orders of magnitude difference in timescales for photoexcitation of the higher energy $2^1\pi\pi^*$ state (~200 fs timescale) compared to below the $1^1\pi\pi^*/1^1\pi\sigma^*$ CI (~2 ns time scale), and they proposed a near-threshold autoionization mechanism. Upon photoexcitation above the $1^1\pi\pi^*/1^1\pi\sigma^*$ CI, Riley et al.[149] observed a proton-

coupled electron transfer mechanism leading to solvated electron formation. In a recent cluster study, Sandler et al.[153] proposed a sequential proton-coupled electron transfer mechanism where the solvent reorganization stabilizes the charge-transfer state in addition to O−H bond elongation.

At the air/water interface, monolayer formation with no concentration dependence on the molecular orientation has been reported for bulk concentrations below 200 mM.[154–156] Electronic second harmonic generation (ESHG) spectroscopy experiments have reported a highly favorable adsorption free energy to the air/water interface ($\Delta G° = -14.7 \pm 0.4$ kJ mol^{-1})[157] with a favorable orientation, tilted 50 ± 5° relative to the surface normal.[156] Herein, we present the surface-specific electronic $|\chi^{(2)}|^2$-spectrum of phenol at the air/water interface in the deep UV (ca. 5.4-6.2 eV), preliminary two-photon absorption (2PA) spectral data, and employ MD simulations and electronic structure calculations to elucidate the effects of aqueous solvation in the bulk and at the interface.

Materials & Methods

Phenol (99%, ACROS Organics) was used without further purification. All solutions were prepared in glassware washed and soaked in NOCHROMIX (Godax Laboratories, Inc.) and concentrated sulfuric acid solution overnight, then rinsed with copious amounts of ultrapure water (18.2 MΩ.cm at 25 °C, TOC < 5 ppb, Milli-Q, EMD Millipore). Sample solutions were prepared immediately before measurements.

The bulk linear one-photon absorption spectrum was measured in a spectrophotometer (UV-2600, SHIMADZU) in a 10-mm pathlength quartz cuvette at a bulk concentration of 100 μM.

The broadband DUV-ESFG spectrum of phenol at the air/water interface was measured with *ssp*-polarization (*s*-polarized SFG, *s*-polarized 285 nm, and *p*-polarized white light continuum) using the experimental setup described in Chapter 1. The bulk concentration (100 mM) used corresponds to a surface concentration of ca. 4.4 M.[156] Here, a commercial optical parametric amplifier (Spectra Physics, TOPAS Prime) is used to generate the UV narrowband pulse at ω_1 = 285 nm (4.35 eV, 8 μJ/pulse, FWHM = 2 nm), which is then spatially and temporally overlapped with a spectrally broad white light continuum pulse (50 μJ/pulse, $\omega_2 \approx$ 600-1400 nm) at the solution surface. The generated coherent sum frequency radiation in reflection geometry at the phase-matched angle is spatially and spectrally filtered and then directed into a spectrograph and CCD detector. Samples were contained in a Teflon Petri dish and measured at 293 K. Each sample was exposed to the laser for a total of 20 minutes with no visible photodegradation, photoproducts, or changes in the signal.

Bulk 2PA spectra were measured by the Bradforth Group at University of Southern California by mixing 673 nm (1.84 eV) pump with the visible portion of the white light continuum (~300-600 nm) to cover the spectral range of the lowest energy excitations. Both pump and probe beams were overlapped spatially and temporally 1-mm flow cell. Differential absorbance (ΔA) of the broadband continuum probe was recorded with and without the pump pulse using a 256-channel silicon photodiode array. The detailed experimental design is described elsewhere.[78,80]

Computational Methods

To examine the effects of aqueous solvation on the electronic transitions of phenol, molecular dynamics simulations were performed by the Geissler Group and electronic structure calculations were performed by the M. Head-Gordon Group and the Dreuw Group. Computing the transition energies of phenol requires equilibrium configurations of the non-electronic degrees of freedom, *i.e.*, the atomic nuclei, as a starting point. Using empirical interaction potentials, such configurations from MD simulations were harvested.

A series of configurations were taken of one phenol molecule surrounded by 267 SPC/E[1] molecules. The LAMMPS molecular dynamics package[158] was used to simulate a likely molecular geometry of a phenol in either bulk liquid or near an air-water interface. The phenol was parameterized with the Amber ff99[159] force field and was kept rigid and planar (*i.e.*, CCOH dihedral angle = 0°, point group: C_s). SPC/E molecules were kept rigid using the SHAKE[160] algorithm, while the phenol was kept rigid using the LAMMPS rigid/nvt command.[161]

"Bulk-like" and "interface-like" configurations were both generated by using a spring relative to the center of mass to secure the phenol either to the center or to the edge of the water droplet. The atomic coordinates of the phenol and nearest water molecules were extracted for deeper electronic structure analysis.

In aqueous solution, there are three dominant phenol-water interactions: phenol can act as a hydrogen bond donor and/or hydrogen bond acceptor, and a weaker OH−φ interaction can occur between water and the π-electron cloud of the ring.[162] At the air/water interface, a highly specific hydration structure is predicted by Tahara and co-workers wherein one water molecule forms a weak OH−φ bond with the phenol π-ring and a second water molecule accepts a hydrogen bond from the phenol −OH group,[163] consistent with the partial hydration proposed by Girault and co-workers.[157] In order to harvest "bulk-like" and "interface-like" configurations for electronic structure calculations, snapshots where phenol was donating, accepting, or donating and accepting hydrogen bonds were selected from the simulation results. A water-phenol contact was classified as a hydrogen bond if the oxygen-oxygen distance was less than 3.5 Å and the angle made by the O−H bond vector with the oxygen-oxygen displacement vector was less than 30°.

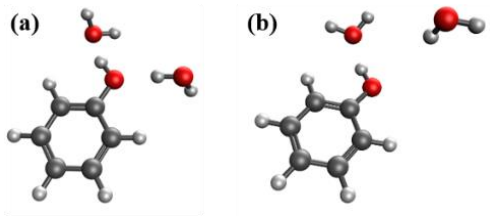

Figure 13. Representative snapshots of (a) bulk-like solvation and (b) interfacial solvation configurations used for ADCMAN electronic structure calculations.

To limit the computational cost of the electronic structure calculations, only two water molecules nearest to the phenol −OH group were taken into account. The OH−φ interaction was found to not significantly affect the transition energies and the water molecule interacting with the ring was not explicitly included in the electronic structure calculations to limit the computational cost of those calculations. Algebraic Diagrammatic Construction (ADC)[164–166] calculations were performed for an isolated phenol in the gas phase, bulk-like solvated, and interface-like solvated

phenol configurations to obtain 1PA oscillator strengths and 2PA cross-sections for degenerate excitation, 3.64 eV + broadband, and 4.35 eV + broadband energies to match experimental conditions. ADC was chosen because of its high accuracy where TDDFT calculations had failed, and because it is one of the few methods in Q-Chem currently capable of calculating the 2PA cross-sections. Calculations were performed in the Def2-TZVPD basis set.

Results & Discussion

In 1PA spectra, a band near 275 nm (4.5 eV) assigned to the $S_0 \rightarrow S_1(1^1\pi\pi^*)$ transition is observed in gas phase and bulk aqueous phenol. Interestingly, the bulk 2PA spectrum (Figure 14) measured by the Bradforth group shows relatively lower intensity in this region compared to the 1PA spectrum. The $S_0 \rightarrow S_1(^1\pi\pi^*)$ transition was not observed in in our interfacial broadband DUV-ESFG measurements (data not shown) due to signal interference from bulk fluorescence.

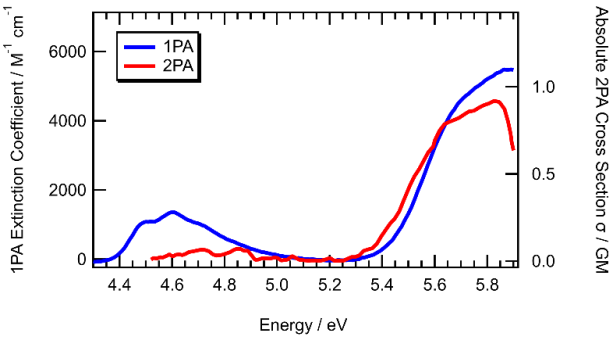

Figure 14. One-photon (blue) and two-photon (red) absorption spectra of bulk aqueous phenol measured by the Bradforth Group. Two-photon absorption was measured with 673 nm pump and continuum (~300-600 nm) pulses. [PhOH] = 851 mM.

In the case of the two-photon (*i.e.* sum frequency) on-resonance and one-photon off-resonance homodyne-detection condition employed here, the normalized ESFG signal intensity is proportional to $|\chi^{(2)}|^2$, where $\chi^{(2)}$ is the second-order nonlinear susceptibility:

$$I_{\mathrm{ESFG}} \propto \left|\chi^{(2)}\right|^2 \propto \sum_n \frac{|\mu_{0n}(\alpha_{0n})_{2\mathrm{PA}}|^2}{(\omega_n - \omega_{\mathrm{SFG}})^2 + \Gamma_n^2}$$

Here, μ_{0n} is the one-photon absorption (1PA) transition dipole matrix element and $(\alpha_{0n})_{2PA}$ is the two-photon absorption (2PA) polarizability tensor element connecting the ground state to excited state n, Γ_n is the linewidth of the transition, ω_n is the transition energy between the ground state and excited state, and ω_{SFG} is the sum frequency of the input photons.[31,83] The selection rules for interface specific ESFG spectroscopy under this condition require a transition to be simultaneously 1PA and 2PA active.[31,62,83] The low absorption of the $S_0 \rightarrow S_1(^1\pi\pi^*)$ transition in 2PA and broadband DUV-ESFG spectra suggests a weak 2PA cross-section for the lowest electronic excitation.

The absorption spectra at higher energies are shown in Figure 15. The fine structure observed in the gas phase[167] (Figure 15a) is lost in the bulk aqueous 1PA absorption spectrum (Figure 15b), due to inhomogeneous broadening, as solvent fluctuations create a continuum of possible local solvation environments.[168] A shoulder arising from higher energy transitions is

present; however, measuring 1PA at these higher energies in aqueous solution presents a challenge experimentally because the water electronic absorption onset begins near ~6.4 eV (194 nm). Further experiments are underway to measure 2PA spectra at these higher energies by mixing 340 nm (3.64 eV) and a continuum pulse.

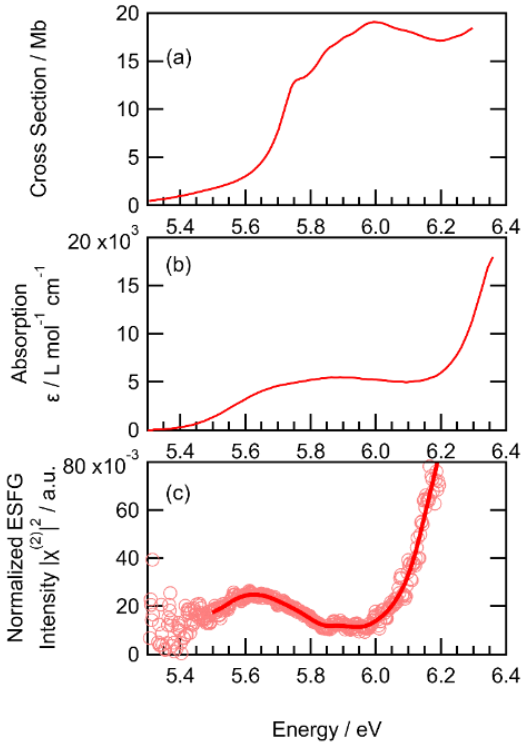

Figure 15. Electronic spectra of phenol. (a) Gas-phase absorption spectrum at room temperature reproduced from Ref.[167], (b) bulk one-photon absorption spectrum of aqueous phenol ($[PhOH]_{bulk}$=100 µM), and (c) interfacial $|\chi^{(2)}|^2$-spectrum measured with broadband DUV-ESFG spectroscopy ($[PhOH]_{bulk}$=100 mM). All spectra were measured at room temperature (293 K).

Compared to the gas phase[167] and bulk 1PA spectra, the interfacial $|\chi^{(2)}|^2$-spectrum (Figure 15c) measured with broadband DUV-ESFG spectroscopy appears to exhibit a redshift and a slight change in the spectral shape. The spectral differences likely arise from the differences in selection rules in the spectroscopy techniques and the solvation environments.

As presented above, ESFG intensity is proportional to the product of the 1PA and 2PA cross-sections. The 2PA spectra at higher energies (ca. 5.7-6.3 eV) have yet to be measured so we cannot definitively say whether the differences in the spectral shape in the 5.4-6.2 eV region are purely due to selection rules. However, we can elucidate the effects of solvation by comparing with MD simulations and electronic structure calculations. The highly specific hydration structure at the interface and differences in local solvation environment relative to bulk will lead to some shifts in the electronic spectra. In 4-methylphenol (*p*-cresol), Fornander et al. found that discrete hydrogen bonding motifs (viz. phenol as a hydrogen bond donor vs. acceptor, or both) can cause small spectral shifts (~2-4 nm, ~0.05-0.1 eV) in the $S_0 \rightarrow S_1(1^1\pi\pi^*)$ and $S_0 \rightarrow S_3(2^1\pi\pi^*)$ transitions.[169] Molecular orbitals from the ADC calculations of phenol in representative solvation environments are presented in Figure 16 and the transition energies and associated oscillator strengths and 2PA cross-sections are presented in Table 2 and Table 3.

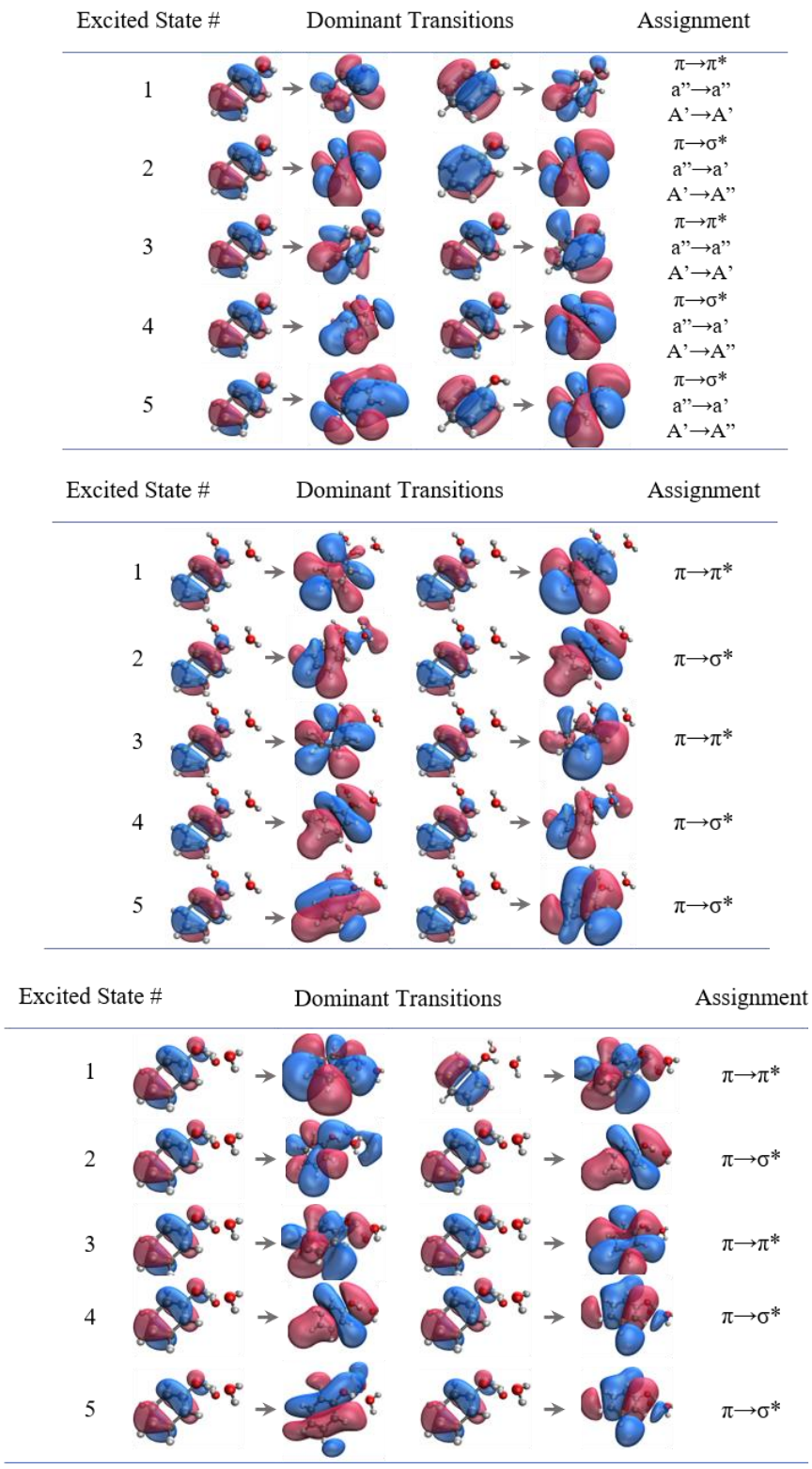

Figure 16. Molecular orbitals of dominant transitions and assignments for phenol in gas phase (top), bulk-like solvation (middle), and interface-like solvation (bottom) environments. The symmetry labels for the orbitals and excitations in the gas phase are in the C_s point group.

Table 2. Gas phase electronic transition energies and associated one-photon absorption oscillator strengths and two-photon absorption cross-sections for (a) degenerate 2PA excitation, (b) 3.64 eV + broadband excitation, and (c) 4.35 eV + broadband excitation.

(a)

Exc State #	Transition Energy (eV)	1PA Osc	2PA (par)	2PA (per)	pol. ratio	Assignment
1	4.9	0.0295	8.59	6.39	1.34	π→π* a"→a" A'→A'
2	5.8	0.0002	0.57	0.42	1.33	π→σ* a"→a' A'→A"
3	6.1	0.0970	110.78	38.05	2.91	π→π* a"→a" A'→A'
4	6.4	0.0032	36.91	27.68	1.33	π→σ* a"→a' A'→A"
5	6.8	0.0000	11.80	8.85	1.33	π→σ* a"→a' A'→A"

(b)

Exc State #	Transition Energy (eV)	1PA Osc	2PA (par)	2PA (per)	pol. ratio	Assignment
1	4.9	0.0295	12.08	9.53	1.27	π→π*
2	5.8	0.0002	0.75	0.85	0.88	π→σ*
3	6.1	0.0970	118.12	40.40	2.92	π→π*
4	6.4	0.0032	38.22	28.86	1.32	π→σ*
5	6.8	0.0000	11.90	8.93	1.33	π→σ*

(c)

Exc State #	Transition Energy (eV)	1PA Osc	2PA (par)	2PA (per)	pol. ratio	Assignment
1	4.9	0.0283	25.70	23.68	1.09	π→π*
2	5.8	0.0003	2.82	3.95	0.71	π→σ*
3	6.1	0.0983	151.64	50.15	3.02	π→π*
4	6.3	0.0029	48.74	38.41	1.27	π→σ*
5	6.8	0.0001	12.89	9.89	1.30	π→σ*

Table 3. Electronic transition energies and associated one-photon absorption oscillator strengths and two-photon absorption cross-sections for (a) bulk-like solvated 3.64 eV + broadband excitation, (b) bulk-like solvated 4.35 eV + broadband excitation, and (c) interface-like solvated 4.35 eV + broadband excitation.

(a)

Exc State #	Transition Energy (eV)	1PA Osc	2PA (par)	2PA (per)	pol. ratio	Assignment
1	4.9	0.0257	10.9	8.5	1.28	π→π*
2	5.9	0.0013	2.9	1.5	1.92	π→σ*
3	6.1	0.0977	118.6	38.6	3.07	π→π*
4	6.4	0.0039	42.4	31.9	1.33	π→σ*
5	6.8	0.0002	13.5	9.4	1.44	π→σ*

(b)

Exc State #	Transition Energy (eV)	1PA Osc	2PA (par)	2PA (per)	pol. ratio	Assignment
1	4.9	0.0257	22.5	20.1	1.12	π→π*
2	5.9	0.0013	5.9	5.9	0.99	π→σ*
3	6.1	0.0977	153.9	48.0	3.21	π→π*
4	6.4	0.0039	52.5	40.6	1.29	π→σ*
5	6.8	0.0002	21.5	14.7	1.46	π→σ*

(c)

Exc State #	Transition Energy (eV)	1PA Osc	2PA (par)	2PA (per)	pol. ratio	Assignment
1	4.8	0.0368	54.6	56.1	0.97	π→π*
2	5.4	0.0011	12.2	15.4	0.79	π→σ*
3	5.9	0.1367	256.7	78.1	3.29	π→π*
4	6.1	0.0035	69.2	46.6	1.49	π→σ*
5	6.2	0.0006	36.4	25.4	1.43	π→σ*

The ADC results predict redshifts in the excitation energies for phenol in the "interface-like" configuration wherein phenol acts as a hydrogen bond donor relative to bulk-like configurations wherein phenol is both hydrogen bond donor and acceptor. These results align with our measured broadband DUV-ESFG spectra that shows an apparent redshift in the $|\chi^{(2)}|^2$-spectrum and are also consistent with theoretical results of Fornander et al.[169]

Conclusions

The results of our broadband DUV-ESFG spectroscopy measurements of phenol at the air/water interface, combined with measured bulk 2PA spectra, suggest that the lowest electronic excitation ($1^1\pi\pi^*$) is not strongly 2PA active. At higher energies corresponding to $1^1\pi\sigma^*$and $2^1\pi\pi^*$ transitions, the highly specific hydration structure at the interface leads to an apparent redshift in the spectrum. Further work is necessary to elucidate the role of selection rules on the interfacial $|\chi^{(2)}|^2$-spectrum of phenol.

Chapter 6 Future Directions for Broadband DUV-ESFG Spectroscopy

Homodyne- and Heterodyne-detected ESFG Spectroscopy

As of Spring 2021, the optical design of the broadband DUV-ESFG spectroscopy setup in the Saykally Group employs a homodyne detection reflection geometry (Figure 17) based on the homodyne ESFG experiment of Yamaguchi & Tahara.[29]

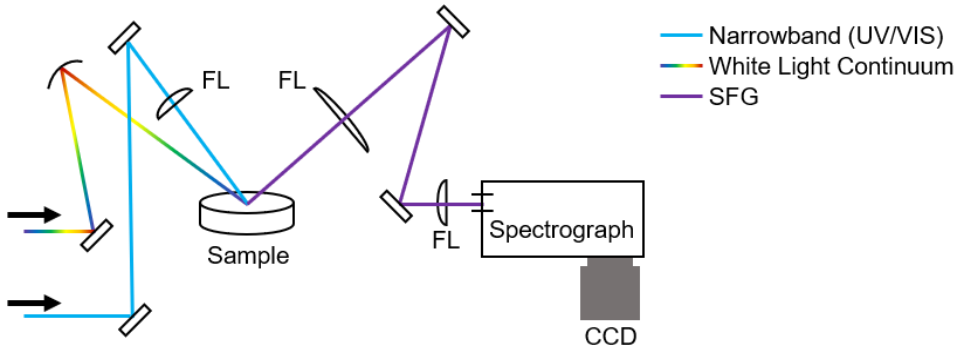

Figure 17. Simplified diagram of homodyne-detected broadband DUV-ESFG spectroscopy setup in the Saykally Group as of Spring 2021. Complete diagram of setup is presented in Chapter 1.

In homodyne-detected ESFG spectroscopy, the background-subtracted and normalized intensity is proportional to the square modulus of the second-order nonlinear susceptibility,

$$I_{\mathrm{ESFG}} \propto |E_{\mathrm{SFG}}|^2 \propto \left|\chi^{(2)}\right|^2 = N^2\left|\langle\beta^{(2)}\rangle\right|^2$$

where $\chi^{(2)}$ is the macroscopic nonlinear susceptibility and $\beta^{(2)}$ is the molecular hyperpolarizability. Thus, phase information from the complex $\chi^{(2)}$-spectrum is lost in the homodyne-detected $|\chi^{(2)}|^2$-spectrum—the "power spectrum". Because of this limitation, homodyne-detected SFG spectra has proven to be challenging to interpret, as was the case for homodyne-detected vibrational SFG power spectra of the water O–H stretch region,[170,171] and cannot provide absolute orientational information without serious assumptions at aqueous interfaces, which is important in understanding mechanistic details of interfacial systems.[49,50] In recent years, several research groups have successfully developed heterodyne-detected (or phase-sensitive) SFG spectroscopy methods in the infrared[170–174] and visible[175–177] wavelengths. Typically, a local oscillator and phase delay plate are introduced in the beam paths to obtain interference between the local oscillator field and the signal field. The intensity of heterodyne-detected ESFG spectra can be expressed as:

$$I_{\mathrm{HDESFG}} \propto |E_{\mathrm{SFG}} + E_{\mathrm{LO}}|^2 = |E_{\mathrm{SFG}}|^2 + |E_{\mathrm{LO}}|^2 + 2|E_{\mathrm{SFG}}||E_{\mathrm{LO}}|\cos\Delta\phi$$

where E_{SFG} is the signal field, E_{LO} is the local oscillator field, and $\Delta\phi$ is the phase difference between the two fields. The complex $\chi^{(2)}$ can be extracted by isolating the cross-term using a Fourier transform to obtain the spectrum in the time domain, with the time delay set by the delay plate. The homodyne contributions to the signal occur at $t = 0$ and the heterodyne contributions exist at $t = \pm\Delta t$, where Δt is determined by the thickness and material of the delay plate. The cross-term can be extracted using a step function filter, then an inverse Fourier transform is performed

to return to the frequency domain. After normalization, the intensity is proportional to $\chi^{(2)}$ wherein the imaginary components, Im($\chi^{(2)}$), are absorptive at resonances and the real components, Re($\chi^{(2)}$), are dispersive at resonances. Additionally, orientational information can be extracted from the signs:

$$I \propto |E_{\mathrm{SFG}}||E_{\mathrm{LO}}| \cos \Delta\phi \propto \chi^{(2)} \propto N\langle\beta^{(2)}\rangle$$

Because ESFG signals are inherently weak due to being generated from only a few monolayers at the interface, relatively long acquisition times are necessary to obtain sufficient signal-to-noise ratios. The cross-term that oscillates at the phase difference between the two fields can be strongly amplified and thus reduce acquisition times and significantly improve signal-to-noise ratio, which would allow for measurement of interfacial spectra at low concentrations and/or with analytes that possess only weakly resonant signals.

In 2008, the Tahara Group demonstrated heterodyne-detected ESFG spectroscopy wherein the local oscillator was placed in non-collinear reflection geometry after the sample to measure the interfacial spectra and absolute surface orientation of *p*-nitroaniline and coumarin dye molecules.[175,178] More recently, the Roberts Group generated the local oscillator in non-collinear transmission geometry before the sample through a thin z-cut quartz crystal to probe a thin organic semiconductor material.[177] Both the Tahara and Roberts Groups mixed a broadband continuum pulse (~540-1200 nm, ~450-800 nm) and a narrowband up-conversion pulse centered near 800 nm to generate broadband sum frequency near 410 nm and 340 nm, respectively. To the best of our knowledge, heterodyne-detected ESFG spectroscopy in the deep ultraviolet (~200 nm) has not yet been successfully demonstrated.

To incorporate heterodyne-detection in our broadband DUV-ESFG setup, several efforts were made. The initial attempt was modeled following the Tahara Group, viz. a non-collinear reflection geometry, wherein the local oscillator was placed after the sample (Figure 18). Here, the signal field is generated at the sample and only the sum frequency field was transmitted through the delay plate (CaF_2 window) to generate the phase difference. The fundamental and sum frequency fields were then re-focused onto the local oscillator. This design suffered from significant alignment challenges after the sample, as it required re-establishing spatial and temporal overlap of three beams using a single spherical concave mirror. Furthermore, the reflectance of optics drops precipitously in the ultraviolet.

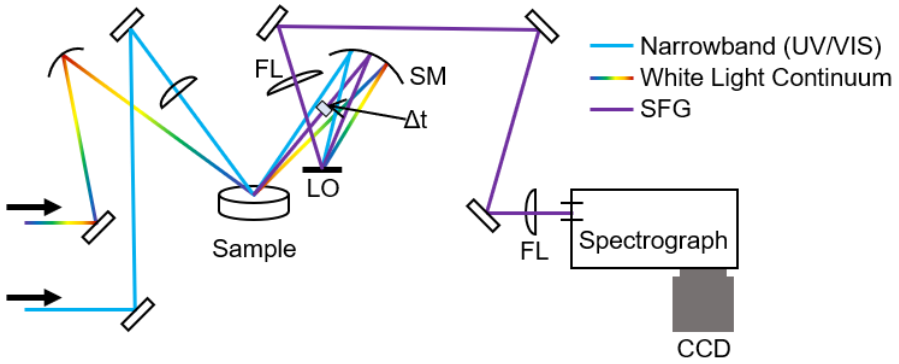

Figure 18. Heterodyne-detected broadband SFG design following Tahara et al. (FL: focusing lens, SM: spherical mirror, Δt: delay plate, LO: local oscillator, CCD: charge-coupled device camera)

To simplify the alignment, two off-axis parabolic mirrors were installed to replace the single spherical mirror (Figure 19). This simplified the alignment procedure for the three beams, but the increased number of reflections severely attenuated the intensity when working with UV wavelengths.

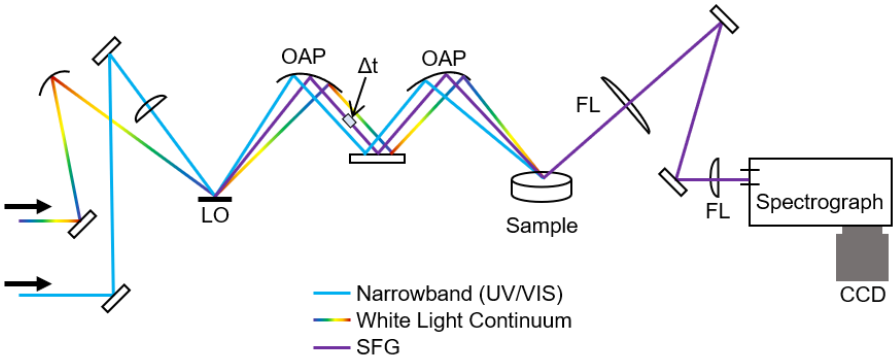

Figure 19. Adapted HD-ESFG spectroscopy design with off-axis parabolic mirrors. (FL: focusing lens, Δt: delay plate, LO: local oscillator, OAP: off-axis parabolic mirror, CCD: charge-coupled device camera)

To limit attenuation of the local oscillator signal in reflection geometry, a transmission geometry, placing the local oscillator before the sample, was incorporated. A z-cut quartz crystal (20 μm thickness, Crystran Ltd.) was used as the local oscillator in transmission geometry (Figure 20).

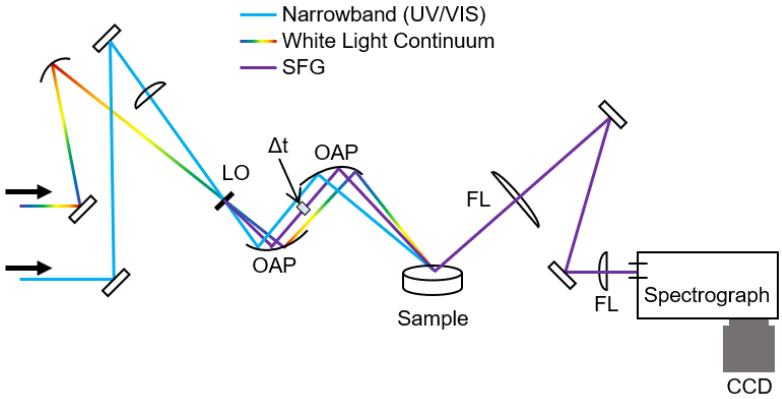

Figure 20. HD-ESFG spectroscopy design with local oscillator in transmission geometry. (FL: focusing lens, Δt: delay plate, LO: local oscillator, OAP: off-axis parabolic mirror, CCD: charge-coupled device camera)

To confirm the alignment, homodyne- and heterodyne-detected ESFG spectra of GaAs were measured (Figure 21), mixing the white light continuum pulse (~600-1400 nm) and 800 nm narrowband pulse using the setup as shown in Figure 20. The homodyne ESFG spectrum (Figure 21a) was measured without the local oscillator and delay plates in the beam paths. For the heterodyne-detected ESFG spectrum (Figure 21b), the delay plate acts to insert a temporal delay in the local oscillator, which results in spectral fringes, with the spacing corresponding to the phase difference between the local oscillator and sample signal fields. The fringes can be further enhanced by optimizing the alignment.

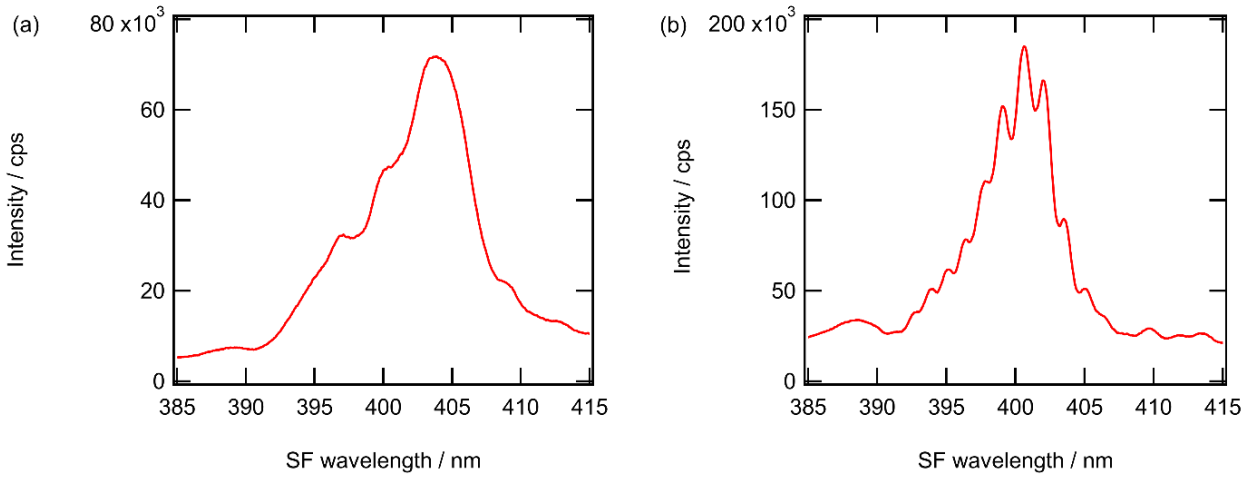

Figure 21. (a) Homodyne-detected ESFG spectrum of GaAs measured with the local oscillator and delay plate removed from the beam paths and (b) heterodyne-detected ESFG spectrum of GaAs measured with the local oscillator and delay plate in the beam path.

Using the design as described above, the frequency-doubled 400 nm was used as the narrowband up-conversion frequency and mixed with the white light continuum pulse, resulting in an SFG spectrum centered near 267 nm. When the SFG spectrum generated through the local oscillator (z-cut quartz) was measured, there were certain frequencies where the amplitude of the local oscillator signal was significantly decreased, viz. near 257 nm and 271 nm, as shown below (Figure 22).

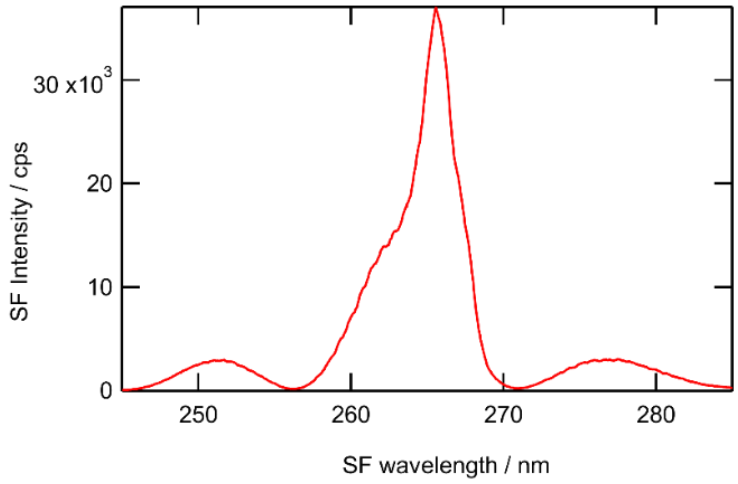

Figure 22. Non-resonant SFG spectrum of z-cut quartz (local oscillator) measured in transmission geometry.

The constructive and destructive interference in the spectrum is attributed to the temporal walk-off due to different group velocities of the input and sum frequencies as they travel through the 20 μm z-cut quartz crystal (this is consistent with observations by Moon et al.[177] who observed similar spectral patterns with the SF spectrum centered near 400 nm). A thinner z-cut quartz window could be used to reduce the effects of the temporal walk-off. However, the tradeoff is the decrease in the interaction length, which will reduce conversion efficiency. Furthermore, handling such a thin crystal can be experimentally challenging. Petersen and co-workers employ a 150 nm

thin film of zinc oxide deposited on soda lime glass to generate the local oscillator for heterodyne-detected vibrational SFG spectroscopy, which might be a viable alternative method to generate the local oscillator with reduced spectral modulation.[174]

Probing the Air/Water and Liquid/Liquid Interface using a Flat-Jet

One of the shortcomings of ESFG spectroscopy is its inherently weak signal strength due to the signal being generated from only a few monolayers at the interface when probing planar aqueous interfaces. Thus, relatively long acquisition times (ca. 1-10 minutes) are necessary to obtain sufficient signal-to-noise ratio. Furthermore, concentrations typically used in the experiments range from 1-5 M to generate sufficient SFG photons. However, as described in previous chapters, long acquisition times risk surface contamination from airborne particulates and formation of laser-induced photoproducts. Moreover, ion-ion interactions become prominent at such high concentrations at the interface, which can complicate spectral interpretation.

A continuously flowing flat-jet sheet allows for ESFG spectroscopy of a continuously refreshing aqueous interface that circumvents the issues presented above for a static aqueous sample surface contained in a conventional Petri dish. Roke et al. demonstrated vibrational SFG spectra in the $-CH_3$ stretch region of the ethanol/air interface of a cylindrical microjet.[179] However, a limitation of the cylindrical jet setup is its inherently curved interface. Recently, Koralek et al. developed ultrathin liquid flat-jets, utilizing microfluidic technology that allows for stable liquid jets ranging in thickness from microns to tens of nanometers.[60] Furthermore, Koralek and co-workers have developed two-component flat-jets that would allow studies of liquid-liquid interfaces[180] with nonlinear spectroscopy which has not yet been extensively explored. Incorporating a flat-jet in the broadband DUV-ESFG spectroscopy system would allow for measurements of low concentration solutions or analytes with lower ESFG cross-sections. For example, azide,[181] carbonate species,[182] hydroxide,[183] iron-chloride complexes,[184] sulfur dioxide,[185] and other sulfur species.[186]

Lastly, measuring concentration effects in broadband DUV-ESFG spectra could better our understanding of how ion pair and ion cluster formation are manifested in interfacial electronic spectra. Additionally, the mixing capabilities of the two-component flat-jet system could be used to mix two reactant solutions and study reaction kinetics or to probe liquid/liquid interfaces.

Chapter 7 Probing Liquid Carbon with Soft X-ray Free Electron Laser Spectroscopy: An Overview

Liquid Carbon

The liquid state of carbon is of fundamental chemical significance and has potential practical applications, but it remains very poorly characterized (see Ref[187] for a recent review by our group). As a time-honored prototype of tetrahedral bonding, which generates important solid structures, the study of liquid carbon could lead to the discovery of novel forms of carbon, much as the study of small carbon clusters led to the serendipitous discovery of fullerenes and carbon nanotubes.[188] Evidence suggests that carbon nanotubes are formed in carbon arcs by nucleation from a liquid carbon precursor.[189] A recent study reports that a new, metastable state of carbon (Q-carbon) is formed through a liquid intermediate.[190] Novel carbon materials and routes for synthesizing them are of great interest, as some proposed carbon allotropes may have exciting new properties for technological applications, and better understanding of the liquid properties may suggest new routes for synthesizing known carbon materials of technological significance with improved control of product properties.

To reliably model such processes requires a far more detailed understanding of the liquid state than is currently available. As extreme pressures and temperatures are required for the generation of equilibrium liquid carbon, transient methods, including pulse electrical heating and ultrafast laser-induced non-thermal melting[191,192] must be exploited to prepare liquid samples for characterization. Some electrical properties of liquid carbon have been deduced from pulse electrical heating experiments,[193] and both X-ray and optical reflectivity experiments have been performed on non-thermally melted samples.[191,192] The results of these experiments on carbon have proven controversial, with different studies reaching different conclusions regarding the properties of the liquid state.

Previous X-ray absorption spectroscopy (XAS) studies of non-thermally melted liquid carbon were hampered by limited time and energy resolution.[194] Data obtained in these experiments demonstrated a large change in the XAS from the initial solid. This change was ascribed to a weakening of bonds between carbon atoms. By fitting the spectra, the authors were able to predict the number of π-bonds per carbon atom, which exhibited a dramatic and density-dependent change upon melting. X-ray scattering studies of shock-compressed liquid carbon also show complex bonding, but were limited in terms of accessible scattering angles and by requiring extremely high pressures.[195] In 2020, FERMI scientists published results of time-resolved XAS on non-thermally laser melted amorphous carbon films and found a transient equilibrium condition at 14,200 K and ~0.5 Mbar in ~300 fs before ablation.[196] Recent *ab initio* molecular dynamics studies[197] have modeled the liquid and its position in the carbon phase diagram, as well as the evolution of carbon under extreme conditions, but have had their own inconsistencies.

As there is currently so little known about the structure of liquid carbon, the ability to identify its structures and properties in different pressure and density regimes is of immense scientific interest. Additionally, gaining insight into the dynamical evolution and cooling of the carbon fluid following heating by the optical melting pulse will aid in validating physical models that are used in hydrodynamic modeling of high-energy density physics experiments at free

electron laser facilities. Historically, experiments have focused on acquisition of data in the compression regime[198] and equation of state models are often well-validated for compression, but data regarding ablation and recrystallization of liquids generated from strong interaction with lasers are generally lacking.

Herein, we present results of pump-probe soft X-ray free electron laser spectroscopy studies on laser-induced non-thermally melted carbon samples and accompanying theoretical calculations.

Soft X-ray Free Electron Laser Spectroscopy

Recent technological advances have opened new venues for spectroscopy at soft X-ray energies (ca. > 0.1 nm, < 10 keV). The development of X-ray free electron lasers has enabled researchers to probe systems using ultrafast and tunable soft X-ray beams with high coherence and brilliance.[199] Currently, there are several operating soft X-ray beamlines around the world: PAL-XFEL (South Korea), LCLS (SLAC National Accelerator Laboratory), SPring-8 and SACLA (Japan), FLASH DESY (Hamburg, Germany), SwissFEL (Switzerland), and FERMI Elettra (Italy), with some existing beamlines undergoing upgrades and new facilities in construction.

Due to their high intensities and short pulse lengths, soft X-ray free electron laser sources provide an exciting and novel way to study materials. Specifically, PAL-XFEL[200] in Pohang, South Korea (Figure 23) is well-suited to probing the carbon *K*-edge because of its high performance at the relevant photon energy range as well as its short pulse duration, which allowed for the study of the time evolution of carbon electronic structure as it undergoes melting, expansion, cooling, and ablation.

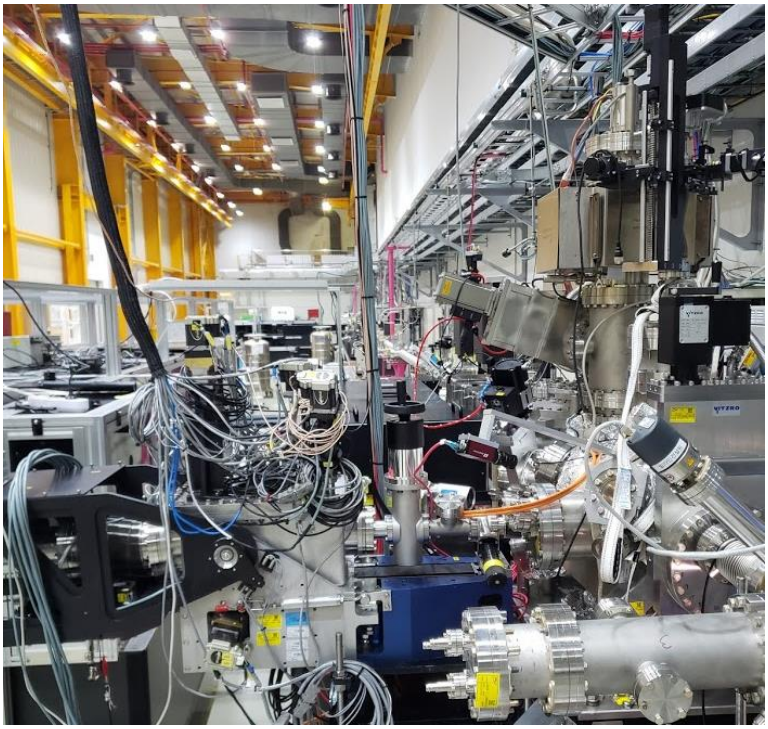

Figure 23. Soft X-ray scattering and spectroscopy endstation at PAL-XFEL in Pohang, South Korea. Photo by Hikaru Mizuno.

Time-Resolved X-ray Emission Spectroscopy and Resonant Inelastic X-ray Scattering Spectroscopy of Liquid Carbon

Unpublished material in this section is included with permission from Rebecca K. Lindsey, Sebastien Hamel, Kamal Chinnathambi, Sumana L. Raj, Christopher J. Hull, Soonnam Kwon, Sang Han Park, Jason K. Cooper, Feipeng Yang, Yi-Sheng Liu, Jinghua Guo, Dennis Nordlund, Walter S. Drisdell, Heather D. Whitley, Michael Odelius, Craig P. Schwartz, and Richard J. Saykally.

XPS measurements of unmelted samples were performed by J.K.C. at Lawrence Berkeley National Lab, XES and RIXS spectra of unmelted samples were measured by F.Y., Y.L., and J.G. at the Advanced Light Source, XAS measurements of unmelted samples were measured by D.N. at SLAC National Accelerator Laboratory, MD simulations were performed by R.K.L., S.H., and H.D.W. at Livermore National Laboratory, electronic structure calculations were performed by K.C. and M.O. at Stockholm University.

Introduction

Due to its elemental specificity and sensitivity to the local structure and bonding, time-resolved soft X-ray free electron laser spectroscopy is a powerful tool to explore the melting dynamics of carbon as it evolves and cools to the glassy state or ablates. X-ray emission spectroscopy (XES) and resonant inelastic X-ray scattering (RIXS) spectroscopy are photon-in photon-out spectroscopy techniques (Figure 24). In the case of carbon, absorption of an X-ray photon promotes an electron from the core level into the continuum (XES) or to an empty valence band state (RIXS), resulting in an excited intermediate state with a core hole. Subsequently, an electron from an occupied valence shell fills the core hole ($2p \rightarrow 1s$), resulting in an emission of an X-ray photon. Generally, XES probes the occupied electronic structure of a material in an element-specific manner. In RIXS spectroscopy, tuning the incident X-ray photon energies allows one to simultaneously obtain information of both the empty electronic states and occupied states.

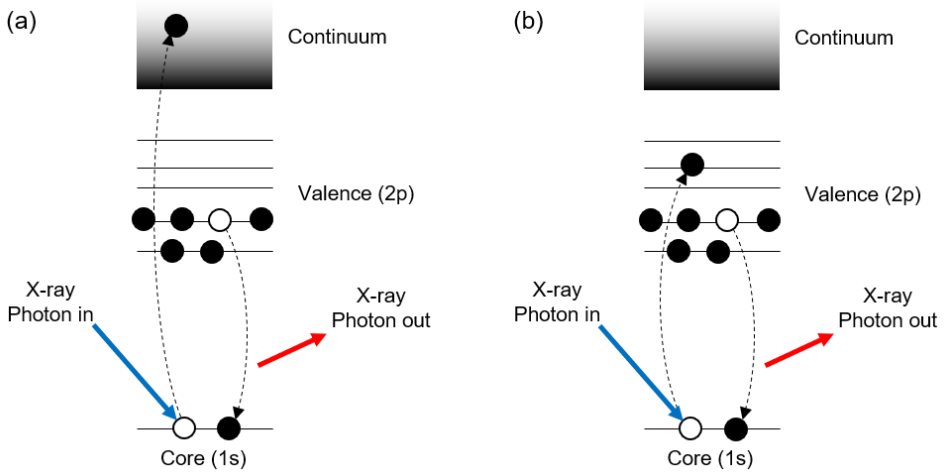

Figure 24. Energy diagram of (a) X-ray emission process and (b) resonant inelastic X-ray scattering process at the carbon *K*-edge. Incident X-ray photon excites a 1*s* core electron to continuum (XES) or an empty 2*p* valence band (RIXS) state. An electron from an occupied valence state fills the core hole, resulting in an emission of an X-ray photon.

Theoretical results for liquid carbon simulated under nominally identical conditions can generate vastly different electronic structure predictions due to differences in functionals, electron temperature treatment, and levels of theory.[201] XES and RIXS are highly sensitive to the underlying electronic and atomic structure and can probe bond strength, average number of bonds, and the nature of interactions between carbon atoms, and can distinguish between different carbon compounds.[202] XES can also be used to characterize the temperature of a material. Such experiments were recently demonstrated for aluminum at FLASH by measuring XES as a function of temperature.[203] Time-resolved RIXS (tr-RIXS) has also been demonstrated at FLASH for liquid silicon, a metastable tetrahedral system, in providing detail into the structure and relevant phase changes; a phase change between solid and liquid, and subsequent liquid-liquid phase transition between high- and low-density liquids were identified, only made possible with detailed electronic and structural information gained from tr-RIXS data.[204]

Our group recently obtained ultrafast grazing incidence X-ray scattering data from laser-ablated silicon at SACLA, showing that large-scale structures are formed after ~20 ps.[205] While this is similar to what occurs in conventional explosions, the effects occur significantly more rapidly than previously observed and may provide valuable insight into the nature of liquid carbon. Herein, we report the first tr-RIXS and tr-XES experiments performed on liquid carbon and accompanying theoretical calculations. Different temperature/pressure conditions are obtained by probing at different delay times between the melting pulse and soft X-ray probe pulse.

Materials & Methods

Samples comprising of amorphous carbon (a-C) thin films (thickness 100 nm, roughness 0.80 nm, ρ = 2.1 g cm^{-3}) deposited on a silicon <100> wafer were purchased from Incoatec GmbH (Germany) for tr-RIXS experiments. Ultrananocrystalline diamond (UNCD) thin films (thickness ca. 400 nm) deposited on silicon <100> wafer were purchased from John Crane (USA) for tr-XES and tr-RIXS experiments.

The pump-probe tr-RIXS and tr-XES experiments were performed at the soft X-ray scattering and spectroscopy beamline at Pohang Advanced Laboratory (Pohang, Republic of South Korea).[200] The liquid was prepared by non-thermal melting of carbon targets with a femtosecond laser and then probed as a function of delay time between the melting and soft X-ray FEL pulses (and thus as a function of temperature, as determined by both the experiment and modeling).

The experimental design is shown in Figure 25. The PAL-XFEL and optical melting laser were nearly-collinearly focused onto the sample surface with an incidence angle of ca. 45° with respect to the sample surface normal. Experimental parameters are presented in Table 4. The larger melting laser spot size ensures that the FEL beam probes a nearly homogeneously excited sample. Samples were mounted on a 4-axis stage and rastered shot-to-shot so that each FEL shot probed a pristine surface. The scattered X-ray photons were collected in reflection geometry, perpendicular to the incoming beams, using a RIXS/XES spectrometer and Newton DO 940 CCD detector (Andor Oxford Instruments). A CCD image was recorded as a 1×2048-pixel image file for each shot.

Tr-RIXS spectra of non-thermally melted a-C samples were collected at incidence energies of 289 eV, 297 eV and 298 eV as a function of time delay between the melting pulse and PAL-XFEL pulse, ranging from Δt = +1 to +50 ps with a time resolution of ca. 150 fs.

Tr-XES and tr-RIXS spectra of non-thermally melted UNCD thin film samples were collected at incident energies of 308 eV, 303 eV, and 294 eV as a function of time delay between the melting pulse and PAL-XFEL pulse, ranging from $\Delta t = -1$ to +100 ps with a time resolution of ca. 150 fs.

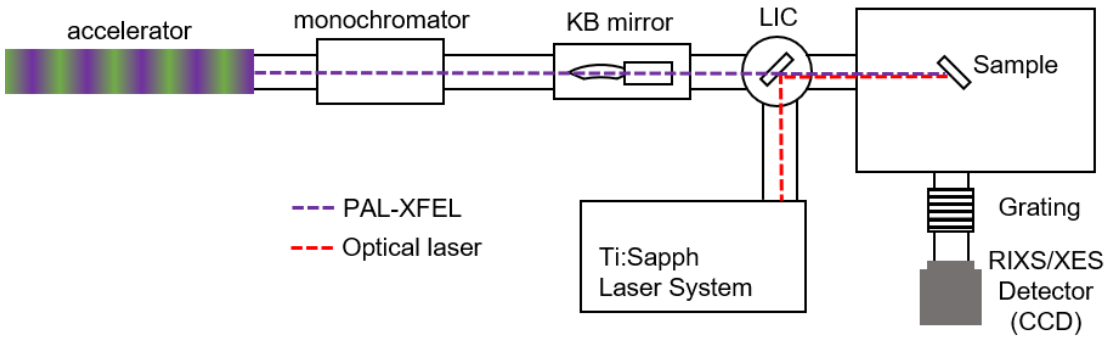

Figure 25. The experimental design for time-resolved resonant inelastic X-ray scattering and X-ray emission spectroscopy at the soft X-ray scattering and spectroscopy beamline at Pohang Accelerator Laboratory. Some optics are omitted for clarity. (KB: Kirkpatrick-Baez mirror; LIC: laser in-coupling mirror).

Table 4. Laser parameters for tr-RIXS and tr-XES experiments at PAL-XFEL.

	PAL-XFEL	Melting Laser	
		tr-RIXS a-C	tr-RIXS/XES UNCD
Spot size, fwhm (μm)	80 μm	200 μm	200 μm
Energy	289, 294, 297, 298, 303, 308 eV (pink beam)	1.55 eV / 800 nm	1.55 eV / 800 nm
Pulse duration (fs)	< 50	65	65
AOI	45°	45°	45°
Pulse Energy (μJ)	--	528	565
Peak Fluence (J cm^{-2})	--	0.82	0.88
Peak power (W cm^{-2})	--	1.3×10^{13}	1.4×10^{13}

For further characterization and comparisons to benchmark theoretical calculations, additional measurements were performed. XAS of unmelted a-C thin films were performed at Stanford Synchrotron Radiation Lightsource (SLAC National Accelerator Laboratory, Menlo Park, CA, USA).[206] XES and RIXS of unmelted a-C and UNCD thin films were performed at Advanced Light Source (Lawrence Berkeley National Laboratory, Berkeley, CA, USA).[207] XPS of unmelted a-C and UNCD thin films were measured with a commercial Kα X-ray photoelectron spectrometer (Thermo Fisher Scientific).

Theoretical Methods

To obtain MD snapshots of carbon at extreme temperature and pressure conditions, the Chebyshev Interaction Model for Efficient Simulation ("ChIMES")[208] was employed. ChIMES accounts for two- and three-body interactions by fitting linear combinations of Chebyshev polynomials through force matching to trajectories from Kohn-Sham density functional theory (DFT).[209] Trajectories were obtained at 7000 K, 14000 K, and 17000 K.

For electronic structure calculations, periodic DFT[209,210] based calculations were performed using the CP2K package[211] to simulate the carbon *K*-edge XAS and XES spectra for diamond, graphite, and amorphous carbon from MD trajectories. A Gaussian Augmented Plane Wave (GAPW) method to perform all-electron calculations with 6-311Gdp basis set and an energy cut-off of 500 Ry with multi-grid consisting of five grids was employed. A supercell of 5×5×5 (1000 atoms), 8×8×3 (768 atoms), and ~17 Å sized cubic box (500 atoms) for diamond, graphite, and a-C was used. Calculations were performed at 0 K and for the Γ point of super cells using the transition potential method; the half core-hole (TPHH) approximation to include C 1*s* core hole relaxation effects on spectra was used. Separate spectrum simulations were performed for each carbon atom present in the a-C cell and only for inequivalent atoms in diamond and graphite cells.

Data Analysis

Time-resolved RIXS. Each dataset comprised 20,000-72,000 FEL shots, with each shot saved as a 1×2048-pixel image file. A representative raw RIXS spectrum of unmelted carbon from a single dataset is shown in Figure 26a. To display the RIXS spectrum, background removal and signal filtering were performed based on the methods developed by Nowak et al.[212] Initially, the baseline background intensity was estimated using the minimum value for each pixel within the dataset and subtracted from all frames. Then, to account for sharing of X-ray photons depositing energy among neighboring pixels, a 3-pixel re-clustering of the pixels was performed (*i.e.*, each pixel was the sum of itself and its neighboring pixels). When the re-clustered pixel intensity was below a user-defined threshold, the central pixel of the 1×3-pixel block was identified as a background. The median value was calculated from the background identified pixels to obtain the optimized background, which was subtracted from each frame. After optimized background subtraction, a 3-pixel re-clustering of the resulting data was performed. When the value of the re-clustered intensity was above a user-defined threshold, then the central pixel was identified as an X-ray photon event and all but the X-ray pixels and their neighboring pixels were set to zero. The filtered RIXS spectra were normalized by the number of shots and FEL intensity, binned, and smoothed using a smoothing spline fit. Spectra obtained at the same delay times were averaged after normalization and smoothing.

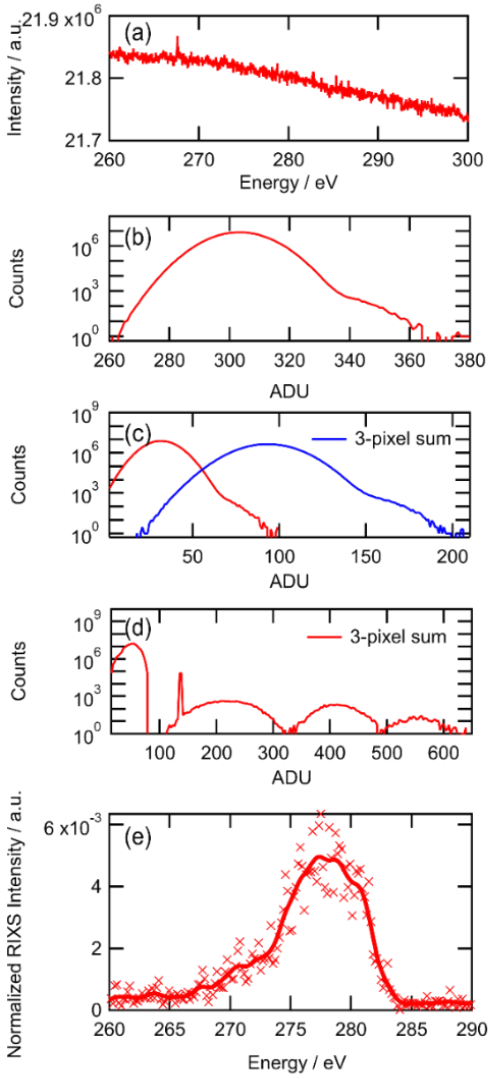

Figure 26. An overview of data analysis steps employed to remove background and isolate RIXS signal. (a) Raw RIXS spectrum of unmelted amorphous carbon comprising 72000 FEL shots with input energy 298 eV. (b) Histogram of raw pixel intensities with baseline/background peak at ~300 ADU and RIXS photons at ~350 ADU (analogue-to-digital-units, *i.e.*, counts). (c) Histogram of baseline-subtracted intensities (red) and 3-pixel re-clustered intensity (blue). (d) Histogram of 3-pixel re-clustered intensity after subtracting optimized background. (e) Filtered RIXS spectrum (×, red) with spline smoothing (solid line, red).

Time-resolved XES. Each dataset contained 10,000-100,000 FEL shots, with each shot saved as a 1×2048-pixel image file. Lower and upper limits were set to remove noise. The filtered XES spectra were normalized by the number of shots and FEL intensity, binned, and smoothed using a smoothing spline fit. Spectra obtained at the same delay times were averaged after normalization and smoothing.

X-ray Photoelectron Spectra. XPS spectra were fit using CasaXPS (Casa Software Ltd).

Results & Discussion

XAS, XES, RIXS, and XPS spectra of unmelted a-C at room temperature were measured to benchmark theoretical results (Figure 27, Figure 28). The XAS spectrum shows the characteristic 1*s*→π* transition near 286 eV from sp^2-carbons and the broad 1*s*→σ* band at higher energies (>290 eV) from sp^3-carbons. The XES/RIXS spectra shows features near 277 eV and a shoulder at 282 eV corresponding to states with 2*s* and 2*p* character.

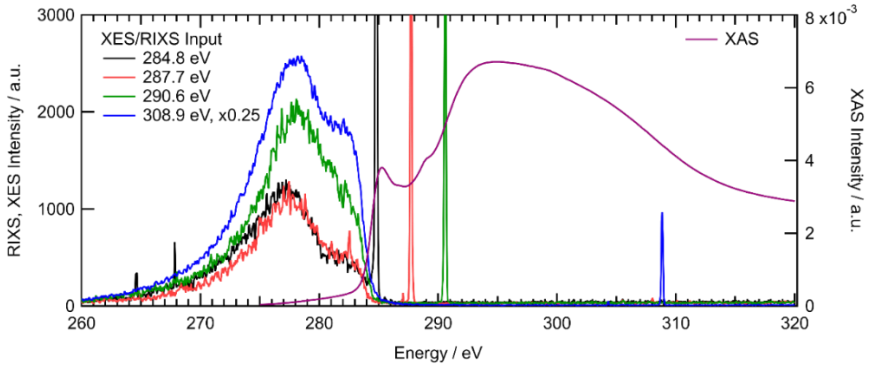

Figure 27. Carbon *K*-edge XES, RIXS, and XAS spectra of unmelted amorphous carbon film. The sharp peaks present in the RIXS and XES spectra are elastic scattering peaks.

The XPS spectrum of unmelted a-C (Figure 28) was deconvoluted to determine the sp^3 content (%sp^3) and the sp^2/sp^3 ratio.[213–215] The binding energy peaks at 284.3 eV (FWHM 1.05 eV) and 285.2 eV (FWHM 1.37 eV) correspond to sp^2- and sp^3-carbon atoms, respectively. The difference (0.9 eV) is consistent with the energy difference between the C 1*s* core levels of graphite and diamond. Other peaks present in the spectrum with much smaller intensity are attributed to surface oxygen contamination (C-O, C=O). The %sp^3 content is calculated as the area over the total C 1*s* peak area, which is ca. 26%, and the sp^2/sp^3 ratio was calculated to be ~2.1. These values are consistent with those reported by Ref.[214] from a-C samples with similar densities as used here. It should be noted that XPS is considered a surface-selective technique (probe depth ~3 nm, depending on incident photon energy). Haerle et al.[214] reported that values obtained from XPS are similar to those obtained measuring plasmon resonance in EELS spectrum.

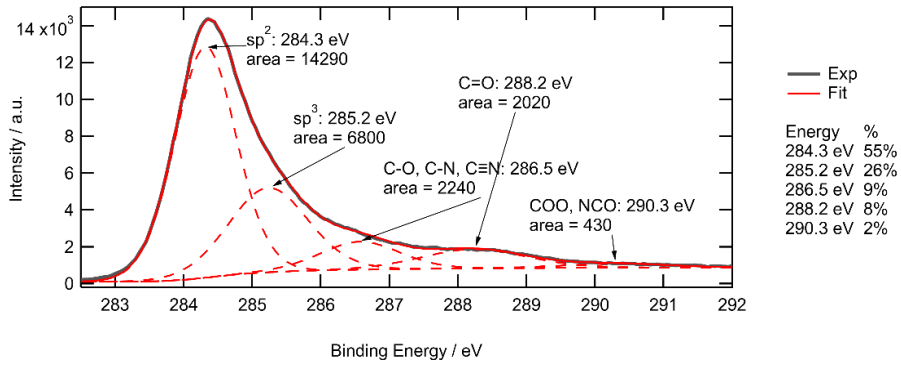

Figure 28. Deconvolution of X-ray photoelectron spectra of C 1s peaks of unmelted amorphous carbon. Peaks at 284.3 eV (FWHM 1.05 eV) and 285.2 eV (FWHM 1.37 eV) correspond to sp^2- and sp^3-carbon atoms.

XES, RIXS, and XPS spectra of unmelted UNCD thin films at room temperature were measured to benchmark theoretical results (Figure 29). The XES spectra shows a broad feature near 279 eV corresponding to states with 2*s* character and a small shoulder near 272 eV.

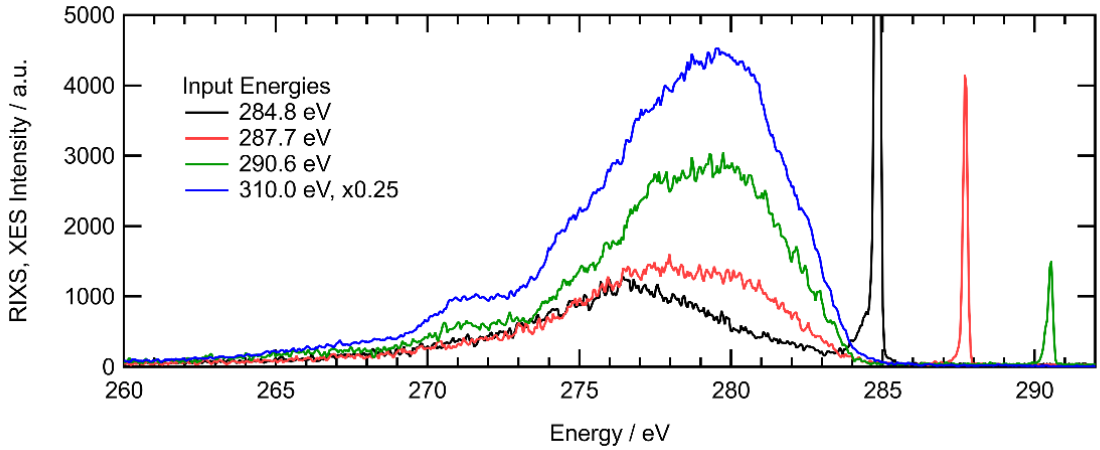

Figure 29. Carbon *K*-edge XES and RIXS spectra of unmelted ultrananocrystalline diamond thin film. The sharp peaks present in the spectra are elastic scattering peaks.

The XPS of UNCD (Figure 30) was fit to obtain %sp^3 of ca. 54% and sp^3/sp^2 ratio of ca. 22.[216] The relatively large contribution from C-O-H in the near-surface region probed by XPS is likely from surface termination and grain boundaries.[217] The grain boundaries of nanocrystalline diamond will contain sp^2-carbon, defects, and hydrogen so the XPS spectrum is not expected to exactly match that of a pristine diamond crystal.[218]

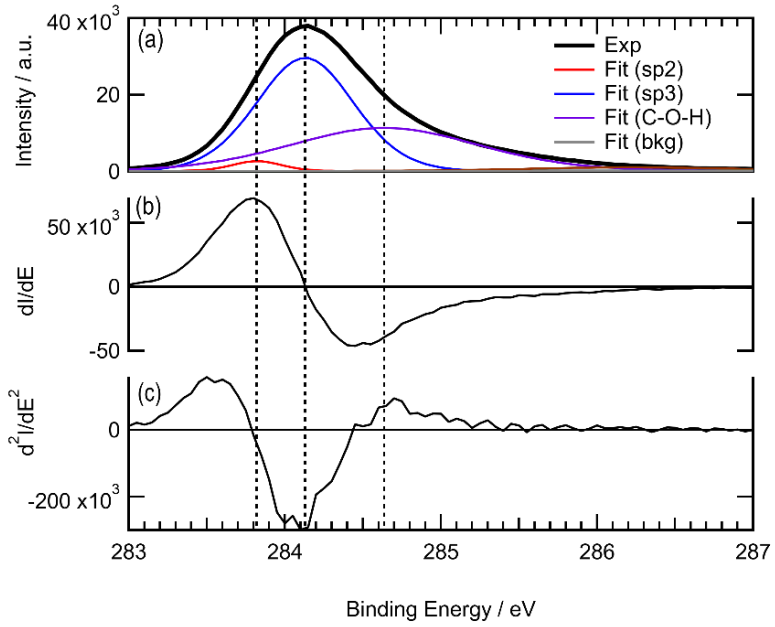

Figure 30. (a) Deconvolution of X-ray photoelectron spectra of C 1s peaks of unmelted ultrananocrystalline diamond thin film. (b) First and (c) second derivatives of the XPS spectral profile. Area (sp^3) = 23391, area (sp^2) = 1043, area (C-O-H) = 19129.

Tr-RIXS spectra of liquid carbon generated from a-C samples were collected at 289 eV, 297 eV, and 298 eV (Figure 31). The RIXS spectra of unmelted carbon (Figure 27) show a broad main peak centered at 278 eV, assigned to emission from σ-orbitals, and a higher energy shoulder near 281 eV, assigned to emission from π-orbitals. Upon melting, the normalized integrated tr-RIXS intensity (Figure 32) shows a sharp initial decrease (+1-2 ps), subsequent recovery (+4 ps), and eventual decrease at long delay time.

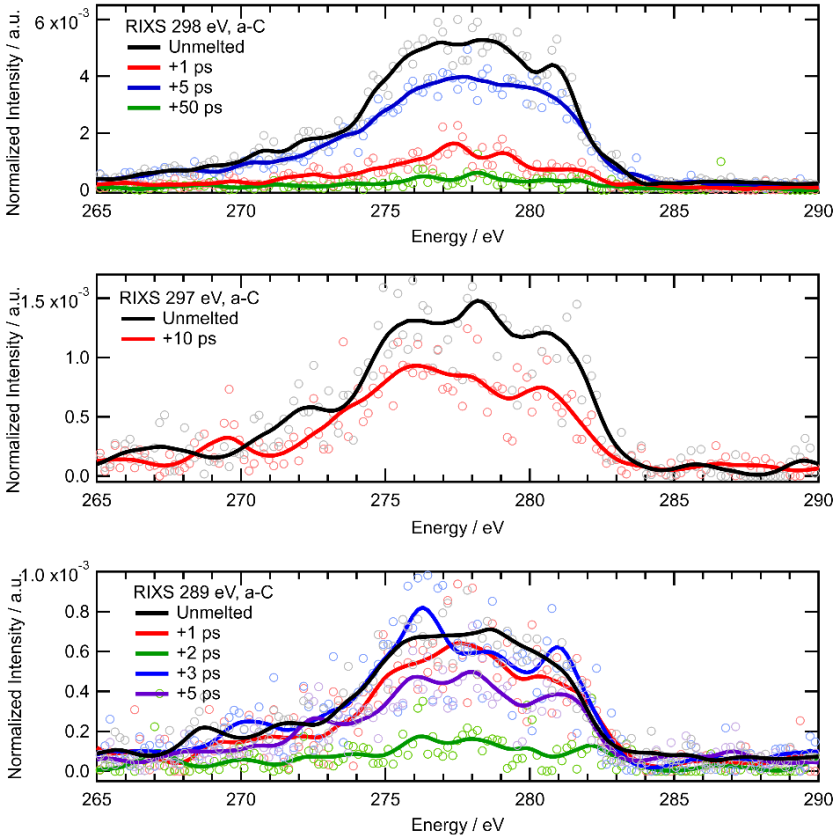

Figure 31. Time-resolved RIXS spectra of amorphous carbon measured at (a) 298 eV, (b), 297 eV, and (c) 289 eV at various time delays. Spectra are filtered, normalized, and smoothed.

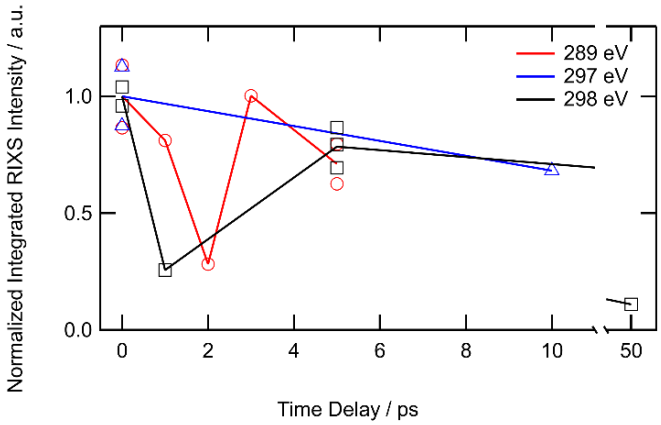

Figure 32. Normalized integrated RIXS intensity as a function of delay time for amorphous carbon. The area of unmelted RIXS spectrum for each excitation energy is normalized to 1.

Tr-XES spectra of liquid carbon from UNCD thin films were collected at 308 eV (Figure 33). Because the UNCD samples were thicker than a-C samples that were previously used, contributions from both melted and unmelted sample in the measured spectra are expected, hence the changes in the tr-XES spectra upon melting are not as obvious as those of a-C. The total integrated area and difference spectra are shown in Figure 34. Upon melting, there is an initial increase in the integrated XES intensity followed by a decrease. Spectral features at 286 eV, 282 eV, and 277 eV at short delay times, corresponding to similar features in the spectrum of highly oriented pyrolytic graphite (sp^2) are observed (Figure 34b). At +20 ps, the XES intensity increases, then returns to initial intensity levels at longer delay time.

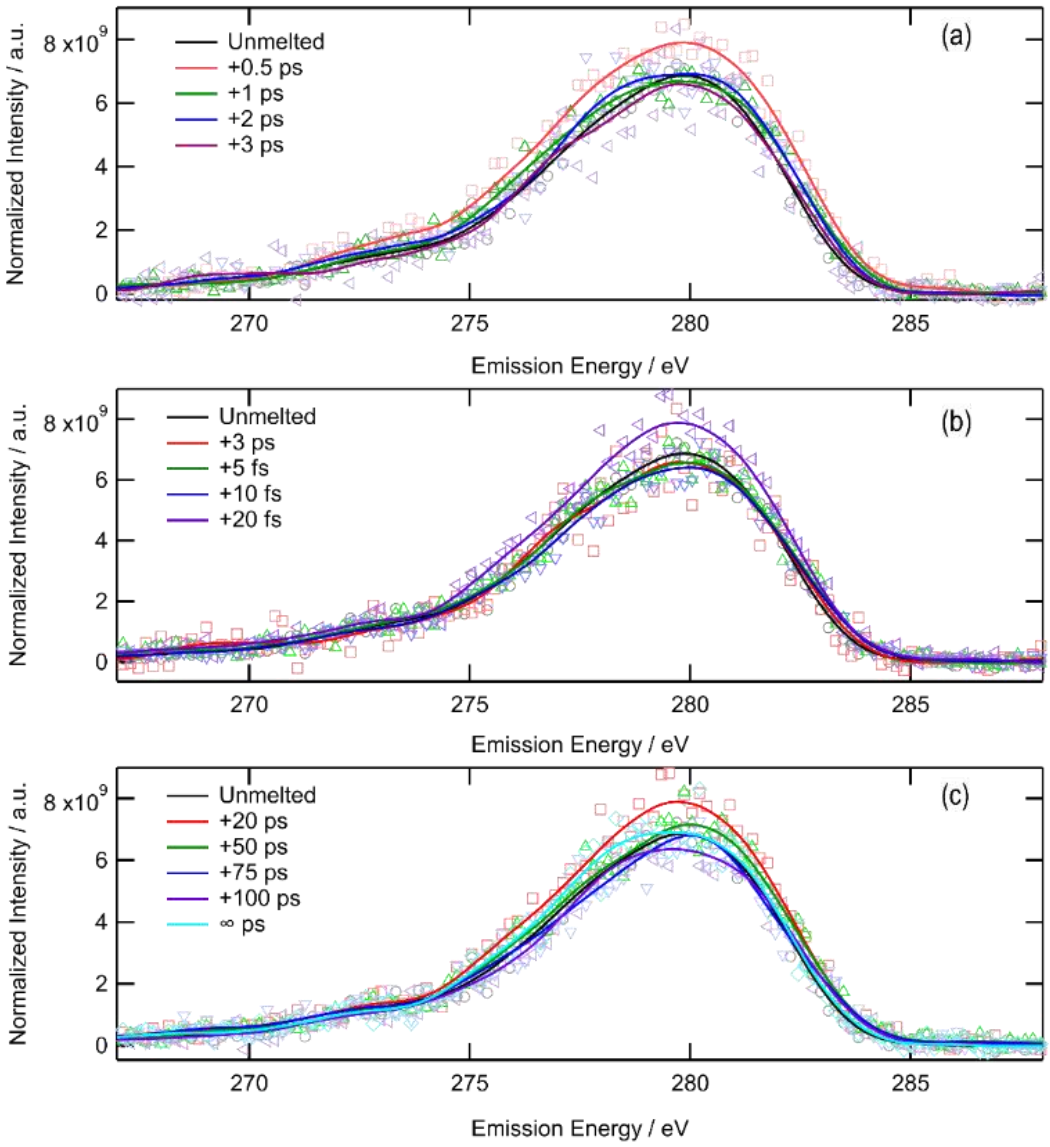

Figure 33. Time-resolved XES spectra of ultrananocrystalline diamond thin film measured at 308 eV at (a) short, (b) intermediate, and (c) long delay times. Spectra are filtered, normalized, and smoothed.

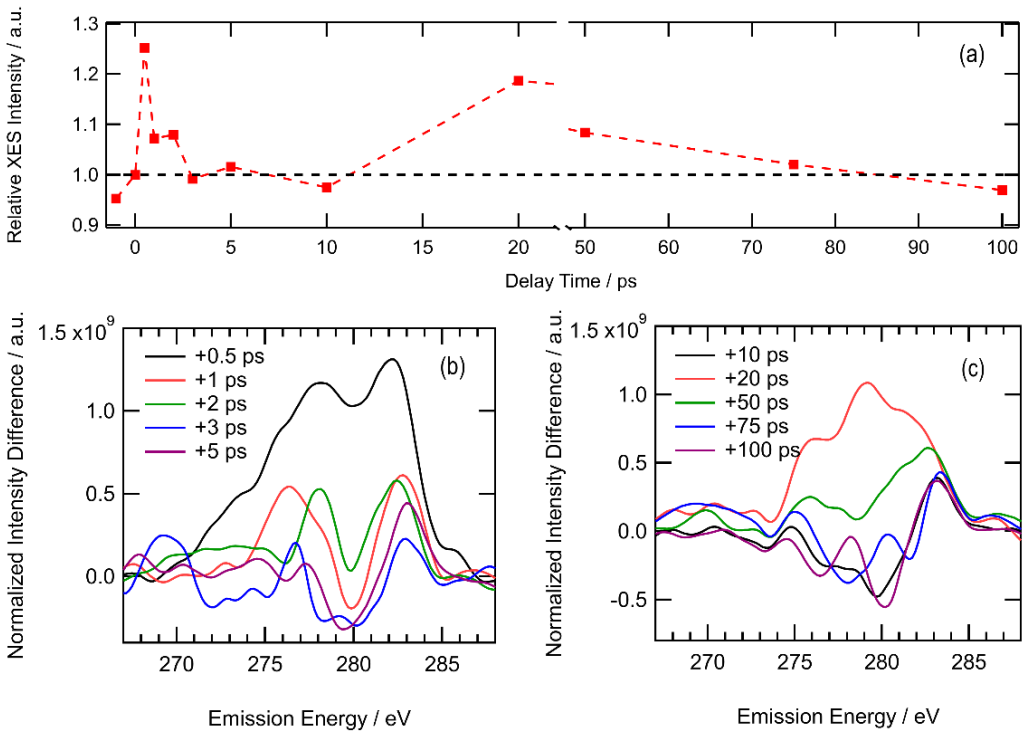

Figure 34. (a) Integrated XES intensity (total area between 265 eV and 288 eV) vs. delay time for ultrananocrystalline diamond thin film samples. XES difference spectra for (b) short and (c) long delay times.

Tr-RIXS spectra of liquid carbon from UNCD measured at FEL incidence energies of 294 eV (Figure 35) and 303 eV (Figure 36) are presented below.

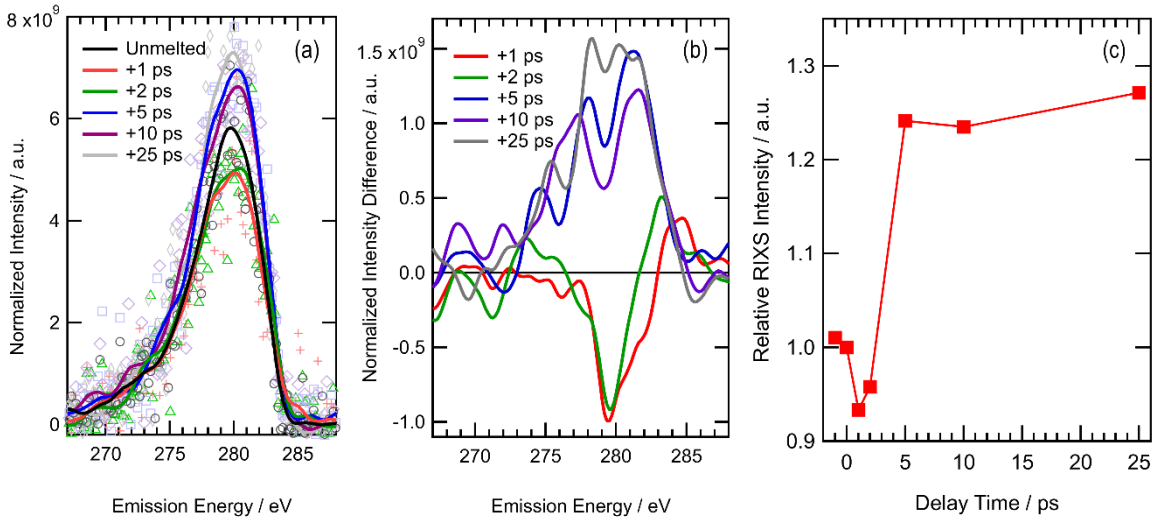

Figure 35. (a) Time resolved RIXS spectra measured from ultrananocrystalline diamond thin film samples with FEL energy 294 eV, (b) RIXS difference spectra, and (c) integrated RIXS intensity vs. delay time.

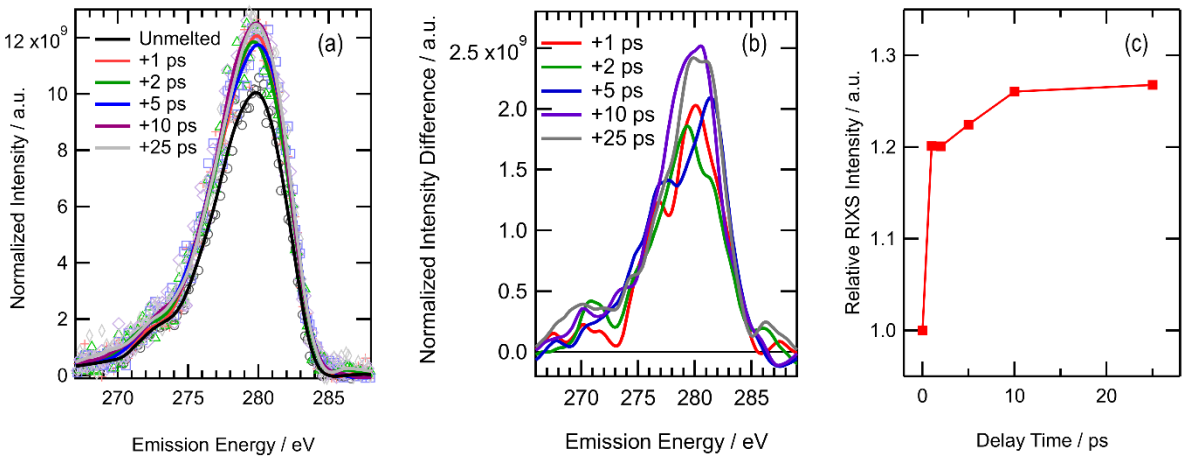

Figure 36. (a) Time resolved RIXS spectrum measured from ultrananocrystalline diamond thin film samples with FEL energy 303 eV, (b) RIXS difference spectra, and (c) integrated RIXS intensity vs. delay time.

In the short time regime (Δt = 0-2 ps), the liquid is expected to be in a non-equilibrium state with high electronic temperature and low lattice temperature. The initial decrease in the RIXS signal intensities for a-C (289, 298 eV; Figure 32) and UNCD (294 eV, Figure 35c) is likely due to a decrease in the absorption cross-section. At low densities, the liquid is expected to be primarily *sp*-hybridized carbon chains, with increasing coordination with increased fluid density. The results of our experiments are consistent with time-resolved XAS measurements on a-C made at FERMI.[196] In tr-XAS spectra measured by Principi and co-workers, the absorption cross-section of sp^2 carbons corresponding to absorption >290 eV was observed to decrease rapidly (within 150 fs) due to increasing *sp*-hybridization as structural reorganization occurred to form the liquid phase.[196] With a decrease in absorption cross-section of the incident X-ray photons at higher incident energies during short delay times, the RIXS intensity concomitantly decreases.

Beyond +5 ps, the liquid will begin to expand, cool, and/or ablate. This time regime is especially relevant to the production of novel carbon materials, as both carbon nanotubes and Q carbon are speculated to nucleate from liquid carbon as it cools.[189] Further efforts, including AFM and TEM, to examine whether novel structures have actually formed in in the laser melt craters are underway. Our group's recent ultrafast grazing incidence X-ray scattering data for laser-ablated silicon showed large-scale structure formation attributed to development of nanoscale inhomogeneities typically associated with nanoparticles and structures +20 ps after non-thermal melting.[205] Similar behavior could be occurring in the a-C and UNCD samples, as recovery of RIXS and XES signal intensity at intermediate delay times are observed.

Preliminary calculations of XAS (Figure 37) and XES (Figure 38) spectra are shown below. At high temperatures, the XAS cross-section decreases at higher energies (>290 eV) and increases at lower energies (<290 eV), with decreasing coordination number, consistent with our observed tr-RIXS measurements at short delay times. The calculated XES shows a prominent feature near 285 eV for carbons with low coordination numbers, which also appears to be consistent with tr-XES data at short delay time (+0.5 ps). Further work is needed here, as the calculated spectra do not exactly match those of the experiments. Here, it is important to note that there is not just a single species of carbon in the probe volume at various delay times as special and structural

reorganization occurs. There may be neutral C atoms and radicals in the generated plume;[219] short-lived polymer-like, nano-, and/or glassy structures,[220] and even novel structures (*e.g.*, pseudo-sp^3 "diaphite" configurations[221]) in the probe volume that are challenging to deconvolute.

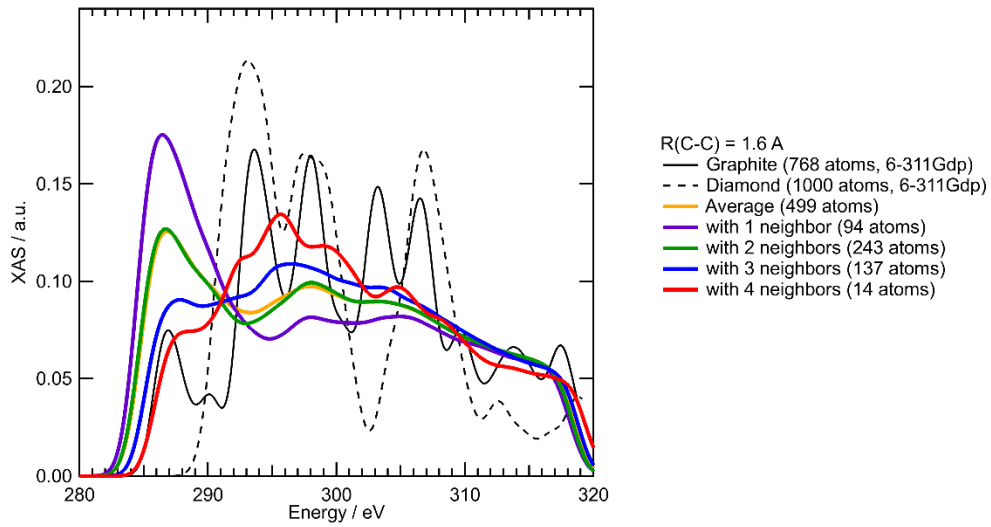

Figure 37. Calculated XAS at carbon *K*-edge for different groups of carbon based on different number of nearest neighbors at 7000 K.

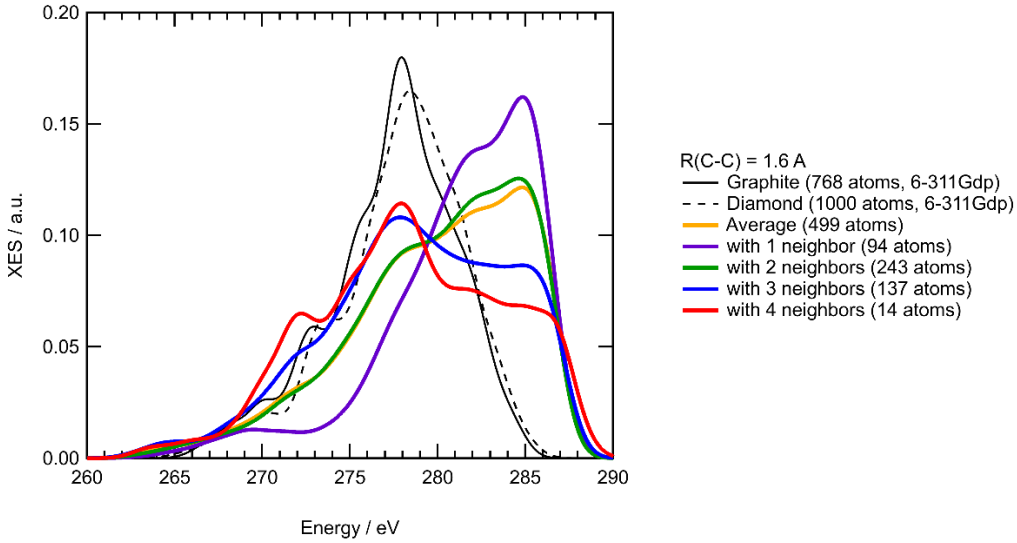

Figure 38. Calculated XES at carbon *K*-edge for different groups of carbon based on different number of nearest neighbors (neighbors defined by cutoff radius of 1.6 Å) at 7000 K.

Conclusions

Tr-RIXS and tr-XES spectra of liquid carbon were measured from a-C and UNCD thin film samples at PAL-XFEL. An initial decrease in tr-RIXS signal intensity at short delay times was observed, consistent with tr-XAS measurements, corresponding to the decrease in XAS cross-section of sp^2-hybridized carbon atoms as structural reorganization occurs to form liquid carbon.

In tr-XES spectra, features near 285 eV corresponding to low coordinated carbon atoms at short delay times were observed. With additional theoretical work, we hope that these results can be used to examine and validate theoretical studies that indicate the possible failure of widely applied models for the ionic contribution to specific heat in the warm dense matter regime.[198] These data would also be useful in validating atomic physics codes, like CRETIN[222] that are frequently applied to analyze and model experiments in this regime, which are based on atomic physics models that do not account for details of the electronic structures arising from strong correlations between atoms.

Ultrafast electron diffraction measurements on non-thermally melted freestanding films of single crystal (100) facing diamond at the Warm Dense Matter endstation at LCLS (SLAC National Accelerator Laboratory) are planned for late 2021 to further our understanding of the liquid phase.

Chapter 8 Optical & Soft X-ray Sum Frequency Generation Spectroscopy

Unpublished material in this chapter is included with permission from Sumana L. Raj, Lars Hoffmann, Royce K. Lam, Riccardo Mincigrucci, Laura Fogli, Emiliano Principi, Dennis Nordlund, Walter S. Drisdell, Michael W. Zuerch, Craig P. Schwartz, and Richard J. Saykally.

XAS measurements of unmelted samples were measured by D.N. at SLAC National Accelerator Laboratory.

Introduction

In 2018, the Saykally Group at FERMI[223] and the Matsuda Group (The University of Tokyo) at SACLA[224] independently demonstrated soft X-ray second harmonic generation (SXSHG) spectroscopy for the first time. In the FERMI experiments, the input fundamental energy (ω) was resonant with the carbon *K*-edge and the SXSHG signal at 2ω was detected in transmission geometry through thin graphite film samples. Resonance enhancement was observed when the fundamental was tuned above the *K*-edge; the signal was determined to be interface specific by measuring carbon films of different thicknesses.[223] Recently, our group has successfully probed the boron *K*-edge at a buried boron/Parylene-N interface using the element-specific and interface-sensitive SXSHG spectroscopy at FERMI.[225]

The high coherence, short pulse duration, high brilliance, and tunable energy of the FERMI soft X-ray free electron laser at ELETTRA[226] in Trieste, Italy is well-suited for these ultrafast X-ray measurements.

In 2019, building upon the successful demonstration of SXSHG, our group attempted to measure soft X-ray sum frequency generation (SXSFG) spectroscopy at the carbon *K*-edge at FERMI by mixing an optical laser pulse and soft X-ray laser pulse of EIS-TIMEX. Like SHG spectroscopy, SFG spectroscopy is a surface sensitive probe under the electric dipole approximation.[24,25] In contrast to VSFG and ESFG spectroscopies that probe vibrational and electronic transitions with interface specificity, the elemental sensitivity of X-rays to local structure would make SXSFG spectroscopy a powerful tool for probing interfacial electronic and atomic structure. Hard X-ray (8 keV) + optical (800 nm) SFG had been successfully demonstrated previously in 2012 at LCLS on a diamond crystal sample;[227] however, the technique lacks the interfacial sensitivity of soft X-ray nonlinear spectroscopy.

Proof-of-concept SXSFG spectroscopy experiments in transmission and reflection geometries were attempted at FERMI-ELETTRA but were ultimately unsuccessful. Additionally, some beamtime was spent attempting soft X-ray difference frequency generation (SXDFG) spectroscopy, another second-order nonlinear technique, but were similarly unsuccessful. Below, we discuss the details and possible reasons as to why we were unable to observe signal from the mixing of optical and soft X-ray beams for SXSFG and SXDFG spectroscopies.

Materials & Methods

For SXSFG and SXDFG spectra measured in transmission geometry, free-standing graphite films (thickness 80 nm, 100 nm, and 200 nm; ρ = 2.0-2.2 g cm^{-3}) were purchased from Lebow Company (USA). For SXSFG spectra measured in reflection geometry, amorphous carbon on silicon (thickness 100 nm, roughness 0.80 nm, ρ = 2.1 g cm^{-3}) were purchased from Incoatec GmbH (Germany).

The experiments were performed at the EIS-TIMEX endstation of FERMI at ELETTRA in Trieste, Italy.[228,229] The energies used for the measurements are presented in Table 5 below. The energies were chosen to be below, at, and above the carbon *K*-edge (Figure 39), similar to the previous SXSHG experiments.

Table 5. Experimental details for soft X-ray sum frequency generation (SXSFG) and soft X-ray difference frequency generation (SXDFG) spectroscopy measurements performed at FERMI.

Experiment	Sample	Optical laser 30 μJ/ pulse, 100-fs	FEL < 28 μJ/pulse, 25-fs	Signal
SFG (transmission)	C film	400 nm 3.10 eV	4.01 nm / 309.2 eV 4.74 nm / 261.6 eV	3.97 nm / 312.3 eV 4.68 nm / 264.7 eV
DFG (transmission)	C film	400 nm 3.10 eV	4.34 nm / 285.7 eV	4.39 nm / 282.6 eV
SFG (reflection)	a-C on Si	400 nm 3.10 eV	4.34 nm / 285.7 eV 4.74 nm / 261.6 eV	4.29 nm / 288.8 eV 4.68 nm / 264.7 eV

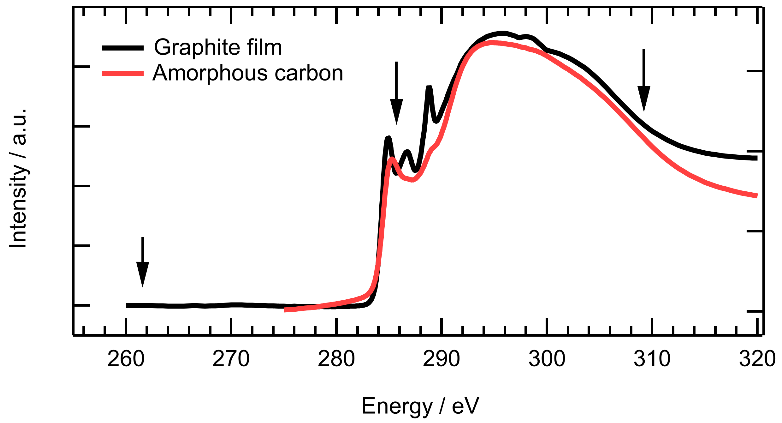

Figure 39. X-ray absorption spectra of 500-nm graphite film (black) and 100-nm amorphous carbon film on silicon substrate. Arrows indicate the FEL energies chosen below, at, and above the carbon *K*-edge for SXSFG measurements.

The collinear transmission geometry design for SXSFG is similar to the SXSHG experiment previously performed at EIS-TIMEX (Figure 40).[223] The FEL (25-fs, spot size ca. 12 × 12 μm^2) and optical laser (400 nm, 100-fs, spot size ca. 60 × 60 μm^2) pulses were spatially and temporally overlapped at the carbon sample in vacuum (ca. 10^{-7} mbar) in collinear geometry at normal incidence. After the sample, the fundamental beams and SFG signal beams directed onto

a grating (HZB 1603-2, 1000 grooves/mm) and then onto a CCD detector (Andor iKon-M SO). The sample was rastered shot-to-shot so each spectrum was measured on a pristine sample. Some beamtime was spent measuring SXDFG, which was done by adjusting the alignment of the grating and position of the detector.

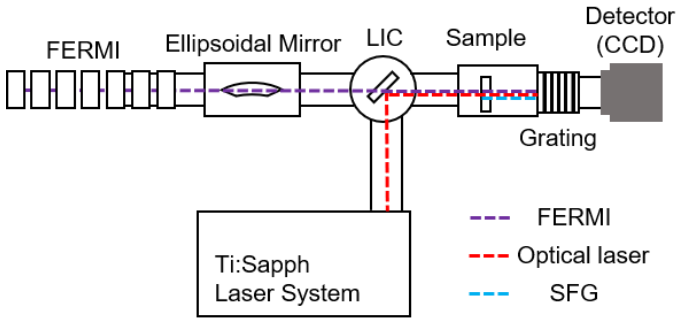

Figure 40. The experimental design of soft X-ray sum frequency generation spectroscopy in collinear transmission geometry at the EIS-TIMEX endstation of FERMI at ELETTRA in Trieste, Italy. Some optics are omitted for clarity. (LIC: laser in-coupling mirror).

Non-collinear reflection geometry SXSFG was also attempted during the beamtime (Figure 41). This design allows for the reflected SXSFG signal and input fundamental beams to be spatially separated. The FEL is focused onto the amorphous carbon sample at an incidence angle of 78° with respect to the surface normal. The optical laser (400 nm) is focused onto the sample at an incidence angle of 12° with respect to the surface normal, from the opposite side. The FEL and optical laser are approximately perpendicular. Both FEL and optical lasers were horizontally polarized (*i.e.*, *p*-polarized). The reflected SXSFG photons will then be ca. 75° from the surface normal, according to the phase-matching equation for 4.34 nm FEL and 400 nm optical laser. The reflected FEL and SXSFG will be spatially separated by ca. 3.1°. A multichannel plate detector is mounted on a circular rail, ca. 12 cm away from the sample so the signal at different angles can be measured. Samples were unable to be rastered during reflection SXSFG measurements.

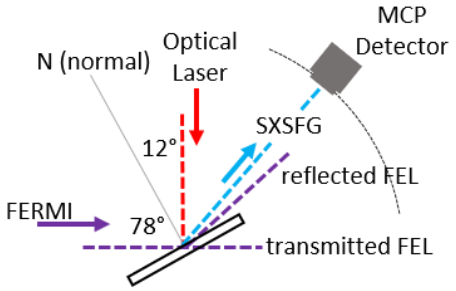

Figure 41. The experimental design of soft X-ray sum frequency generation spectroscopy in reflection geometry at the EIS-TIMEX endstation. The FEL is focused onto the sample at an incidence angle of 78° with respect to the surface normal and the optical laser is focused onto the sample at an incidence angle of 12° with respect to the surface normal. The SXSFG signal should be ca. 75° from the surface normal. A multichannel plate (MCP) detector is mounted on a circular rail approximately 20 cm from the sample. Diagram is not drawn to scale.

Each datafile collected contained 100-500 shots and each shot was saved as a 1024 × 600 pixel image file; using diagnostics data from the Photon Analysis, Delivery, and Reduction System (PADReS),[230] the spectra were filtered to reduce noise arising from FEL instability. Spatial and

spectral filters and a low energy cutoff filter for the FEL shots were applied to spectral data based on methods developed by Lam et al.[223]

Results & Discussion

A representative raw CCD image is shown in Figure 42 for a transmission SXSFG measurement (FEL 4.01 nm, optical 400 nm). The first and second harmonics of the FEL are visible on the spectra and are used to calibrate the energy axis. The spectra were then filtered by looking at the spectral and spatial profiles from PADReS diagnostics information (Figure 43).

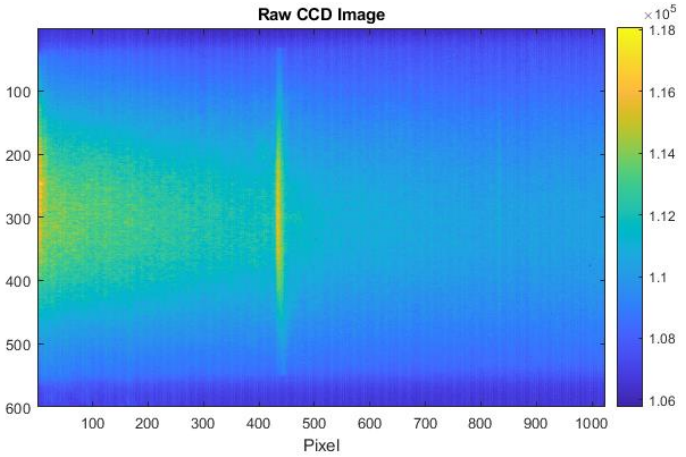

Figure 42. Representative raw CCD image for transmission SXSFG measurement. This spectrum consists of 376 shots with FEL 4.01 nm and 400 nm optical laser. The broad shoulder on the left of the image is the FEL fundamental. The first and second FEL harmonics are visible at 450 pixels and 850 pixels; the peaks corresponding to FEL harmonics were used to calibrate the energy axis.

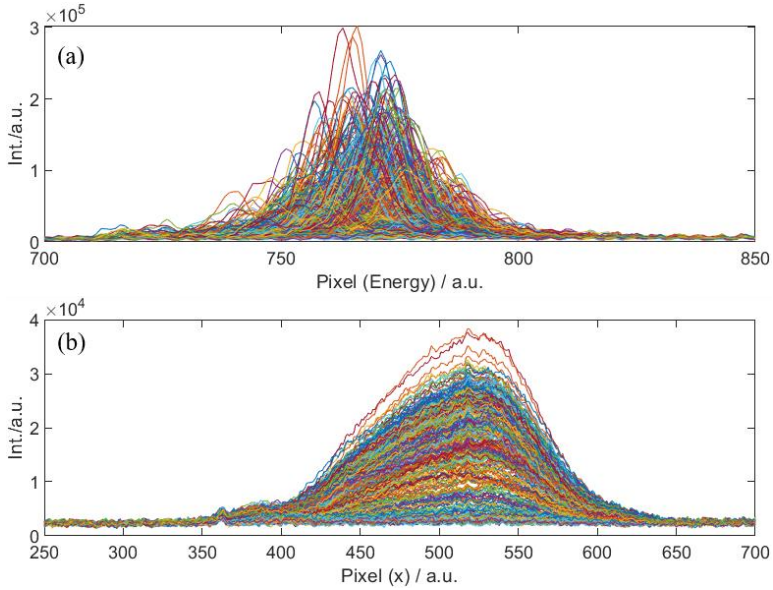

Figure 43. Representative (a) spectral and (b) spatial profiles of FEL shots from Photon Analysis, Delivery, and Reduction System for 376 shots. Full width at half maximum (FWHM) and standard deviations were used to filter FEL shots for further analysis. Shot-to-shot fluctuations are due to FEL instability.

After filtering FEL shots and removing those that were outside filter cutoffs and thresholds, the spectrum below is obtained (Figure 44). The broad shoulder from scattering of the FEL fundamental (309.4 eV) is visible at lower energies. In the collinear transmission geometry, we were hampered by temporal and spatial mismatch in the pulse durations (~20-fs soft X-ray and ~100-fs optical) and spot sizes (60 × 60 μm optical pulse was ca. 30 times larger than 12 × 12 μm soft X-ray pulse). Furthermore, some scattered light on the spectrometer (Figure 44), which may be attributed to the grating or the sample itself, complicated the data filtering and analysis in searching for SXSFG signal. Input energies were chosen in off- and on-resonance conditions (see Table 5 and Figure 39) near the carbon *K*-edge. In the measurements at and above the *K*-edge, resonance enhancement of the SXSFG signal was expected, but also some re-absorption of the SXSFG photons as it passed through the sample. Thin film samples (80-200 nm) were used to reduce significant re-absorption, but no evidence of SXSFG signal in the data was observed.

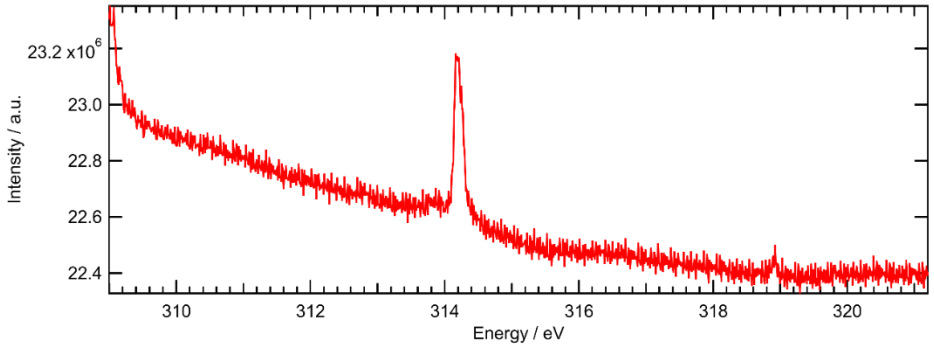

Figure 44. Filtered SXSFG spectrum. Peaks at 314.2 eV and 318.9 eV correspond to first and second harmonics of the FEL. SXSFG photons should occur near 312.5 eV, corresponding to FEL 309.4 eV and optical 3.1 eV input energies.

A representative spectrum from reflection geometry SXSFG experiments is shown in Figure 45. There was no evidence of SXSFG signal observed in the spectra.

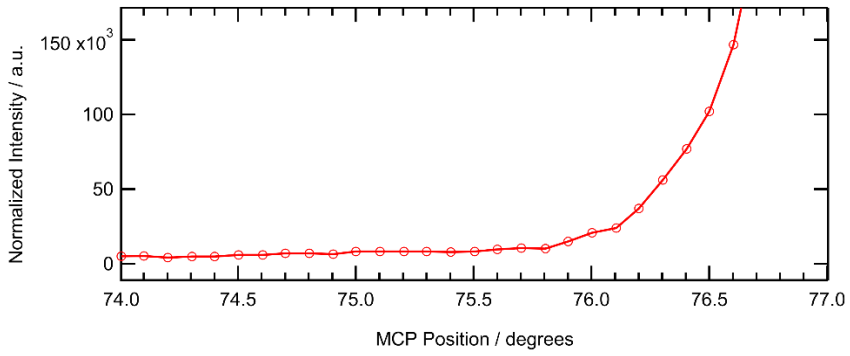

Figure 45. Representative spectrum of SXSFG measured in non-collinear reflection geometry. The reflected fundamental is at ca. 78° and the SXSFG signal should occur at ca. 75° with respect to the surface normal.

While ultimately promising, the non-collinear reflection geometry for SXSFG requires careful consideration of future samples. Because the sample was unable to be rastered in this

configuration, having to stay below the laser damage threshold combined with the slower data acquisition method (*i.e.*, sweeping angle with MCP) presented serious experimental challenges.

Conclusions

Despite our difficulty in observing SXSFG, the collected data in transmission geometry did show large effects on nonlinear X-ray absorption.[231] The soft X-ray absorption showed time-dependent changes as a function of the delay time ($\Delta t = -1.15$ to $+1.00$ ps) between the incident optical and soft X-ray pulses. The FERMI group later published a more detailed experiment wherein time-resolved XAS were measured at the carbon *K*-edge for non-thermally melted carbon.[196] While we were ultimately unable to observe SXSFG signal in transmission and reflection geometries, we hope that these results will aid in designing and improving future second-order nonlinear spectroscopy experiments at free electron soft X-ray sources.

References

(1) Tobias, D. J.; Stern, A. C.; Baer, M. D.; Levin, Y.; Mundy, C. J. Simulation and Theory of Ions at Atmospherically Relevant Aqueous Liquid-Air Interfaces. *Annu. Rev. Phys. Chem.* **2013**, *64* (1), 339–359. https://doi.org/10.1146/annurev-physchem-040412-110049.

(2) Zhong, J.; Kumar, M.; Anglada, J. M.; Martins-Costa, M. T. C.; Ruiz-Lopez, M. F.; Zeng, X. C.; Francisco, J. S. Atmospheric Spectroscopy and Photochemistry at Environmental Water Interfaces. *Annu. Rev. Phys. Chem.* **2019**, *70* (1), 45–69. https://doi.org/10.1146/annurev-physchem-042018-052311.

(3) Yoshimoto, S.; Itaya, K. Adsorption and Assembly of Ions and Organic Molecules at Electrochemical Interfaces: Nanoscale Aspects. *Annu. Rev. Anal. Chem.* **2013**, *6* (1), 213–235. https://doi.org/10.1146/annurev-anchem-062012-092559.

(4) Pinca, J. R.; Duborg, W. G.; Jorn, R. Ion Association and Electrolyte Structure at Surface Films in Lithium-Ion Batteries. *J. Phys. Chem. C* **2021**, acs.jpcc.1c00393. https://doi.org/10.1021/acs.jpcc.1c00393.

(5) Wu, C. H.; Pascal, T. A.; Baskin, A.; Wang, H.; Fang, H.-T.; Liu, Y.-S.; Lu, Y.-H.; Guo, J.; Prendergast, D.; Salmeron, M. B. Molecular-Scale Structure of Electrode–Electrolyte Interfaces: The Case of Platinum in Aqueous Sulfuric Acid. *J. Am. Chem. Soc.* **2018**, *140* (47), 16237–16244. https://doi.org/10.1021/jacs.8b09743.

(6) Zhang, Y.; Cremer, P. S. Interactions between Macromolecules and Ions: The Hofmeister Series. *Curr. Opin. Chem. Biol.* **2006**, *10* (6), 658–663. https://doi.org/10.1016/j.cbpa.2006.09.020.

(7) Petersen, P. B.; Saykally, R. J.; Mucha, M.; Jungwirth, P. Enhanced Concentration of Polarizable Anions at the Liquid Water Surface: SHG Spectroscopy and MD Simulations of Sodium Thiocyanide. *J. Phys. Chem. B* **2005**, *109* (21), 10915–10921. https://doi.org/10.1021/jp050864c.

(8) Otten, D. E.; Shaffer, P. R.; Geissler, P. L.; Saykally, R. J. Elucidating the Mechanism of Selective Ion Adsorption to the Liquid Water Surface. *Proc. Natl. Acad. Sci.* **2012**, *109* (3), 701–705. https://doi.org/10.1073/pnas.1116169109.

(9) Mucha, M.; Frigato, T.; Levering, L. M.; Allen, H. C.; Tobias, D. J.; Dang, L. X.; Jungwirth, P. Unified Picture of the Surfaces of Aqueous Acid, Base, and Salt Solutions. *J. Phys. Chem. B* **2005**, *109* (Md), 7617.

(10) Jungwirth, P.; Tobias, D. J.; Heyro, J. V. Ions at the Air/Water Interface. *J. Phys. Chem. B* **2002**, 6361–6373. https://doi.org/10.1021/jp020242g.

(11) Onorato, R. M.; Otten, D. E.; Saykally, R. J. Adsorption of Thiocyanate Ions to the Dodecanol/Water Interface Characterized by UV Second Harmonic Generation. *Proc. Natl. Acad. Sci.* **2009**, *106* (36), 15176–15180. https://doi.org/10.1073/pnas.0904800106.

(12) McCaffrey, D. L.; Nguyen, S. C.; Cox, S. J.; Weller, H.; Alivisatos, A. P.; Geissler, P. L.; Saykally, R. J. Mechanism of Ion Adsorption to Aqueous Interfaces: Graphene/Water vs. Air/Water. *Proc. Natl. Acad. Sci.* **2017**, *114* (51), 13369–13373. https://doi.org/10.1073/pnas.1702760114.

(13) Cox, S. J.; Geissler, P. L. Interfacial Ion Solvation: Obtaining the Thermodynamic Limit from Molecular Simulations. *J. Chem. Phys.* **2018**, *148* (22). https://doi.org/10.1063/1.5020563.

(14) Wang, Y.; Sinha, S.; Desai, P. R.; Jing, H.; Das, S. Ion at Air-Water Interface Enhances Capillary Wave Fluctuations: Energetics of Ion Adsorption. *J. Am. Chem. Soc.* **2018**, *140*

(40), 12853–12861. https://doi.org/10.1021/jacs.8b06205.
(15) Hantal, G.; Kolafa, J.; Sega, M.; Jedlovszky, P. Single-Particle Dynamics at the Intrinsic Surface of Aqueous Alkali Halide Solutions. *J. Phys. Chem. B* **2021**, acs.jpcb.0c09989. https://doi.org/10.1021/acs.jpcb.0c09989.
(16) Misra, R. P.; Blankschtein, D. Uncovering a Universal Molecular Mechanism of Salt Ion Adsorption at Solid/Water Interfaces. *Langmuir* **2021**. https://doi.org/10.1021/acs.langmuir.0c02829.
(17) Paul, S. K.; Herbert, J. M. Probing Interfacial Effects on Ionization Energies : The Surprising Banality of Anion – Water Hydrogen Bonding at the Air / Water Interface. *ChemRxiv* **2021**. https://doi.org/https://doi.org/10.26434/chemrxiv.14273651.v1.
(18) Liu, J.; Zhang, J. Z. H.; He, X. Probing the Ion-Specific Effects at the Water/Air Interface and Water-Mediated Ion Pairing in Sodium Halide Solution with Ab Initio Molecular Dynamics. *J. Phys. Chem. B* **2018**, *122* (44), 10202–10209. https://doi.org/10.1021/acs.jpcb.8b09513.
(19) Smith, J. D.; Rick, S. W. Ion Clustering in Aqueous Salt Solutions near the Liquid/Vapor Interface. *Condens. Matter Phys.* **2016**, *19* (2), 23002. https://doi.org/10.5488/CMP.19.23002.
(20) Raymond, E. A.; Richmond, G. L. Probing the Molecular Structure and Bonding of the Surface of Aqueous Salt Solutions. *J. Phys. Chem. B* **2004**, *108* (16), 5051–5059. https://doi.org/10.1021/jp037725k.
(21) Liu, D.; Ma, G.; Levering, L. M.; Allen, H. C. Vibrational Spectroscopy of Aqueous Sodium Halide Solutions and Air-Liquid Interfaces: Observation of Increased Interfacial Depth. *J. Phys. Chem. B* **2004**, *108* (4), 2252–2260.
(22) Zhang, X. Mass Spectrometry at the Air-Water Interface. *Int. J. Mass Spectrom.* **2021**, 116527. https://doi.org/10.1016/j.ijms.2021.116527.
(23) Brown, M. A.; Winter, B.; Faubel, M.; Hemminger, J. C. Spatial Distribution of Nitrate and Nitrite Anions at the Liquid/Vapor Interface of Aqueous Solutions. *J. Am. Chem. Soc.* **2009**, *131* (24), 8354–8355. https://doi.org/10.1021/ja901791v.
(24) Shen, Y. R. *Fundamentals of Sum-Frequency Spectroscopy*; Cambridge University Press: Cambridge, U.K., 2016.
(25) Boyd, R. W. *Nonlinear Optics*; Academic Press, 2008.
(26) Sokhan, V. P.; Tildesley, D. J. The Free Surface of Water: Molecular Orientation, Surface Potential and Nonlinear Susceptibility. *Mol. Phys.* **1997**, *92* (4), 625–640. https://doi.org/10.1080/002689797169916.
(27) Rizzuto, A. M.; Irgen-Gioro, S.; Eftekhari-Bafrooei, A.; Saykally, R. J. Broadband Deep UV Spectra of Interfacial Aqueous Iodide. *J. Phys. Chem. Lett.* **2016**, *7* (19), 3882–3885. https://doi.org/10.1021/acs.jpclett.6b01931.
(28) Petersen, P. B.; Saykally, R. J. Probing the Interfacial Structure of Aqueous Electrolytes with Femtosecond Second Harmonic Generation Spectroscopy. *J. Phys. Chem. B* **2006**, *110*, 14060–14073.
(29) Yamaguchi, S.; Tahara, T. Precise Electronic $\chi^{(2)}$ Spectra of Molecules Adsorbed at an Interface Measured by Multiplex Sum Frequency Generation. *J. Phys. Chem. B* **2004**, *108* (50), 19079–19082. https://doi.org/10.1021/jp045306x.
(30) Brodeur, A.; Chin, S. L. Ultrafast White-Light Continuum Generation and Self-Focusing in Transparent Condensed Media. *J. Opt. Soc. Am. B* **1999**, *16* (4), 637. https://doi.org/10.1364/JOSAB.16.000637.

(31) Moad, A. J.; Simpson, G. J. A Unified Treatment of Selection Rules and Symmetry Relations for Sum-Frequency and Second Harmonic Spectroscopies. *J. Phys. Chem. B* **2004**, *108* (11), 3548–3562. https://doi.org/10.1021/jp035362i.
(32) Mizuno, H.; Rizzuto, A. M.; Saykally, R. J. Charge-Transfer-to-Solvent Spectrum of Thiocyanate at the Air/Water Interface Measured by Broadband Deep Ultraviolet Electronic Sum Frequency Generation Spectroscopy. *J. Phys. Chem. Lett.* **2018**, *9* (16), 4753–4757. https://doi.org/10.1021/acs.jpclett.8b01966.
(33) Blandamer, M. J.; Fox, M. F. Theory and Applications of Charge-Transfer-To-Solvent Spectra. *Chem. Rev.* **1970**, *70* (1), 59–93. https://doi.org/10.1021/cr60263a002.
(34) Rabinowitch, E. Electron Transfer Spectra and Their Photochemical Effects. *Rev. Mod. Phys.* **1942**, *14* (2–3), 112–131. https://doi.org/10.1103/RevModPhys.14.112.
(35) Smith, M.; Symons, M. C. R. Solvation Spectra. Part 1.—The Effect of Environmental Changes upon the Ultra-Violet Absorption of Solvated Iodide Ions. *Trans. Faraday Soc.* **1958**, *54*, 338–345. https://doi.org/10.1039/TF9585400338.
(36) Meyerstein, D.; Treinin, A. The Relation Between Lyotropic and Spectroscopic Properties of Anions in Solution. *J. Phys. Chem.* **1960**, *1* (3), 446–450. https://doi.org/10.1021/j100809a017.
(37) Stein, G.; Treinin, A. Electron-Transfer Spectra of Anions in Solution. Part 2. Temperature Dependence of Electron-Transfer Spectra of Anions in Aqueous Solution. *Trans. Faraday Soc.* **1959**, *7* (55), 1091–1099.
(38) Burak, I.; Treinin, A. Solvent Scale for Charge-Transfer-to-Solvent Spectra of Anions. *Trans. Faraday Soc.* **1963**, *59*, 1490. https://doi.org/10.1039/tf9635901490.
(39) Symons, M. C. R.; Jackson, S. E. Solvation Spectra Part 60. - Specific Solvation of Iodide Ions. *J. Chem. Soc. Faraday Trans. 1 Phys. Chem. Condens. Phases* **1978**, No. 75, 1919–1928. https://doi.org/10.1039/F19797501919.
(40) Blandamer, M. J.; Burdett, T. R. Effect of Pressure on the Ultra-Violet Absorption Spectra of Iodide in Non-Aqueous Solvents. *J. Chem. Soc. Faraday Trans. 2* **1972**, *68*, 577. https://doi.org/10.1039/f29726800577.
(41) Marin, T. W.; Janik, I.; Bartels, D. M. Ultraviolet Charge-Transfer-to-Solvent Spectroscopy of Halide and Hydroxide Ions in Subcritical and Supercritical Water. *Phys. Chem. Chem. Phys.* **2019**, *21* (44), 24419–24428. https://doi.org/10.1039/c9cp03805a.
(42) Hofmeister, F. Zur Lehre von Der Wirkung Der Salze. *Arch. für Exp. Pathol. und Pharmakologie* **1888**, *24* (4–5), 247–260. https://doi.org/10.1007/BF01918191.
(43) Fox, M. F.; Smith, C. B.; Hayon, E. Far-Ultraviolet Solution Spectroscopy of Thiocyanate. *J. Chem. Soc., Faraday Trans.* **1981**, *77*, 1497–1502.
(44) Gusarsky, E.; Treinin, A. The Relation between Electrochemical and Spectroscopic Properties of the Halide and Pseudohalide Ions in Solution. *J. Phys. Chem.* **1965**, *69* (9), 3176–3177. https://doi.org/10.1021/j100893a506.
(45) Fox, M. F.; Hayon, E. Far Ultraviolet Solution Spectroscopy of the Iodide Ion. *J. Chem. Soc. Faraday Trans. 1* **1977**, *73*, 1003–1016. https://doi.org/10.1039/f19777301003.
(46) Dogliotti, L.; Hayon, E. Flash Photolysis Study of Sulfite, Thiocyanate, and Thiosulfate Ions in Solution. *J. Phys. Chem.* **1968**, *72* (5), 1800–1807. https://doi.org/10.1021/j100851a073.
(47) Botti, A.; Pagnotta, S. E.; Bruni, F.; Ricci, M. A. Solvation of KSCN in Water. *J. Phys. Chem. B* **2009**, *113* (29), 10014–10021. https://doi.org/10.1021/jp903462h.
(48) Baer, M. D.; Mundy, C. J. An Ab Initio Approach to Understanding the Specific Ion

Effect. *Faraday Discuss.* **2013**, *160*, 89–101. https://doi.org/10.1039/C2FD20113E.
(49) Viswanath, P.; Motschmann, H. Oriented Thiocyanate Anions at the Air-Electrolyte Interface and Its Implications on Interfacial Water - A Vibrational Sum Frequency Spectroscopy Study. *J. Phys. Chem. C Lett.* **2007**, *111* (12), 4484–4486. https://doi.org/10.1021/jp0702649.
(50) Viswanath, P.; Motschmann, H. Effect of Interfacial Presence of Oriented Thiocyanate on Water Structure. *J. Phys. Chem. C* **2008**, *112* (6), 2099–2103. https://doi.org/10.1021/jp077229m.
(51) Tesei, G.; Aspelin, V.; Lund, M. Specific Cation Effects on SCN^- in Bulk Solution and at the Air–Water Interface. *J. Phys. Chem. B* **2018**, *122* (19), 5094–5105. https://doi.org/10.1021/acs.jpcb.8b02303.
(52) Schlaich, A.; Knapp, E. W.; Netz, R. R. Water Dielectric Effects in Planar Confinement. *Phys. Rev. Lett.* **2016**, *117* (4), 1–5. https://doi.org/10.1103/PhysRevLett.117.048001.
(53) Venkateshwaran, V.; Vembanur, S.; Garde, S. Water-Mediated Ion-Ion Interactions Are Enhanced at the Water Vapor-Liquid Interface. *Proc. Natl. Acad. Sci.* **2014**, *111* (24), 8729–8734. https://doi.org/10.1073/pnas.1403294111.
(54) Bian, H.; Wen, X.; Li, J.; Chen, H.; Han, S.; Sun, X.; Song, J.; Zhuang, W.; Zheng, J. Ion Clustering in Aqueous Solutions Probed with Vibrational Energy Transfer. *Proc. Natl. Acad. Sci.* **2011**, *108* (12), 4737–4742. https://doi.org/10.1073/pnas.1019565108.
(55) Gong, S.; Wang, P.; Wei, Z.; Yang, B.; Xu, X.; Xu, H.; Zheng, W. Microsolvation of Sodium Thiocyanate in Water: Gas Phase Anion Photoelectron Spectroscopy and Theoretical Calculations. *J. Phys. Chem. A* **2020**, *124* (38), 7816–7826. https://doi.org/10.1021/acs.jpca.0c07071.
(56) Ishiyama, T.; Morita, A. Intermolecular Correlation Effect in Sum Frequency Generation Spectroscopy of Electrolyte Aqueous Solution. *Chem. Phys. Lett.* **2006**, *431* (1–3), 78–82. https://doi.org/10.1016/j.cplett.2006.09.024.
(57) Ishiyama, T.; Morita, A. Molecular Dynamics Study of Gas-Liquid Aqueous Sodium Halide Interfaces. I. Flexible and Polarizable Molecular Modeling and Interfacial Properties. *J. Phys. Chem. C* **2007**, *111* (2), 721–737. https://doi.org/10.1021/jp065191s.
(58) Hao, H.; Xie, Q.; Ai, J.; Wang, Y.; Bian, H. Specific Counter-Cation Effect on the Molecular Orientation of Thiocyanate Anions at the Aqueous Solution Interface. *Phys. Chem. Chem. Phys.* **2020**, *22* (18), 10106–10115. https://doi.org/10.1039/D0CP00974A.
(59) Luria, M.; Treinin, A. Photochemistry of Thiocyanate Ion in Solution. *J. Phys. Chem.* **1968**, *72* (1), 305–308. https://doi.org/10.1021/j100847a059.
(60) Koralek, J. D.; Kim, J. B.; Brůža, P.; Curry, C. B.; Chen, Z.; Bechtel, H. A.; Cordones, A. A.; Sperling, P.; Toleikis, S.; Kern, J. F.; et al. Generation and Characterization of Ultrathin Free-Flowing Liquid Sheets. *Nat. Commun.* **2018**, *9* (1), 1–8. https://doi.org/10.1038/s41467-018-03696-w.
(61) Mondal, S. K.; Yamaguchi, S.; Tahara, T. Molecules at the Air/Water Interface Experience a More Inhomogeneous Solvation Environment than in Bulk Solvents: A Quantitative Band Shape Analysis of Interfacial Electronic Spectra Obtained by HD-ESFG. *J. Phys. Chem. C* **2011**, *115* (7), 3083–3089. https://doi.org/10.1021/jp110456t.
(62) Bhattacharyya, D.; Mizuno, H.; Rizzuto, A. M.; Zhang, Y.; Saykally, R. J.; Bradforth, S. E. New Insights into the Charge-Transfer-to-Solvent Spectrum of Aqueous Iodide: Surface versus Bulk. *J. Phys. Chem. Lett.* **2020**, *11* (5), 1656–1661. https://doi.org/10.1021/acs.jpclett.9b03857.

(63) Chen, X.; Bradforth, S. E. The Ultrafast Dynamics of Photodetachment. *Annu. Rev. Phys. Chem.* **2008**, *59* (1), 203–231. https://doi.org/10.1146/annurev.physchem.58.032806.104702.
(64) Matheson, M. S.; Mulac, W. A.; Rabani, J. Formation of the Hydrated Electron in the Flash Photolysis of Aqueous Solutions. *J. Phys. Chem.* **1963**, *67* (12), 2613–2617. https://doi.org/10.1021/j100806a027.
(65) Jortner, J.; Raz, B.; Stein, G. The Far u.-v. Absorption Spectrum of the Iodide Ion in Aqueous Solution. *Trans. Faraday Soc.* **1960**, *56*, 1273. https://doi.org/10.1039/tf9605601273.
(66) Fox, M. F.; Hayon, E. New CTTS Absoprtion Bands of Iodide in the Far-Ultraviolet Region. *Chem. Phys. Lett.* **1972**, *14* (4), 442–444. https://doi.org/10.1016/0009-2614(72)80234-3.
(67) Barker, B. E.; Fox, M. F.; Walton, A. Resolution of the Far Ultraviolet Absorption Bands of Solvated Iodide. *J. Chem. Soc. Faraday Trans. 1* **1976**, *72*, 344. https://doi.org/10.1039/f19767200344.
(68) Kloepfer, J. A.; Vilchiz, V. H.; Lenchenkov, V. A.; Germaine, A. C.; Bradforth, S. E. The Ejection Distribution of Solvated Electrons Generated by the One-Photon Photodetachment of Aqueous I^- and Two-Photon Ionization of the Solvent. *J. Chem. Phys.* **2000**, *113* (15), 6288–6307. https://doi.org/10.1063/1.1309011.
(69) Vilchiz, V. H.; Kloepfer, J. A.; Germaine, A. C.; Lenchenkov, V. A.; Bradforth, S. E. Map for the Relaxation Dynamics of Hot Photoelectrons Injected into Liquid Water via Anion Threshold Photodetachment and above Threshold Solvent Ionization. *J. Phys. Chem. A* **2001**, *105* (10), 1711–1723. https://doi.org/10.1021/jp003974m.
(70) Sheu, W. S.; Rossky, P. J. The Electronic Dynamics of Photoexcited Aqueous Iodide. *Chem. Phys. Lett.* **1993**, *202* (3–4), 186–190. https://doi.org/10.1016/0009-2614(93)85263-N.
(71) Sheu, W. S.; Rossky, P. J. Electronic and Solvent Relaxation Dynamics of a Photoexcited Aqueous Halide. *J. Phys. Chem.* **1996**, *100* (4), 1295–1302. https://doi.org/10.1021/jp9513531.
(72) Moskun, A. C.; Bradforth, S. E.; Thøgersen, J.; Keiding, S. Absence of a Signature of Aqueous $I(^2P_{1/2})$ after 200-Nm Photodetachment of I^-(aq). *J. Phys. Chem. A* **2006**, *110* (38), 10947–10955. https://doi.org/10.1021/jp053992+.
(73) Bradforth, S. E.; Jungwirth, P. Excited States of Iodide Anions in Water: A Comparison of the Electronic Structure in Clusters and in Bulk Solution. *J. Phys. Chem. A* **2002**, *106* (7), 1286–1298. https://doi.org/10.1021/jp013068p.
(74) Barthel, E. R.; Martini, I. B.; Schwartz, B. J. How Does the Solvent Control Electron Transfer? Experimental and Theoretical Studies of the Simplest Charge Transfer Reaction. *J. Phys. Chem. B* **2001**, *105* (49), 12230–12241. https://doi.org/10.1021/jp011150e.
(75) Nowakowski, P. J.; Woods, D. A.; Verlet, J. R. R. Charge Transfer to Solvent Dynamics at the Ambient Water/Air Interface. *J. Phys. Chem. Lett.* **2016**, *7* (20), 4079–4085. https://doi.org/10.1021/acs.jpclett.6b01985.
(76) Sagar, D. M.; Bain, C. D.; Verlet, J. R. R. Hydrated Electrons at the Water / Air Interface. *J. Am. Chem. Soc.* **2010**, No. 2, 6917–6919.
(77) Sheu, W. S.; Rossky, P. J. Charge-Transfer-to-Solvent Spectra of an Aqueous Halide Revisited via Computer Simulation. *J. Am. Chem. Soc.* **1993**, *115* (17), 7729–7735. https://doi.org/10.1021/ja00070a017.

(78) Elles, C. G.; Rivera, C. A.; Zhang, Y.; Pieniazek, P. A.; Bradforth, S. E. Electronic Structure of Liquid Water from Polarization-Dependent Two-Photon Absorption Spectroscopy. *J. Chem. Phys.* **2009**, *130* (8), 084501. https://doi.org/10.1063/1.3078336.
(79) Tauber, M. J.; Mathies, R. A.; Chen, X.; Bradforth, S. E. Flowing Liquid Sample Jet for Resonance Raman and Ultrafast Optical Spectroscopy. *Rev. Sci. Instrum.* **2003**, *74* (11), 4958–4960. https://doi.org/10.1063/1.1614874.
(80) Bhattacharyya, D.; Zhang, Y.; Elles, C. G.; Bradforth, S. E. Electronic Structure of Liquid Methanol and Ethanol from Polarization-Dependent Two-Photon Absorption Spectroscopy. *J. Phys. Chem. A* **2019**, *123* (27), 5789–5804. https://doi.org/10.1021/acs.jpca.9b04040.
(81) Petersen, P. B.; Saykally, R. J. On the Nature of Ions At the Liquid Water Surface. *Annu. Rev. Phys. Chem.* **2006**, *57* (23), 333–364. https://doi.org/10.1146/annurev.physchem.57.032905.104609.
(82) Petersen, P. B.; Johnson, J. C.; Knutsen, K. P.; Saykally, R. J. Direct Experimental Validation of the Jones-Ray Effect. *Chem. Phys. Lett.* **2004**, *397* (1–3), 46–50. https://doi.org/10.1016/j.cplett.2004.08.048.
(83) Lin, C.-K.; Hayashi, M.; Lin, S. H. Theoretical Formulation and Simulation of Electronic Sum-Frequency Generation Spectroscopy. *J. Phys. Chem. C* **2013**, *117* (45), 23797–23805. https://doi.org/10.1021/jp407881a.
(84) Kothe, A.; Wilke, M.; Moguilevski, A.; Engel, N.; Winter, B.; Kiyan, I. Y.; Aziz, E. F. Charge Transfer to Solvent Dynamics in Iodide Aqueous Solution Studied at Ionization Threshold. *Phys. Chem. Chem. Phys.* **2015**, *17* (3), 1918–1924. https://doi.org/10.1039/C4CP02482F.
(85) Messina, F.; Bräm, O.; Cannizzo, A.; Chergui, M. Real-Time Observation of the Charge Transfer to Solvent Dynamics. *Nat. Commun.* **2013**, *4*, 2119. https://doi.org/10.1038/ncomms3119.
(86) Franck, J.; Scheibe, G. Über Absorptionsspektren Negativer Halogenionen in Lösung. *Zeitschrift für Phys. Chemie* **1928**, *139A* (1), 22–31. https://doi.org/10.1515/zpch-1928-13904.
(87) Jortner, J.; Ottolenghi, M.; Stein, G. On the Photochemistry of Aqueous Solutions of Chloride, Bromide, and Iodide Ions. *J. Phys. Chem.* **1964**, *68* (2), 247–255. https://doi.org/10.1021/j100784a005.
(88) Platzman, R.; Franck, J. The Role of the Hydration Configuration in Electronic Processes Involving Ions in Aqueous Solution. *Zeitschrift für Phys.* **1954**, *138* (3–4), 411–431. https://doi.org/10.1007/BF01340687.
(89) Jortner, J.; Treinin, A. Intensities of the Absorption Bands of Halide Ions in Solution. *Trans. Faraday Soc.* **1962**, *58*, 1503–1510. https://doi.org/10.1039/tf9625801503.
(90) Herzberg, G. *Atomic Spectra and Atomic Structure*, 2nd ed.; Dover Publications: New York, 1944.
(91) Moore, C. E. *Atomic Energy Levels as Derived from the Analysis of Optical Spectra*; National Bureau of Standards: Washington, D.C., 1952; Vol. 2.
(92) Ku, J. K.; Setser, D. W. Collisional Deactivation of Xe(5p56p) States in Xe and Ar. *J. Chem. Phys.* **1986**, *84* (8), 4304–4316. https://doi.org/10.1063/1.450825.
(93) Faisal, F. H. M.; Wallenstein, R.; Zacharias, H. Three-Photon Excitation of Xenon and Carbon Monoxide. *Phys. Rev. Lett.* **1977**, *39* (18), 1138–1141. https://doi.org/10.1103/PhysRevLett.39.1138.

(94) Blandamer, M. J.; Gough, T. E.; Symons, M. C. R. Solvation Spectra. Part 5.—Effect of Pressure on the Ultra-Violet Absorption Spectrum of Solvated Iodide. *Trans. Faraday Soc.* **1963**, *59*, 1748–1753. https://doi.org/10.1039/TF9635901748.
(95) Griffiths, T. R.; Wijayanayake, R. H. Effects of Cations upon Absorption Spectra. Part 5.—Charge-Transfer-to-Solvent Spectrum of Iodide and Ion-Pair Formation. *Trans. Faraday Soc.* **1970**, *66* (June 1967), 1563–1573. https://doi.org/10.1039/TF9706601563.
(96) McGuire, E. J. Two- and Three-Photon Ionization in the Noble Gases. *Phys. Rev. A* **1981**, *24* (2), 835–848. https://doi.org/10.1103/PhysRevA.24.835.
(97) Stern, A. C.; Baer, M. D.; Mundy, C. J.; Tobias, D. J. Thermodynamics of Iodide Adsorption at the Instantaneous Air-Water Interface. *J. Chem. Phys.* **2013**, *138* (11). https://doi.org/10.1063/1.4794688.
(98) Caleman, C.; Hub, J. S.; van Maaren, P. J.; van der Spoel, D. Atomistic Simulation of Ion Solvation in Water Explains Surface Preference of Halides. *Proc. Natl. Acad. Sci.* **2011**, *108* (17), 6838–6842. https://doi.org/10.1073/pnas.1017903108.
(99) Karmakar, A.; Chandra, A. Water in Hydration Shell of an Iodide Ion: Structure and Dynamics of Solute-Water Hydrogen Bonds and Vibrational Spectral Diffusion from First-Principles Simulations. *J. Phys. Chem. B* **2015**, *119* (27), 8561–8572. https://doi.org/10.1021/jp510714e.
(100) Mizuno, H.; Oosterbaan, K. J.; Menzl, G.; Smith, J.; Rizzuto, A. M.; Geissler, P. L.; Head-Gordon, M.; Saykally, R. J. Revisiting the $\pi \rightarrow \pi^*$ Transition of the Nitrite Ion at the Air/Water Interface: A Combined Experimental and Theoretical Study. *Chem. Phys. Lett.* **2020**, *751*, 137516. https://doi.org/10.1016/j.cplett.2020.137516.
(101) Otten, D. E.; Onorato, R. M.; Michaels, R.; Goodknight, J.; Saykally, R. J. Strong Surface Adsorption of Aqueous Sodium Nitrite as an Ion Pair. *Chem. Phys. Lett.* **2012**, *519–520*, 45–48. https://doi.org/10.1016/j.cplett.2011.10.056.
(102) Treinin, A.; Hayon, E. Absorption Spectra and Reaction Kinetics of NO_2, N_2O_3, and N_2O_4 in Aqueous Solution. *J. Am. Chem. Soc.* **1970**, *92* (20), 5821–5828. https://doi.org/10.1021/ja00723a001.
(103) Zafiriou, O. C.; True, M. B. Nitrite Photolysis in Seawater by Sunlight. *Mar. Chem.* **1979**, *8*, 9–32.
(104) Vione, D.; Maurino, V.; Minero, C.; Pelizzetti, E.; Harrison, M. A. J.; Olariu, R.-I.; Arsene, C. Photochemical Reactions in the Tropospheric Aqueous Phase and on Particulate Matter. *Chem. Soc. Rev.* **2006**, *35* (5), 441–453. https://doi.org/10.1039/b510796m.
(105) Trawick, W. G.; Eberhardt, W. H. Electronic Transitions in the Nitrite Ion. *J. Chem. Phys.* **1954**, *22* (8), 1462–1462. https://doi.org/10.1063/1.1740425.
(106) Sidman, J. W. Electronic and Vibrational States of the Nitrite Ion. I. Electronic States. *J. Am. Chem. Soc.* **1957**, *79* (11), 2669–2675. https://doi.org/10.1021/ja01568a002.
(107) Strickler, S. J.; Kasha, M. Solvent Effects on the Electronic Absorption Spectrum of Nitrite Ion. *J. Am. Chem. Soc.* **1963**, *85* (19), 2899–2901. https://doi.org/10.1021/ja00902a007.
(108) Friedman, H. L. On the Ultraviolet Absorption Spectra of Uninegative Ions. *J. Chem. Phys.* **1953**, *21* (2), 319–322. https://doi.org/10.1063/1.1698879.
(109) Stein, G.; Treinin, A. Electron-Transfer Spectra of Anions in Solution. Part 1.- Absorption Spectra and Ionic Radii. *Trans. Faraday Soc.* **1959**, *55* (7), 1086–1090.
(110) Rizzuto, A. M. Investigation of the Surface Properties of Aqueous Solutions, University of

California, Berkeley, 2016.
(111) Hua, W.; Verreault, D.; Adams, E. M.; Huang, Z.; Allen, H. C. Impact of Salt Purity on Interfacial Water Organization Revealed by Conventional and Heterodyne-Detected Vibrational Sum Frequency Generation Spectroscopy. *J. Phys. Chem. C* **2013**, *117* (38), 19577–19585. https://doi.org/10.1021/jp408146t.
(112) Atkovska, K.; Hub, J. S. Energetics and Mechanism of Anion Permeation across Formate-Nitrite Transporters. *Sci. Rep.* **2017**, *7* (1), 1–14. https://doi.org/10.1038/s41598-017-11437-0.
(113) Kam, H. C.; Ranathunga, D. T. S.; Payne, E. R.; Smaldone, R. A.; Nielsen, S. O.; Dodani, S. C. Spectroscopic Characterization and in Silico Modelling of Polyvinylpyrrolidone as an Anion-Responsive Fluorescent Polymer in Aqueous Media. *Supramol. Chem.* **2019**, *31* (8), 514–522. https://doi.org/10.1080/10610278.2019.1630740.
(114) Berendsen, H. J. C.; Grigera, J. R.; Straatsma, T. P. The Missing Term in Effective Pair Potentials. *J. Phys. Chem.* **1987**, *91* (24), 6269–6271. https://doi.org/10.1021/j100308a038.
(115) Leontyev, I.; Stuchebrukhov, A. Accounting for Electronic Polarization in Non-Polarizable Force Fields. *Phys. Chem. Chem. Phys.* **2011**, *13* (7), 2613–2626. https://doi.org/10.1039/c0cp01971b.
(116) Vega, C.; Abascal, J. L. F. Simulating Water with Rigid Non-Polarizable Models: A General Perspective. *Phys. Chem. Chem. Phys.* **2011**, *13* (44), 19663–19688. https://doi.org/10.1039/c1cp22168j.
(117) Pegado, L.; Marsalek, O.; Jungwirth, P.; Wernersson, E. Solvation and Ion-Pairing Properties of the Aqueous Sulfate Anion: Explicit versus Effective Electronic Polarization. *Phys. Chem. Chem. Phys.* **2012**, *14* (29), 10248–10257. https://doi.org/10.1039/c2cp40711f.
(118) Jorgensen, W. L.; Chandrasekhar, J.; Madura, J. D.; Impey, R. W.; Klein, M. L. Comparison of Simple Potential Functions for Simulating Liquid Water. *J. Chem. Phys.* **1983**, *79* (2), 926–935. https://doi.org/10.1063/1.445869.
(119) Chandler, D. *Introduction to Modern Statistical Mechanics*, 1st Ed.; Oxford University Press: New York, 1987.
(120) Hess, B.; Bekker, H.; Berendsen, H. J. C.; Fraaije, J. G. E. M. LINCS: A Linear Constraint Solver for Molecular Simulations. *J. Comput. Chem.* **1997**, *18* (12), 1463–1472. https://doi.org/10.1002/(SICI)1096-987X(199709)18:12<1463::AID-JCC4>3.0.CO;2-H.
(121) Bussi, G.; Donadio, D.; Parrinello, M. Canonical Sampling through Velocity Rescaling. *J. Chem. Phys.* **2007**, *126* (1). https://doi.org/10.1063/1.2408420.
(122) Essmann, U.; Perera, L.; Berkowitz, M. L.; Darden, T.; Lee, H.; Pedersen, L. G. A Smooth Particle Mesh Ewald Method. *J. Chem. Phys.* **1995**, *103* (19), 8577–8593. https://doi.org/10.1063/1.470117.
(123) Abraham, M. J.; Murtola, T.; Schulz, R.; Páll, S.; Smith, J. C.; Hess, B.; Lindah, E. Gromacs: High Performance Molecular Simulations through Multi-Level Parallelism from Laptops to Supercomputers. *SoftwareX* **2015**, *1–2*, 19–25. https://doi.org/10.1016/j.softx.2015.06.001.
(124) Tribello, G. A.; Bonomi, M.; Branduardi, D.; Camilloni, C.; Bussi, G. PLUMED 2: New Feathers for an Old Bird. *Comput. Phys. Commun.* **2014**, *185* (2), 604–613. https://doi.org/10.1016/j.cpc.2013.09.018.

(125) Rhee, Y. M.; Casanova, D.; Head-Gordon, M. Performance of Quasi-Degenerate Scaled Opposite Spin Perturbation Corrections to Single Excitation Configuration Interaction for Excited State Structures and Excitation Energies with Application to the Stokes Shift of 9-Methyl-9,10-Dihydro-9-Silaphenanthrene. *J. Phys. Chem. A* **2009**, *113* (39), 10564–10576. https://doi.org/10.1021/jp903659u.
(126) Head-Gordon, M.; Oumi, M.; Maurice, D. Quasidegenerate Second-Order Perturbation Corrections to Single-Excitation Configuration Interaction. *Mol. Phys.* **1999**, *96* (4), 593–602. https://doi.org/10.1080/00268979909482996.
(127) Schreiber, M.; Silva-Junior, M. R.; Sauer, S. P. A.; Thiel, W. Benchmarks for Electronically Excited States: CASPT2, CC2, CCSD, and CC3. *J. Chem. Phys.* **2008**, *128* (13), 134110. https://doi.org/10.1063/1.2889385.
(128) Kánnár, D.; Szalay, P. G. Benchmarking Coupled Cluster Methods on Valence Singlet Excited States. *J. Chem. Theory Comput.* **2014**, *10* (9), 3757–3765. https://doi.org/10.1021/ct500495n.
(129) Gross, E. K. U.; Dobson, J. F.; Petersilka, M. Density Functional Theory of Time-Dependent Phenomena. In *Density Functional Theory II*; Springer-Verlag: Berlin/Heidelberg, 2005; pp 81–172. https://doi.org/10.1007/BFb0016643.
(130) Furche, F. On the Density Matrix Based Approach to Time-Dependent Density Functional Response Theory. *J. Chem. Phys.* **2001**, *114* (14), 5982–5992. https://doi.org/10.1063/1.1353585.
(131) Görling, A.; Heinze, H. H.; Ruzankin, S. P.; Staufer, M.; Rösch, N. Density- and Density-Matrix-Based Coupled Kohn–Sham Methods for Dynamic Polarizabilities and Excitation Energies of Molecules. *J. Chem. Phys.* **1999**, *110* (6), 2785–2799. https://doi.org/10.1063/1.477922.
(132) Bauernschmitt, R.; Ahlrichs, R. *Treatment of Electronic Excitations within the Adiabatic Approximation of Time Dependent Density Functional Theory*; 1996; Vol. 256.
(133) Jamorski, C.; Casida, M. E.; Salahub, D. R. Dynamic Polarizabilities and Excitation Spectra from a Molecular Implementation of Time-dependent Density-functional Response Theory: N_2 as a Case Study. *J. Chem. Phys.* **1996**, *104* (13), 5134–5147. https://doi.org/10.1063/1.471140.
(134) Rappoport, D.; Furche, F. Property-Optimized Gaussian Basis Sets for Molecular Response Calculations. *J. Chem. Phys.* **2010**, *133* (13), 134105. https://doi.org/10.1063/1.3484283.
(135) Weigend, F.; Ahlrichs, R. Balanced Basis Sets of Split Valence, Triple Zeta Valence and Quadruple Zeta Valence Quality for H to Rn: Design and Assessment of Accuracy. *Phys. Chem. Chem. Phys.* **2005**, *7* (18), 3297. https://doi.org/10.1039/b508541a.
(136) Smith, J. W.; Lam, R. K.; Shih, O.; Rizzuto, A. M.; Prendergast, D.; Saykally, R. J. Properties of Aqueous Nitrate and Nitrite from X-Ray Absorption Spectroscopy. *J. Chem. Phys.* **2015**, *143* (8), 084503. https://doi.org/10.1063/1.4928867.
(137) Fumagalli, L.; Esfandiar, A.; Fabregas, R.; Hu, S.; Ares, P.; Janardanan, A.; Yang, Q.; Radha, B.; Taniguchi, T.; Watanabe, K.; et al. Anomalously Low Dielectric Constant of Confined Water. *Science.* **2018**, *360* (6395), 1339–1342. https://doi.org/10.1126/science.aat4191.
(138) Varghese, S.; Kannam, S. K.; Hansen, J. S.; Sathian, S. P.; P. Sathian, S.; Sathian, S. P. Effect of Hydrogen Bonds on the Dielectric Properties of Interfacial Water. *Langmuir* **2019**, *35* (24), 8159–8166. https://doi.org/10.1021/acs.langmuir.9b00543.

(139) Sun, S.; Schaefer, J.; Backus, E. H. G.; Bonn, M. How Surface-Specific Is 2nd-Order Non-Linear Spectroscopy? *J. Chem. Phys.* **2019**, *151* (23). https://doi.org/10.1063/1.5129108.
(140) Barry, B. A. The Role of Redox-Active Amino Acids in the Photosynthetic Water-Oxidizing Complex. *Photochem. Photobiol.* **1993**, *57* (1), 179–188. https://doi.org/10.1111/j.1751-1097.1993.tb02275.x.
(141) Rayne, S.; Forest, K.; Friesen, K. J. Mechanistic Aspects Regarding the Direct Aqueous Environmental Photochemistry of Phenol and Its Simple Halogenated Derivatives. A Review. *Environ. Int.* **2009**, *35* (2), 425–437. https://doi.org/10.1016/j.envint.2008.09.004.
(142) Smith, J. D.; Sio, V.; Yu, L.; Zhang, Q.; Anastasio, C. Secondary Organic Aerosol Production from Aqueous Reactions of Atmospheric Phenols with an Organic Triplet Excited State. *Environ. Sci. Technol.* **2014**, *48* (2), 1049–1057. https://doi.org/10.1021/es4045715.
(143) Ryder, O. S.; Campbell, N. R.; Shaloski, M.; Al-Mashat, H.; Nathanson, G. M.; Bertram, T. H. Role of Organics in Regulating $ClNO_2$ Production at the Air-Sea Interface. *J. Phys. Chem. A* **2015**, *119* (31), 8519–8526. https://doi.org/10.1021/jp5129673.
(144) Wei, Z.; Li, Y.; Cooks, R. G.; Yan, X. Accelerated Reaction Kinetics in Microdroplets: Overview and Recent Developments. *Annu. Rev. Phys. Chem.* **2020**, *71* (1), 31–51. https://doi.org/10.1146/annurev-physchem-121319-110654.
(145) Kusaka, R.; Nihonyanagi, S.; Tahara, T. The Photochemical Reaction of Phenol Becomes Ultrafast at the Air–Water Interface. *Nat. Chem.* **2021**, 1–7. https://doi.org/10.1038/s41557-020-00619-5.
(146) Sobolewski, A. L.; Domcke, W.; Dedonder-Lardeux, C.; Jouvet, C. Excited-State Hydrogen Detachment and Hydrogen Transfer Driven by Repulsive $^1\pi\sigma^*$ States: A New Paradigm for Nonradiative Decay in Aromatic Biomolecules. *Phys. Chem. Chem. Phys.* **2002**, *4* (7), 1093–1100. https://doi.org/10.1039/b110941n.
(147) Ashfold, M. N. R.; King, G. A.; Murdock, D.; Nix, M. G. D.; Oliver, T. A. A.; Sage, A. G. $\pi\sigma^*$ Excited States in Molecular Photochemistry. *Phys. Chem. Chem. Phys.* **2010**, *12* (6), 1218–1238. https://doi.org/10.1039/B921706A.
(148) Iqbal, A.; Cheung, M. S. Y.; Nix, M. G. D.; Stavros, V. G. Exploring the Time-Scales of H-Atom Detachment from Photoexcited Phenol-h_6 and Phenol-d_5 : Statistical vs Nonstatistical Decay. *J. Phys. Chem. A* **2009**, *113* (29), 8157–8163. https://doi.org/10.1021/jp9031223.
(149) Riley, J. W.; Wang, B.; Woodhouse, J. L.; Assmann, M.; Worth, G. A.; Fielding, H. H. Unravelling the Role of an Aqueous Environment on the Electronic Structure and Ionization of Phenol Using Photoelectron Spectroscopy. *J. Phys. Chem. Lett.* **2018**, *9* (4), 678–682. https://doi.org/10.1021/acs.jpclett.7b03310.
(150) Harris, S. J.; Murdock, D.; Zhang, Y.; Oliver, T. A. A.; Grubb, M. P.; Orr-Ewing, A. J.; Greetham, G. M.; Clark, I. P.; Towrie, M.; Bradforth, S. E.; et al. Comparing Molecular Photofragmentation Dynamics in the Gas and Liquid Phases. *Phys. Chem. Chem. Phys.* **2013**, *15* (18), 6567–6582. https://doi.org/10.1039/c3cp50756d.
(151) Zhang, Y.; Oliver, T. A. A.; Ashfold, M. N. R.; Bradforth, S. E. Contrasting the Excited State Reaction Pathways of Phenol and Para-Methylthiophenol in the Gas and Liquid Phases. *Faraday Discuss.* **2012**, *157*, 141–163. https://doi.org/10.1039/c2fd20043k.
(152) Oliver, T. A. A.; Zhang, Y.; Roy, A.; Ashfold, M. N. R.; Bradforth, S. E. Exploring Autoionization and Photoinduced Proton-Coupled Electron Transfer Pathways of Phenol

in Aqueous Solution. *J. Phys. Chem. Lett.* **2015**, *6* (20), 4159–4164. https://doi.org/10.1021/acs.jpclett.5b01861.
(153) Sandler, I.; Nogueira, J. J.; González, L. Solvent Reorganization Triggers Photo-Induced Solvated Electron Generation in Phenol. *Phys. Chem. Chem. Phys.* **2019**, *21* (26), 14261–14269. https://doi.org/10.1039/C8CP06656F.
(154) Harkins, W. D.; Grafton, E. H. Monomolecular Films on Water: The Oriented Adsorption of Derivatives of Benzene. *J. Am. Chem. Soc.* **1925**, *47* (5), 1329–1335. https://doi.org/10.1021/ja01682a017.
(155) Filek, M.; Paluch, M.; Waligóra, B. Electrical Properties of the Monolayers of *p*-Phenol Derivatives. *J. Colloid Interface Sci.* **1982**, *89* (1), 166–169. https://doi.org/10.1016/0021-9797(82)90130-8.
(156) Hicks, J. M.; Kemnitz, K.; Eisenthal, K. B.; Heinz, T. F. Studies of Liquid Surfaces by Second Harmonic Generation. *J. Phys. Chem.* **1986**, *90* (4), 560–562. https://doi.org/10.1021/j100276a015.
(157) Tamburello-Luca, A. A.; Hébert, P.; Brevet, P. F.; Girault, H. H. Resonant-Surface Second-Harmonic Generation Studies of Phenol Derivatives at Air/Water and Hexane/Water Interfaces. *J. Chem. Soc., Faraday Trans.* **1996**, *92* (17), 3079–3085. https://doi.org/10.1039/FT9969203079.
(158) Plimpton, S. Fast Parallel Algorithms for Short-Range Molecular Dynamics. *J. Comput. Phys.* **1995**, *117* (1), 1–19. https://doi.org/10.1006/jcph.1995.1039.
(159) Spasic, A.; Serafini, J.; Mathews, D. H. The Amber Ff99 Force Field Predicts Relative Free Energy Changes for RNA Helix Formation. *J. Chem. Theory Comput.* **2012**, *8* (7), 2497–2505. https://doi.org/10.1021/ct300240k.
(160) Andersen, H. C. Rattle: A "Velocity" Version of the Shake Algorithm for Molecular Dynamics Calculations. *J. Comput. Phys.* **1983**, *52* (1), 24–34. https://doi.org/10.1016/0021-9991(83)90014-1.
(161) Kamberaj, H.; Low, R. J.; Neal, M. P. Time Reversible and Symplectic Integrators for Molecular Dynamics Simulations of Rigid Molecules. *J. Chem. Phys.* **2005**, *122* (22), 224114. https://doi.org/10.1063/1.1906216.
(162) Scheiner, S.; Kar, T.; Pattanayak, J. Comparison of Various Types of Hydrogen Bonds Involving Aromatic Amino Acids. *J. Am. Chem. Soc.* **2002**, *124* (44), 13257–13264. https://doi.org/10.1021/ja027200q.
(163) Kusaka, R.; Ishiyama, T.; Nihonyanagi, S.; Morita, A.; Tahara, T. Structure at the Air/Water Interface in the Presence of Phenol: A Study Using Heterodyne-Detected Vibrational Sum Frequency Generation and Molecular Dynamics Simulation. *Phys. Chem. Chem. Phys.* **2018**, *20* (5), 3002–3009. https://doi.org/10.1039/C7CP05150F.
(164) Schirmer, J. Beyond the Random-Phase Approximation: A New Approximation Scheme for the Polarization Propagator. *Phys. Rev. A* **1982**, *26* (5), 2395–2416. https://doi.org/10.1103/PhysRevA.26.2395.
(165) Schirmer, J.; Trofimov, A. B. Intermediate State Representation Approach to Physical Properties of Electronically Excited Molecules. *J. Chem. Phys.* **2004**, *120* (24), 11449–11464. https://doi.org/10.1063/1.1752875.
(166) Shao, Y.; Gan, Z.; Epifanovsky, E.; Gilbert, A. T. B.; Wormit, M.; Kussmann, J.; Lange, A. W.; Behn, A.; Deng, J.; Feng, X.; et al. Advances in Molecular Quantum Chemistry Contained in the Q-Chem 4 Program Package. *Mol. Phys.* **2015**, *113* (2), 184–215. https://doi.org/10.1080/00268976.2014.952696.

(167) Limão-Vieira, P.; Duflot, D.; Ferreira Da Silva, F.; Lange, E.; Jones, N. C.; Hoffmann, S. V.; Ğmiałek, M. A.; Jones, D. B.; Brunger, M. J. Valence and Lowest Rydberg Electronic States of Phenol Investigated by Synchrotron Radiation and Theoretical Methods. *J. Chem. Phys.* **2016**, *145* (3). https://doi.org/10.1063/1.4955334.
(168) Gerrard, D. L. L.; Maddams, W. F. F. Solvent Effects in u.v. Absorption Spectra. I. Phenol in Cyclohexane Ethanol Mixtures. *Spectrochim. Acta Part A Mol. Spectrosc.* **1978**, *34* (12), 1205–1211. https://doi.org/10.1016/0584-8539(78)80081-6.
(169) Fornander, L. H.; Feng, B.; Beke-Somfai, T.; Nordén, B. UV Transition Moments of Tyrosine. *J. Phys. Chem. B* **2014**, *118* (31), 9247–9257. https://doi.org/10.1021/jp5065352.
(170) Shen, Y. R.; Ostroverkhov, V. Sum-Frequency Vibrational Spectroscopy on Water Interfaces: Polar Orientation of Water Molecules at Interfaces. *Chem. Rev.* **2006**, *106* (4), 1140–1154. https://doi.org/10.1021/cr040377d.
(171) Nihonyanagi, S.; Mondal, J. A.; Yamaguchi, S.; Tahara, T. Structure and Dynamics of Interfacial Water Studied by Heterodyne-Detected Vibrational Sum-Frequency Generation. *Annu. Rev. Phys. Chem.* **2013**, *64*, 579–603. https://doi.org/10.1146/annurev-physchem-040412-110138.
(172) Sun, S.; Bisson, P. J.; Bonn, M.; Shultz, M. J.; Backus, E. H. G. Phase-Sensitive Sum-Frequency Generation Measurements Using a Femtosecond Nonlinear Interferometer. *J. Phys. Chem. C* **2019**, *123* (12), 7266–7270. https://doi.org/10.1021/acs.jpcc.9b00861.
(173) Xu, X.; Shen, Y. R.; Tian, C. Phase-Sensitive Sum Frequency Vibrational Spectroscopic Study of Air/Water Interfaces: H_2O, D_2O, and Diluted Isotopic Mixtures. *J. Chem. Phys.* **2019**, *150* (14), 144701. https://doi.org/10.1063/1.5081135.
(174) Vanselous, H.; Petersen, P. B. Extending the Capabilities of Heterodyne-Detected Sum-Frequency Generation Spectroscopy: Probing Any Interface in Any Polarization Combination. *J. Phys. Chem. C* **2016**, *120* (15), 8175–8184. https://doi.org/10.1021/acs.jpcc.6b01252.
(175) Yamaguchi, S.; Tahara, T. Heterodyne-Detected Electronic Sum Frequency Generation: "Up" versus "down" Alignment of Interfacial Molecules. *J. Chem. Phys.* **2008**, *129* (10). https://doi.org/10.1063/1.2981179.
(176) Yamaguchi, S.; Watanabe, H.; Mondal, S. K.; Kundu, A.; Tahara, T. Up versus down Alignment and Hydration Structures of Solutes at the Airwater Interface Revealed by Heterodyne-Detected Electronic Sum Frequency Generation with Classical Molecular Dynamics Simulation. *J. Chem. Phys.* **2011**, *135* (19). https://doi.org/10.1063/1.3662136.
(177) Moon, A. P.; Pandey, R.; Bender, J. A.; Cotton, D. E.; Renard, B. A.; Roberts, S. T. Using Heterodyne-Detected Electronic Sum Frequency Generation to Probe the Electronic Structure of Buried Interfaces. *J. Phys. Chem. C* **2017**, *121* (34), 18653–18664. https://doi.org/10.1021/acs.jpcc.7b05514.
(178) Watanabe, H.; Yamaguchi, S.; Sen, S.; Morita, A.; Tahara, T. "Half-Hydration" At the Air/Water Interface Revealed By Heterodyne-Detected Electronic Sum Frequency Generation Spectroscopy, Polarization Second Harmonic Generation, and Molecular Dynamics Simulation. *J. Chem. Phys.* **2010**, *132* (14). https://doi.org/10.1063/1.3372620.
(179) Smolentsev, N.; Chen, Y.; Jena, K. C.; Brown, M. A.; Roke, S. Sum Frequency and Second Harmonic Generation from the Surface of a Liquid Microjet. *J. Chem. Phys.* **2014**, *141* (18), 18C524. https://doi.org/10.1063/1.4896996.
(180) Morita, A.; Koizumi, A.; Hirano, T. Recent Progress in Simulating Microscopic Ion

Transport Mechanisms at Liquid–Liquid Interfaces. *J. Chem. Phys.* **2021**, *154* (8), 080901. https://doi.org/10.1063/5.0039172.
(181) Petersen, P. B.; Saykally, R. J. Confirmation of Enhanced Anion Concentration at the Liquid Water Surface. *Chem. Phys. Lett.* **2004**, *397* (1–3), 51–55. https://doi.org/10.1016/j.cplett.2004.08.049.
(182) Lam, R. K.; Smith, J. W.; Rizzuto, A. M.; Karslloğlu, O.; Bluhm, H.; Saykally, R. J. Reversed Interfacial Fractionation of Carbonate and Bicarbonate Evidenced by X-Ray Photoemission Spectroscopy. *J. Chem. Phys.* **2017**, *146* (9). https://doi.org/10.1063/1.4977046.
(183) Opalka, D.; Sprik, M. Solute-Solvent Charge-Transfer Excitations and Optical Absorption of Hydrated Hydroxide from Time-Dependent Density-Functional Theory. *J. Chem. Theory Comput.* **2014**, *10* (6), 2465–2470. https://doi.org/10.1021/ct5002889.
(184) Lin, L.; Husek, J.; Biswas, S.; Baumler, S. M.; Adel, T.; Ng, K. C.; Baker, L. R.; Allen, H. C. Iron(III) Speciation Observed at Aqueous and Glycerol Surfaces: Vibrational Sum Frequency and X-Ray. *J. Am. Chem. Soc.* **2019**, *141* (34), 13525–13535. https://doi.org/10.1021/jacs.9b05231.
(185) Donaldson, D. J.; Guest, J. A.; Goh, M. C. Evidence for Adsorbed SO_2 at the Aqueous-Air Interface. *J. Phys. Chem.* **1995**, *99* (23), 9313–9315. https://doi.org/10.1021/j100023a002.
(186) Hua, W.; Verreault, D.; Allen, H. C. Relative Order of Sulfuric Acid, Bisulfate, Hydronium, and Cations at the Air–Water Interface. *J. Am. Chem. Soc.* **2015**, *137* (43), 13920–13926. https://doi.org/10.1021/jacs.5b08636.
(187) Hull, C. J.; Raj, S. L.; Saykally, R. J. The Liquid State of Carbon. *Chem. Phys. Lett.* **2020**, *749* (March), 137341. https://doi.org/10.1016/j.cplett.2020.137341.
(188) Kroto, H. W.; Heath, J. R.; O'Brien, S. C.; Curl, R. F.; Smalley, R. E. C60: Buckminsterfullerene. *Nature* **1985**, *318* (6042), 162–163. https://doi.org/10.1038/318162a0.
(189) de Heer, W. A. Liquid Carbon, Carbon-Glass Beads, and the Crystallization of Carbon Nanotubes. *Science.* **2005**, *307* (5711), 907–910. https://doi.org/10.1126/science.1107035.
(190) Narayan, J.; Bhaumik, A. Novel Phase of Carbon, Ferromagnetism, and Conversion into Diamond. *J. Appl. Phys.* **2015**, *118* (21), 215303. https://doi.org/10.1063/1.4936595.
(191) Reitze, D. H.; Ahn, H.; Downer, M. C. Optical Properties of Liquid Carbon Measured by Femtosecond Spectroscopy. *Phys. Rev. B* **1992**, *45* (6), 2677–2693. https://doi.org/10.1103/PhysRevB.45.2677.
(192) Raj, S.; Devlin, S.; Mincigrucci, R.; Schwartz, C.; Principi, E.; Bencivenga, F.; Foglia, L.; Gessini, A.; Simoncig, A.; Kurdi, G.; et al. Free Electron Laser Measurement of Liquid Carbon Reflectivity in the Extreme Ultraviolet. *Photonics* **2020**, *7* (2), 35. https://doi.org/10.3390/photonics7020035.
(193) Savvatimskiy, A. I. Experimental Electrical Resistivity of Liquid Carbon in the Temperature Range from 4800 to ~20,000 K. *Carbon N. Y.* **2009**, *47* (10), 2322–2328. https://doi.org/10.1016/j.carbon.2009.04.009.
(194) Johnson, S. L.; Heimann, P. A.; MacPhee, A. G.; Lindenberg, A. M.; Monteiro, O. R.; Chang, Z.; Lee, R. W.; Falcone, R. W. Bonding in Liquid Carbon Studied by Time-Resolved X-Ray Absorption Spectroscopy. *Phys. Rev. Lett.* **2005**, *94* (5), 1–4. https://doi.org/10.1103/PhysRevLett.94.057407.
(195) Kraus, D.; Vorberger, J.; Gericke, D. O.; Bagnoud, V.; Blažević, A.; Cayzac, W.; Frank, A.; Gregori, G.; Ortner, A.; Otten, A.; et al. Probing the Complex Ion Structure in Liquid

Carbon at 100 GPa. *Phys. Rev. Lett.* **2013**, *111* (25), 1–5. https://doi.org/10.1103/PhysRevLett.111.255501.
(196) Principi, E.; Krylow, S.; Garcia, M. E.; Simoncig, A.; Foglia, L.; Mincigrucci, R.; Kurdi, G.; Gessini, A.; Bencivenga, F.; Giglia, A.; et al. Atomic and Electronic Structure of Solid-Density Liquid Carbon. *Phys. Rev. Lett.* **2020**, *125* (15), 155703. https://doi.org/10.1103/PhysRevLett.125.155703.
(197) Wu, C. J.; Glosli, J. N.; Galli, G.; Ree, F. H. Liquid-Liquid Phase Transition in Elemental Carbon: A First-Principles Investigation. *Phys. Rev. Lett.* **2002**, *89* (13), 1–4. https://doi.org/10.1103/PhysRevLett.89.135701.
(198) Whitley, H. D.; Sanchez, D. M.; Hamel, S.; Correa, A. A.; Benedict, L. X. Molecular Dynamics Simulations of Warm Dense Carbon. *Contrib. to Plasma Phys.* **2015**, *55* (5), 390–398. https://doi.org/10.1002/ctpp.201400101.
(199) Matsuda, I.; Kubota, Y. Recent Progresses in Spectroscopies Using Soft X-Ray Free-Electron Laser. *Chem. Lett.* **2021**, cl.200881. https://doi.org/10.1246/cl.200881.
(200) Park, S. H.; Yoon, J.; Kim, C.; Hwang, C.; Kim, D. H.; Lee, S. H.; Kwon, S. Scientific Instruments for Soft X-Ray Photon-in/Photon-out Spectroscopy on the PAL-XFEL. *J. Synchrotron Radiat.* **2019**, *26*, 1031–1036. https://doi.org/10.1107/S1600577519004272.
(201) Lomba, E.; López-Martín, J. L.; Anta, J. A.; Ho/ye, J. S.; Kahl, G. A Theoretical Approach to the Tight-Binding Band Structure of Liquid Carbon and Silicon beyond Linear Approximations. *J. Chem. Phys.* **1997**, *106* (24), 10238–10247. https://doi.org/10.1063/1.474050.
(202) Chuang, C. H.; Ray, S. C.; Ma, D.; Sharma, S.; Ganguly, A.; Papakonstantinou, P.; Chiou, J. W.; Tsai, H. M.; Mazumder, D.; Sharma, S.; et al. Chemical Modification of Graphene Oxide by Nitrogenation: An X-Ray Absorption and Emission Spectroscopy Study. *Sci. Rep.* **2017**, *7* (January), 1–10. https://doi.org/10.1038/srep42235.
(203) Nagler, B.; Zastrau, U.; Fäustlin, R. R.; Vinko, S. M.; Whitcher, T.; Nelson, A. J.; Sobierajski, R.; Krzywinski, J.; Chalupsky, J.; Abreu, E.; et al. Turning Solid Aluminium Transparent by Intense Soft X-Ray Photoionization. *Nat. Phys.* **2009**, *5* (9), 693–696. https://doi.org/10.1038/nphys1341.
(204) Beye, M.; Sorgenfrei, F.; Schlotter, W. F.; Wurth, W.; Fohlisch, A. The Liquid-Liquid Phase Transition in Silicon Revealed by Snapshots of Valence Electrons. *Proc. Natl. Acad. Sci.* **2010**, *107* (39), 16772–16776. https://doi.org/10.1073/pnas.1006499107.
(205) Hull, C.; Raj, S.; Lam, R.; Katayama, T.; Pascal, T.; Drisdell, W. S.; Saykally, R.; Schwartz, C. P. Early Time Dynamics of Laser-Ablated Silicon Using Ultrafast Grazing Incidence X-Ray Scattering. *Chem. Phys. Lett.* **2019**, *736* (September), 136811. https://doi.org/10.1016/j.cplett.2019.136811.
(206) Tirsell, K. G.; Karpenko, V. P. A General Purpose Sub-KeV X-Ray Facility at the Stanford Synchrotron Radiation Laboratory. *Nucl. Inst. Methods Phys. Res. A* **1990**, *291* (1–2), 511–517. https://doi.org/10.1016/0168-9002(90)90113-K.
(207) Qiao, R.; Li, Q.; Zhuo, Z.; Sallis, S.; Fuchs, O.; Blum, M.; Weinhardt, L.; Heske, C.; Pepper, J.; Jones, M.; et al. High-Efficiency in Situ Resonant Inelastic x-Ray Scattering (IRIXS) Endstation at the Advanced Light Source. *Rev. Sci. Instrum.* **2017**, *88* (3). https://doi.org/10.1063/1.4977592.
(208) Lindsey, R. K.; Fried, L. E.; Goldman, N. ChIMES: A Force Matched Potential with Explicit Three-Body Interactions for Molten Carbon. *J. Chem. Theory Comput.* **2017**, *13* (12), 6222–6229. https://doi.org/10.1021/acs.jctc.7b00867.

(209) Kohn, W.; Sham, L. J. Self-Consistent Equations Including Exchange and Correlation Effects. *Phys. Rev.* **1965**, *140* (4A), A1133–A1138. https://doi.org/10.1103/PhysRev.140.A1133.
(210) Hohenberg, P.; Kohn, W. Inhomogeneous Electron Gas. *Phys. Rev.* **1964**, *136* (3B), B864–B871. https://doi.org/10.1103/PhysRev.136.B864.
(211) Hutter, J.; Iannuzzi, M.; Schiffmann, F.; VandeVondele, J. CP2K: Atomistic Simulations of Condensed Matter Systems. *Wiley Interdiscip. Rev. Comput. Mol. Sci.* **2014**, *4* (1), 15–25. https://doi.org/10.1002/wcms.1159.
(212) Nowak, S. H.; Armenta, R.; Schwartz, C. P.; Gallo, A.; Abraham, B.; Garcia-Esparza, A. T.; Biasin, E.; Prado, A.; Maciel, A.; Zhang, D.; et al. A Versatile Johansson-Type Tender X-Ray Emission Spectrometer. *Rev. Sci. Instrum.* **2020**, *91* (3). https://doi.org/10.1063/1.5121853.
(213) Díaz, J.; Paolicelli, G.; Ferrer, S.; Comin, F. Separation of the sp^3 and sp^2 components in the C1*s* photoemission spectra of amorphous carbon films. *Phys. Rev. B* **1996**, *54* (11), 8064–8069. https://doi.org/10.1103/PhysRevB.54.8064.
(214) Haerle, R.; Riedo, E.; Pasquarello, A.; Baldereschi, A. sp^2/sp^3 Hybridization Ratio in Amorphous Carbon from C 1*s* Core-Level Shifts: X-Ray Photoelectron Spectroscopy and First-Principles Calculation. *Phys. Rev. B* **2001**, *65* (4), 045101. https://doi.org/10.1103/PhysRevB.65.045101.
(215) Díaz, J.; Anders, S.; Zhou, X.; Moler, E. J.; Kellar, S. A.; Hussain, Z. Analysis of the π^* and σ^* bands of the x-ray absorption spectrum of amorphous carbon. *Phys. Rev. B* **2001**, *64* (12), 125204. https://doi.org/10.1103/PhysRevB.64.125204.
(216) Mérel, P.; Tabbal, M.; Chaker, M.; Moisa, S.; Margot, J. Direct Evaluation of the sp^3 Content in Diamond-like-Carbon Films by XPS. *Appl. Surf. Sci.* **1998**, *136* (1–2), 105–110. https://doi.org/10.1016/S0169-4332(98)00319-5.
(217) Kumar, N.; Kozakov, A. T.; Dash, S.; Tyagi, A. K.; Lin, I. N. Microstructure, Chemical Bonds, and Friction Properties of Nanocrystalline Diamond Films Deposited in Two Different Plasma Media. *Phys. Solid State* **2013**, *55* (10), 2076–2087. https://doi.org/10.1134/S1063783413100181.
(218) Walter, M.; Mangolini, F.; McClimon, J. B.; Carpick, R. W.; Moseler, M. Fermi Level Pinning by Defects Can Explain the Large Reported Carbon 1*s* Binding Energy Variations in Diamond. **2019**, No. arXiv:1902.02958, 1–6.
(219) Garrelie, F.; Bourquard, F.; Loir, A. S.; Donnet, C. Control of Femtosecond Pulsed Laser Deposition by Temporal Pulse Shaping. *Opt. InfoBase Conf. Pap.* **2014**.
(220) Yasumaru, N.; Miyazaki, K.; Kiuchi, J. Glassy Carbon Layer Formed in Diamond-like Carbon Films with Femtosecond Laser Pulses. *Appl. Phys. A* **2004**, *79* (3), 425–427. https://doi.org/10.1007/s00339-004-2746-3.
(221) Kanasaki, J.; Inami, E.; Tanimura, K.; Ohnishi, H.; Nasu, K. Formation of sp^3-Bonded Carbon Nanostructures by Femtosecond Laser Excitation of Graphite. *Phys. Rev. Lett.* **2009**, *102* (8), 087402. https://doi.org/10.1103/PhysRevLett.102.087402.
(222) Scott, H. A.; Hansen, S. B. Advances in NLTE Modeling for Integrated Simulations. *High Energy Density Phys.* **2010**, *6* (1), 39–47. https://doi.org/10.1016/j.hedp.2009.07.003.
(223) Lam, R. K.; Raj, S. L.; Pascal, T. A.; Pemmaraju, C. D.; Foglia, L.; Simoncig, A.; Fabris, N.; Miotti, P.; Hull, C. J.; Rizzuto, A. M.; et al. Soft X-Ray Second Harmonic Generation as an Interfacial Probe. *Phys. Rev. Lett.* **2018**, *120* (2), 23901. https://doi.org/10.1103/PhysRevLett.120.023901.

(224) Yamamoto, S.; Omi, T.; Akai, H.; Kubota, Y.; Takahashi, Y.; Suzuki, Y.; Hirata, Y.; Yamamoto, K.; Yukawa, R.; Horiba, K.; et al. Element Selectivity in Second-Harmonic Generation of $GaFeO_3$ by a Soft-X-Ray Free-Electron Laser. *Phys. Rev. Lett.* **2018**, *120* (22), 223902. https://doi.org/10.1103/PhysRevLett.120.223902.
(225) Schwartz, C. P.; Raj, S. L.; Jamnuch, S.; Hull, C. J.; Miotti, P.; Lam, R. K.; Nordlund, D.; Uzundal, C. B.; Pemmaraju, C. Das; Mincigrucci, R.; et al. Angstrom-Resolved Interfacial Structure in Organic-Inorganic Junctions. *arXiv* **2020**, 1–19.
(226) Allaria, E.; Appio, R.; Badano, L.; Barletta, W. A.; Bassanese, S.; Biedron, S. G.; Borga, A.; Busetto, E.; Castronovo, D.; Cinquegrana, P.; et al. Highly Coherent and Stable Pulses from the FERMI Seeded Free-Electron Laser in the Extreme Ultraviolet. *Nat. Photonics* **2012**, *6* (10), 699–704. https://doi.org/10.1038/nphoton.2012.233.
(227) Glover, T. E.; Fritz, D. M.; Cammarata, M.; Allison, T. K.; Coh, S.; Feldkamp, J. M.; Lemke, H.; Zhu, D.; Feng, Y.; Coffee, R. N.; et al. X-Ray and Optical Wave Mixing. *Nature* **2012**, *488* (7413), 603–608. https://doi.org/10.1038/nature11340.
(228) Simoncig, A.; Mincigrucci, R.; Principi, E.; Bencivenga, F.; Calvi, A.; Foglia, L.; Kurdi, G.; Raimondi, L.; Manfredda, M.; Mahne, N.; et al. The EIS Beamline at the Seeded Free-Electron Laser FERMI. *X-ray Lasers Coherent X-ray Sources Dev. Appl.* **2017**, *10243* (May 2017), 102430L. https://doi.org/10.1117/12.2268152.
(229) Masciovecchio, C.; Battistoni, A.; Giangrisostomi, E.; Bencivenga, F.; Principi, E.; Mincigrucci, R.; Cucini, R.; Gessini, A.; D'Amico, F.; Borghes, R.; et al. EIS: The Scattering Beamline at FERMI. *J. Synchrotron Radiat.* **2015**, *22* (February), 553–564. https://doi.org/10.1107/S1600577515003380.
(230) Zangrando, M.; Cocco, D.; Fava, C.; Gerusina, S.; Gobessi, R.; Mahne, N.; Mazzucco, E.; Raimondi, L.; Rumiz, L.; Svetina, C. Recent Results of PADReS, the Photon Analysis Delivery and REduction System, from the FERMI FEL Commissioning and User Operations. *J. Synchrotron Radiat.* **2015**, *22*, 565–570. https://doi.org/10.1107/S1600577515004580.
(231) Hoffmann, L. Nonlinear X-Ray Absorption of Graphite, Freie University Berlin, 2019.